



Université Catholique de Louvain

Faculté des Sciences

École de Physique

Center for Cosmology, Particle Physics and Phenomenology

*A New Approach to Matrix
Element Re-Weighting*

Olivier Mattelaer

Jury de thèse :

J. M. Gerard (UCL-CP3) *Président*

F. Maltoni (UCL-CP3) *Promoteur*

V. Lemaître (UCL-CP3)

J. Govaerts (UCL-CP3)

J. D'hondt (VUB)

G. Degrassi (INFN-Roma Tre)

January 2011

Remerciements

A la base de toute thèse se cachent dans l'ombre le travail et la patience d'un promoteur. Le professeur Jan Govaerts a été tout un temps mon promoteur, il m'a permis de comprendre ce qu'était la recherche ainsi que la rigueur nécessaire à celle-ci. Il m'a laissé une liberté qui m'a permis de m'intéresser à d'autres projets et finalement de changer de sujet de thèse et de promoteur. Le professeur Fabio Maltoni a alors accepté d'encadrer mes recherches sur la pondération par éléments de matrice et m'a notamment mis en contact avec différents collaborateurs pour que cette recherche puisse réellement prendre son envol. Outre ses compétences scientifiques, je retiendrai sa chaleur lors de chacune de nos rencontres.

Je tiens aussi à remercier mon jury. Merci d'avoir lu attentivement ma thèse et d'avoir contribué à améliorer la qualité de celle-ci par leurs remarques et commentaires. Merci d'avoir accepté cette charge et de l'avoir accomplie avec un réel professionnalisme malgré de lourdes charges. Un merci tout particulier à Giuseppe pour l'accueil dispensé lors de l'année passée à Rome.

Le support technique et administratif offert par CP3/FYNU a toujours été d'un niveau excellent tant pour le service informatique que pour le secrétariat. Merci pour les maintenances des clusters, pour les commandes de billets d'avion, les relectures de lettres, de travaux, etc.

Une thèse est non seulement (et surtout) un travail de recherches, mais c'est aussi une tranche de vie marquée par des rencontres et des échanges enrichissants, non seulement à Louvain-La-Neuve et à Rome mais aussi lors de nombreuses conférences auxquelles j'ai assisté.

Différentes personnes ont permis à ces années de thèse d'être d'enrichissantes tant scientifiquement que personnellement. Je pense notamment à l'ambiance inimitable et inoubliable mise par les membres du CP3, et en particulier à nos discussions stratégiques sur les trolls. Merci aussi à l'ensemble de mes collaborateurs (Pierre, Johan, Michel, Arnaud, Claude, Priscilla, Céline, Will, Rik, Ayres, Vincent, Tim, Fabio, Jan, Matondo, Valentin) avec qui c'était toujours un plaisir de travailler mais aussi de discuter autour d'un verre et/ou d'un bon repas. En particulier je voudrais remercier Pierre Artoisenet, avec qui MADWEIGHT a été réellement conçu, cette collaboration fructueuse fut le point de départ de cette thèse. De plus, le travail au sein du team MADGRAPH a aussi été aussi l'occasion d'apprendre à travailler au sein d'un groupe d'une grande qualité scientifique et humaine.

Ma thèse m'a aussi permis de découvrir celle qui sera dans peu de temps ma femme. Je tiens à la remercier pour son soutien sans faille et sans borne. Son aide et sa patience durant ces derniers mois m'ont permis de garder ma concentration et d'arriver à terminer ma thèse dans les temps. Le soutien de ma famille m'a également été d'un précieux secours. Mes parents sont sans doute tout aussi fiers que moi de cette thèse. Merci de m'avoir donné la possibilité de faire ces études et de m'avoir soutenu dans mes choix. Merci aussi à mon frère et ma soeur pour leurs touchantes attentions. Je voudrais aussi souligner le sens de la famille élargie qui est le nôtre. Ainsi, ma Marraïne et son mari, Laurent, ont proposé, spontanément, de relire le texte de ce travail afin d'en améliorer le style et l'anglais.

Finalement je remercierai mes amis, le groupe du temps de midi, des randonnées, du voyage au Jura et à l'île d'Oleron. Tous ces moments m'ont permis de sortir des équations et des lignes de code pour revisiter les petits bonheurs de la vie. Un merci tout particulier aux Jumeaux et à Catherine qui m'ont tellement soutenu, écouté et avec qui j'ai partagé tant de bons moments. Un merci aussi à Bruno et Tatiana pour toutes les soirées passées ensemble des plus simples aux plus absurdes.

Merci à tous ceux qui ont pris la peine de venir à ma défense publique : leur présence m'a profondément touché.

“It is possible to store the mind with a million facts and still be entirely uneducated.”

Alec Bourne

Table des matières

Introduction	11
1 The current theoretical picture : the search for new physics	15
1.1 Standard Model	16
1.1.1 Electroweak interactions before symmetry breaking	16
1.1.2 The Brout-Englert-Higgs mechanism	18
1.1.3 Strong interactions	19
1.2 The quest for the Higgs	20
1.2.1 Theoretical constraints	20
1.2.2 LEP exclusion	21
1.2.3 Tevatron exclusion	23
1.2.4 LHC searches	24
1.2.5 Indirect constraints from precision measurements	26
1.3 Top-Quark Mass measurement	28
1.4 Physics Beyond the Standard Model	30
1.5 Minimal Super-symmetric Standard Model	31
1.6 Characterise new physics	32

2	Matrix element re-weighting	35
3	Computation of the weights : a general method	39
3.1	Monte-Carlo techniques	40
3.1.1	Adaptive Monte Carlo techniques	41
3.1.2	Multi-Channel method	43
3.2	Strategy of the integrator	44
3.3	Primary change of variables	46
3.4	Change of variables fixing the conservation of energy-momentum	48
3.5	Combining the blocks	53
3.6	Finding the appropriate change of variable	54
3.7	One-channel phase-space generator	55
3.8	Validation of the phase-space generator	56
4	Standard Applications of the Matrix Element Re-weighting	61
4.1	The Matrix Element Method	62
4.2	Top-quark mass measurement	66
4.3	Smuon production	68
4.4	Spin sensitivity : Charged Higgs	71
4.5	Differential Matrix Element Method	75
5	QCD Radiation In the Matrix Element Method	81
5.1	Initial State Radiation at partonic level	83
5.2	Initial State Radiation at the hadron level	87
	Conclusions	93

A	Changes of Variables	97
A.1	Phase-space measure associated with the final blocks	97
A.1.1	FB A	97
A.1.2	FB B	98
A.1.3	FB C	99
A.1.4	FB D	101
A.1.5	FB E	103
A.1.6	FB F	105
A.2	Phase-space measure associated with the secondary blocks	107
A.2.1	PB A	107
A.2.2	PB B	108
A.2.3	PB C/D	109
A.2.4	PB E	110
B	Monte-Carlo and statistics associated to marginal distribution	113
B.1	marginal distributions	113
B.2	Correlation matrix and chi-square	114

Introduction

“What is a scientist after all ? It is a curious man looking through a keyhole, the keyhole of nature, trying to know what’s going on.”

Jacques Yves Cousteau

It is an exciting time for high energy physics, as the most powerful accelerators ever built are now exploring phenomena at scales and distances never probed before. The TEVATRON Run II at the Fermi National Accelerator Laboratory, with more than 5 fb^{-1} of integrated luminosity, has provided a plethora of information on the TeV scales, from an extremely precise measure of the top-quark mass [1] to the 95% confidence level exclusion of a Standard Model Higgs with a mass between 154 and 170 GeV [2]. At the same time, the LHC at CERN after only few months of running, has provided to CMS and ATLAS already few tens of pb^{-1} starting the physics program, with the first important measurements (vector boson and top cross sections [3,4]) as well as competitive exclusions for new physics (dijet resonances [5,6], leptoquarks [7],...).

The fundamental interactions and constituents of matter are framed in the Standard Model (SM) of the electroweak and strong interactions. The SM is not only a mathematically consistent (and beautiful !) theory but also describes extremely well (almost) all observed high-energy phenomena. From the first predictions in the late seventies –such as the observations of neutral weak currents and of bottom quark (necessary for CP violation)– to the precision measurements of LEP, its successes have been impressive, even beyond our best expectations and in some cases hopes.

In this context, the purpose of the current collider experiments is first to observe and then measure the properties of the Higgs, the independent physical state of the scalar sector. This sector is important in the SM not only because it is linked to the fermion/boson mass spectrum, but also because measuring the Higgs mass will fix the last unconstrained parameter of the SM. Nevertheless, its discovery is less than guaranteed, not only because alternative scenarios for EWSB exist, but also given that the favoured region determined by precision measurements [8] is already excluded by the direct searches made at LEP [9].

This small tension in the SM as well as the presence of inelegant fine-tuning –which is necessary to have stability of the Fermi scale– could be the indication that the SM is not the correct theory and that we need to go Beyond the Standard Model (BSM). Many theories have been proposed in the last years to solve some critical points of the Standard Model. For example, theories like Large Extra Dimensions [10, 11], MSSM [12, 13] and walking technicolor [14, 15] provide a way to regularise the gauge boson scattering and/or to fix the hierarchy problem.

All such theories are, in general, characterised by a set of new physical states interacting weakly and/or strongly with the known SM particles. If their couplings are sizeable enough and if their masses are in the kinematical reach of the LHC, such particles are expected to be directly produced. They will then decay in the detectors (or in some cases also escape them), giving visible signatures (or missing transverse energy). Extracting new physics signatures from the huge amount of QCD events at hadron colliders is going to be a real challenge. Compared to the electron-positron collisions (like LEP), the data flow describing events resulting from the head-on collision of two high energy proton beams at LHC/TEVATRON is extremely complex. This is due to several effects : the non-trivial structure of the proton, the total amount of energy available in the rest frame of the collision and, last but not least, the high luminosity at which the machines have been designed to work.

Analysing the data of a detector in a proton-proton collider and identifying the imprints left by the Higgs or by any BSM particles are extremely challenging tasks and call for dedicated experimental and analysis methods. The first stage of any analysis consists in applying a set of kinematical cuts in order to curb as much as possible the SM backgrounds, without rejecting too much of the “signal” events. While this allows to reach discovery significance in many cases, it also requests a detailed knowledge of the Standard Model backgrounds, especially in underpopulated regions of the phase space. Sometimes, even this stage can be difficult. As a following step, the different measurement methods can be categorised into two main classes :

- methods that do not use any (or little) theoretical input, i.e., **model independent methods**. This class of methods is particularly suited for discoveries since the nature of the new physics can have a large variety of properties. Those techniques are

often based on the estimation of general features from distributions. The measurement of end-points in distributions and/or the position of the peaks, for example, can provide key information on the new particles –most of the time the mass. The end point technique [16] and M_{T2} [17, 18] are examples of such methods.

- methods that (even maximally) use theoretical knowledge on the searched signal are called **model dependent**. Those methods can use the full theoretical information provided by a given benchmark in order to enhance the information of interest and help to reach discovery (or exclusions) significance. Kinematical fits [19,20] can be considered as a clear example of a model-dependent method, since in this case the decay chain and the mass of some of the propagators are assumed.

The *Matrix Element Method* (MEM), the main application of the matrix element re-weighting studied in this thesis, fits in the second category. It maximally exploits the theoretical information (i.e., the matrix-element) to assign a probability to each event. In this thesis, we will study the interest of such re-weighting for the ongoing search in accelerator physics.

This work is divided into five different parts. The first Chapter is dedicated to a brief overview of the Standard Model and one of its most popular extensions, the MSSM. It also describes different measurement techniques used in literature. The second Chapter presents the details of the MEM and introduces the definition of the event-by-event matrix element re-weighting. The third Chapter presents an algorithm designed for an efficient numerical and automatic estimation of the weight associated to each event. This algorithm is then exploited in Chapter four in order to study the interest and the sensitivity of this method. It starts by presenting possible application of the matrix element re-weighting in the context of the LHC both using a template method and the MEM. Then this chapter presents an original way to estimate differential cross-sections in order to observe new physics, named *differential* Matrix Element Method (DMEM). The last chapter studies the modification to MEM in presence of QCD radiation such that the method keeps its predictive power.

The work presented in this thesis has been the object of various publications, first on MADWEIGHT and on the Matrix Element Method [21, 22, 23] and on the QCD correction [24, 25]. The last Chapter on the estimation of the cross-section contains results that have not been published yet.

Chapitre 1

The current theoretical picture : the search for new physics

*“What we observe is not nature itself,
but nature exposed to our method of
questioning.”*

Werner Heisenberg

The question on the nature of the world is longstanding. The theory of the *four elements* shows that the Greek philosophers were already interested in the fundamental components of matter. Since then, the search for the fundamental building blocks has made sensational progresses both on the experimental and theoretical sides. Those advances are now embedded in our current representation of the fundamental particles and interactions, the *Standard Model*.

This first Chapter aims at giving a very brief picture of the Standard Model and to motivate the search for the last missing piece, i.e. the Higgs boson. This Chapter will also introduce the motivations and possible directions for searching physics beyond the Standard Model, highlighting the experimental challenges to measure and characterise the properties of eventual new particles.

Since this presentation is not supposed to be exhaustive, the interested reader is invited to consult excellent references such as [26] or [27] for more details on the Standard Model, [12, 13] for additional information on Supersymmetry and the MSSM and [19] for more explanations on mass determinations.

1.1 Standard Model

We know four interactions :

Gravity : First described by Newton as the attractive force between massive objects, this interaction is now explained by General Relativity which links gravity with the curvature of the space-time. The coupling G_N associated to gravity is by far the weakest of the four forces. Nevertheless because the range of gravity is infinite and all charges are of the same sign, this force is the dominant one at large scales (planets, galaxies, universe, . . .)

Electromagnetism : This is the force between electrically charged particles. Its range is infinite as well. However, the presence of particles with opposite charges leads to a “screening” effect over large scales. This force rules many of the interactions of our daily life, from the chemical bonds to communications.

Strong interactions : This is the interaction responsible for the cohesion of the nucleus (and of all the hadrons) and explains the interaction between the components of the nucleon : the quarks and the gluons themselves. This is the strongest force at short distances (fermi $\simeq 10^{-15} m$) but, due to confinement, its range is limited.

Weak interactions : This interaction is responsible for some nuclear phenomena such as beta decay. Its range is limited since the carriers of the interactions (the Z and W^\pm bosons) are massive.

The Standard Model describes these interactions between the constituents of the matter (and between the carriers themselves !) at the quantum level. The gravity is not included in the SM. At small scales (but not too small !!) gravity is so weak compared to the other three forces that it can be safely neglected, something that we systematically do when computing cross-sections and decays of particles in high-energy experiments. Moreover, including gravity as one of the gauge theories in the SM becomes difficult, since the quantum description of General Relativity is not renormalisable.

In this presentation of the Standard Model we will focus our attention on the electroweak sector, and introduce the Higgs via the spontaneous symmetry breaking. For completeness, we also provide a short description of the strong sector, i.e., of Quantum Chromo Dynamics (QCD).

1.1.1 Electroweak interactions before symmetry breaking

In the year sixties, Glashow, Weinberg and Salam [28, 29, 30] proposed a renormalisable Yang-Mills theory based on the gauge groups $SU(2)_L \times U(1)_Y$ to describe

electroweak phenomena at scales of order $\Lambda_{EW} \approx 250$ GeV. The vectorial fields associated with the generators of the group mediate the electroweak interaction. The field B_μ is related to the generator Y of $U(1)_Y$ and the fields W_μ^i are related to the three generators T^i of $SU(2)_L$ defined as

$$[T^a, T^b] = i\epsilon^{abc}T^c. \quad (1.1)$$

The associated tensor fields read

$$W_{\mu\nu}^a \equiv \partial_\mu W_\nu^a - \partial_\nu W_\mu^a + g_L \epsilon^{abc} W_\mu^b W_\nu^c, \quad (1.2)$$

$$B_{\mu\nu} \equiv \partial_\mu B_\nu - \partial_\nu B_\mu, \quad (1.3)$$

where g_L is the coupling constant of $SU(2)_L$. The purely gauge part of the Lagrangian is given by

$$\mathcal{L}_G = -\frac{1}{4} W_{\mu\nu}^a W_a^{\mu\nu} - \frac{1}{4} B_{\mu\nu} B^{\mu\nu}. \quad (1.4)$$

Concerning the matter fields, the theory contains three generations of left and right-handed chiral quarks and leptons with $\psi_{R,L} \equiv (1 \pm \gamma_5)\psi$. Left handed fermions transform as $SU(2)_L$ doublets (noted Q_L for quarks and L_L for leptons) while right-handed fermions transform as singlets of $SU(2)$ (generically noted u_R, d_R for quarks and e_R for leptons¹).

Gauge and matter sectors are minimally coupled through the kinetic terms

$$\mathcal{L}_D = i\bar{L}_L^j D_\mu \gamma^\mu L_L^j + i\bar{Q}_L^j D_\mu \gamma^\mu Q_L^j + i\bar{u}_R^j D_\mu \gamma^\mu u_R^j + i\bar{d}_R^j D_\mu \gamma^\mu d_R^j + i\bar{e}_R^j D_\mu \gamma^\mu e_R^j \quad (1.5)$$

where j stands for the three generations of quarks and leptons and the covariant derivative D_μ is defined as

$$D_\mu \equiv \partial_\mu - ig_L T_a W_\mu^a - ig_Y \frac{Y}{2} B_\mu, \quad (1.6)$$

with g_Y the coupling constant of the $U(1)_Y$ gauge group.

The Lagrangian $\mathcal{L}_G + \mathcal{L}_D$ is not self-sufficient to completely describe the electroweak interactions since it cannot explain the observed masses for the W^\pm and Z gauge bosons. Those masses are important to explain the limited range of the weak interaction. However adding a direct mass term for those gauge bosons would explicitly break the gauge invariance of the theory. As explained in the next section, this issue can be addressed in an elegant way by the mechanism of spontaneous symmetry breaking, the so-called Brout-Englert-Higgs mechanism [31, 32, 33].

1. To simplify, I consider a "strict" version of the Standard Model in which neutrinos are massless. In this case the right handed neutrino is not introduced in this Lagrangian.

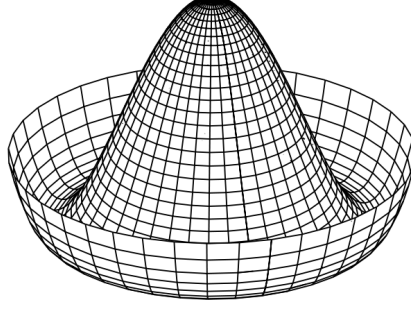


FIGURE 1.1 – Form of the Higgs potential

1.1.2 The Brout-Englert-Higgs mechanism

The Brout-Englert-Higgs (BEH) mechanism adds a new gauge invariant scalar sector to the theory. To be able to give mass to the gauge bosons, the potential of this sector should present more than one minimum. By symmetry, those minima should transform into each other under the gauge symmetries. Since the expansion of the vacuum should be done around a single minimum, this expansion cannot preserve the symmetry anymore. The interest of such a breaking, qualified of spontaneous, is that the degrees of freedom linked to transformations of one minimum into another (called Goldstone bosons) can be re-interpreted –as we will see– as the longitudinal part of the gauge boson corresponding to the broken generators. In addition to those gauge bosons, the BEH mechanism requires the presence of at least one physical scalar (called the Higgs) linked to the non trivial value for the vacuum expectation value.

In the Standard Model, three of the four electroweak gauge bosons are massive. As a consequence, at least three scalars are needed in addition to the one triggering the BEH mechanism. One minimal solution which breaks the full group $SU(2)_L \times U(1)_Y$ to $U(1)_{EM}$ is to choose the new sector as a doublet representation of $SU(2)_L$

$$H \equiv \begin{pmatrix} H^1 \\ H^0 \end{pmatrix} \equiv \frac{1}{\sqrt{2}} \begin{pmatrix} i(\pi^1 + i\pi^2) \\ \sigma + i\pi^3 \end{pmatrix}. \quad (1.7)$$

The Higgs doublet couples to the gauge sector of the SM through the kinetic term of the most general gauge invariant renormalisable Lagrangian

$$\mathcal{L}_S = (D^\mu H)^\dagger D_\mu H + \mu^2 H^\dagger H - \lambda(H^\dagger H)^2. \quad (1.8)$$

By enforcing the positivity of the μ and λ parameter, the potential has a “mexican hat” shape (see Fig. 1.1) which fulfills the condition for the BEH mechanism. The

minimum of the potential in \mathcal{L}_S can always be rotated to

$$\langle H \rangle = \frac{1}{\sqrt{2}} \begin{pmatrix} 0 \\ v \end{pmatrix} \quad (1.9)$$

with a $SU(2)_L \times U(1)_Y$ gauge transformation, and $v = \sqrt{\mu^2/\lambda}$ which corresponds to the field value at the potential minimum.² The gauge boson mass spectrum is then established from $|D^\mu \langle H \rangle|^2$ which contains the following term :

$$\frac{v^2}{8} (g_Y B_\mu - g_L W_\mu^3)^2 + \frac{g_L^2}{4} v^2 W^+ W^- \quad (1.10)$$

with $W_\mu^\pm \equiv \frac{1}{\sqrt{2}} (W_\mu^1 \mp iW_\mu^2)$. The mass of the charged gauge bosons is therefore given by

$$m_W = \frac{1}{2} g_L v. \quad (1.11)$$

On the other hand W_μ^3 and B_μ mix into two physical gauge bosons, the photon A_μ and the boson Z_μ

$$\begin{pmatrix} A_\mu \\ Z_\mu \end{pmatrix} = \begin{pmatrix} \cos \theta_W & \sin \theta_W \\ -\sin \theta_W & \cos \theta_W \end{pmatrix} \begin{pmatrix} B_\mu \\ W_\mu^3 \end{pmatrix}, \quad (1.12)$$

with masses

$$m_A = 0, \quad \text{and} \quad m_Z = \frac{m_W}{\cos \theta_W}. \quad (1.13)$$

In those equations the weak angle θ_W is defined by $\tan \theta_W = g_Y/g_L$. Additionally the Higgs doublet in the SM allows a Yukawa term in the Lagrangian which, after spontaneous symmetry breaking, provides mass terms to the fermions.

It also should be noted that in 1973, Llewellyn-Smith demonstrated with a few hypothesis (mainly renormalisability and unitarity), that the electroweak sector requests the presence of at least one scalar. He also computed the required relation between the scalar(s), the gauge boson and the fermions. Those relations corresponds to a spontaneous symmetry breaking of the theory [34].

1.1.3 Strong interactions

As in the electroweak sector, the strong interactions are described by a renormalisable Yang-Mills theory based on a gauge group which in this case is $SU(3)_c$ [35, 36]. This

² The vacuum expectation value is fixed experimentally by the measurement of the coupling in the Fermi interaction. Therefore, the only free parameter of the Standard Model is the mass of the Higgs boson h^0 –the particle associated to the expansion of σ around the vacuum– since $m_{h^0}^2 = -\mu^2 + 3\lambda v^2$.

theory describes the interactions of quarks carrying colour quantum numbers. The gluons –the vectors of the interaction– are the vectorial fields G_μ^a corresponding to the eight generator \bar{T}^a of the $SU(3)$ group.

The Lagrangian corresponding to the QCD sector reads³

$$\mathcal{L}_{QCD} = -\frac{1}{4}G_{\mu\nu}^a G_a^{\mu\nu} + i\bar{q}^j \gamma^\mu D_\mu q^j, \quad (1.14)$$

where j stands for the 6 different quark flavours and $G_{\mu\nu}^a$ and D_μ are defined as

$$G_{\mu\nu}^a \equiv \partial_\mu G_\nu^a - \partial_\nu G_\mu^a + g_s f^{abc} G_\mu^b G_\nu^c, \quad (1.15)$$

$$D_\mu \equiv \partial_\mu - ig_s \bar{T}_a G_\mu^a. \quad (1.16)$$

Contrary to the W^\pm and Z boson, the experimental gluon mass is compatible with zero [37]. Therefore, the theory does not call for any spontaneous symmetry breaking. Another important property of the strong sector comes from the β function of the Renormalisation Group Equation which is negative –due to the self interactions– leading to stronger interactions at lower energies (and so to confinement) and to asymptotic freedom at high energies. This last property allows us to make reliable perturbative predictions at high-energy colliders.

1.2 The quest for the Higgs

As stated in the previous section, the Higgs is the last missing piece of the Standard Model. Discovering the Higgs is then of central importance since it will transform the SM into a fully determined theory which is in “nearly” perfect agreement with basically all the current experimental information.

In this section we present some of the theoretical considerations restricting the Higgs mass range, before going over the researches done at LEP, TEVATRON and the one expected at LHC. We will conclude this section by presenting the information on the Higgs mass coming from the Electroweak precision measurements.

1.2.1 Theoretical constraints

If we try to describe the fermion scattering at high energy with the Fermi interaction, the cross section –proportional to the centre of mass energy (\sqrt{s})– breaks the unitarity

³. Note that the Dirac kinematic term has some redundant factor with Eq. (1.5). Therefore, the SM Lagrangian is not the sum of the two Lagrangian.

bounds around $\Lambda_{EM} \simeq 200$ GeV. The Glashow-Weinberg Salam theory resolves this problem through the existence of the W^\pm . But this moves the unitarity problem to higher energy and to other processes like $e^+e^- \rightarrow W^+W^-$ and $W^+W^- \rightarrow W^+W^-$.

In the SM the Higgs plays the same role as the W^\pm for the Fermi interaction, it provides negative interference such that the unitarity breaking behaviour of the cross-section is cancelled by its contribution. The first partial wave⁴ for the amplitude $W^+W^- \rightarrow W^+W^-$ process can be estimated by

$$a_0 \approx \frac{-m_{h^0}^2}{8\pi v^2}, \quad (1.17)$$

in the limit where $s \gg m_W^2, m_{h^0}^2$. The optical theorem ($|Re(a_l)| < 1/2$), induces then a maximal bound for the Higgs Mass $m_{h^0} \lesssim 870$ GeV. A combined analysis of all $2 \rightarrow 2$ scattering processes involving gauge and Higgs bosons gives a slightly more stringent bound of about 710 GeV.

Besides these unitarity limits, the requirement that all processes involving the Higgs boson can be consistently described with a perturbative expansion also leads to restricts on m_{h^0} . One of them starts from the Higgs partial decay width into pairs of gauge bosons, which grows proportionally to the cube of the Higgs mass. The one loop corrections [38], for instance, are of the same order as the Born tree-level contribution for $m_{h^0} \approx 10$ TeV, while the two loop corrections can be larger than the one-loop correction already for $m_{h^0} \approx 1$ TeV. More complete calculations [39] have led to a definitive upper limit at about 700 GeV, which is in surprisingly good agreement with the naive estimate obtained from a perturbative approach to unitarity.

1.2.2 LEP exclusion

At LEP the SM Higgs was supposed to be produced mainly in the s-channel Higgsstrahlung channel : $e^+e^- \rightarrow Z \rightarrow h^0Z$, where the Z can be either virtual (LEPI) or real (LEPII). The cross-section of this process as a function of \sqrt{s} and m_{h^0} is presented in Fig. 1.2.

The different Higgs decay modes and their branching ratios are displayed in Fig. 1.3. For a mass below 140 GeV, the Higgs decays mainly in pair of fermions, especially in $b\bar{b}$ (more than 80% of the decays). For higher Higgs mass the W^+W^- and ZZ

4. The partial wave for the amplitude are defined as

$$a_J(s) = \int d\cos\theta P_J(\cos\theta)\mathcal{M}.$$

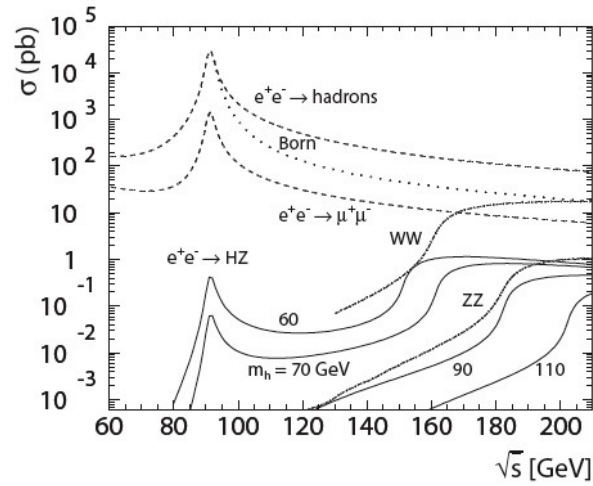


FIGURE 1.2 – Cross sections of the Higgs-strahlung production mechanism in e^+e^- collisions as a function of \sqrt{s} and m_{h^0} . The main background processes are also shown in dashed lines. From Ref. [40].

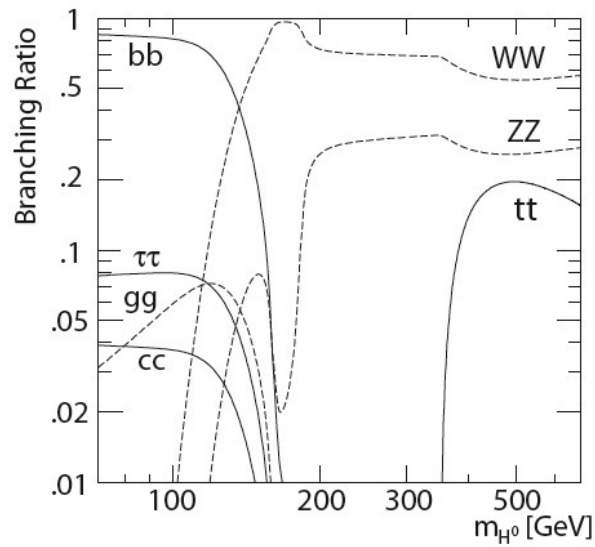


FIGURE 1.3 – Branching ratios for the SM Higgs boson decay as a function m_{h^0} . From Ref. [40].

modes are dominant and the decay width grows quickly with m_{h^0} . Considering this production and the associate decay modes, the most interesting final state topologies for a Higgs mass around 100 GeV are :

Fully hadronic decay with process $e^+e^- \rightarrow (h^0 \rightarrow b\bar{b})(Z \rightarrow q\bar{q})$. This channel represents 60% of the total branching ratio. With this channel the Higgs mass can be reconstructed with a precision of order 2.5 GeV.

Missing energy in $e^+e^- \rightarrow (h^0 \rightarrow b\bar{b})(Z \rightarrow \nu\bar{\nu})$, the missing E_T cut authorises to get rid of the main background, providing a resolution of the order of 3 GeV.

Semi-leptonic production , $e^+e^- \rightarrow (h^0 \rightarrow b\bar{b})(Z \rightarrow l^+l^-)$ where l^\pm is either electron or muon particle. This channel has a rather small branching ratio ($\approx 6\%$) but a rather low background leading to a good energy resolution (1.5 GeV).

In each of these discovery channels the main problem is to disentangle the signal from the background which has identical final states and –quite often– larger cross-sections than the signal. The difference in the kinematics between signal and background encourages to apply selection cuts. For instance, $e^+e^- \rightarrow (h^0 \rightarrow b\bar{b})(Z^0 \rightarrow \nu\bar{\nu})$ and $e^+e^- \rightarrow Z/\gamma \rightarrow b\bar{b}$ are easily separable due to the presence of large missing energy in the first case and not in the second. Applying a E_T cut then provides a sample of events with virtually no background. The mass distribution of the pair $b\bar{b}$ would then present a peak at the Higgs mass.

The final result of these studies is an exclusion –at 95% confidence level– of a Standard Model Higgs with a mass lower than 114.4 GeV [9].

1.2.3 Tevatron exclusion

In opposition to LEP, the TEVATRON is a proton/anti-proton collider. As a consequence the main production mode for a Higgs is gluon fusion (through a top loop). In this case the most promising discovery channels are those where the Higgs decays in two W for $m_{h^0} \gtrsim 2m_W$. If the Higgs is significantly lighter than $2m_W$, it decays mostly in $b\bar{b}$, faces so a large background that the Higgs-strahlung production with $h^0 \rightarrow b\bar{b}$ (or $h^0 \rightarrow WW^*$) turns out to be the most promising discovery channel.

As with LEP, the main problem is to disentangle the signal and the background. At hadron colliders this is even harder due to the presence of large QCD radiation and that the centre of mass of the partonic process is not fixed. In this case, more advanced analysis techniques are necessary.

As an example, let us mention that TEVATRON experiments normally use Neural Network techniques to discriminate the signal from the background. The neural network takes a series of inputs such as the momenta of particles, the tagging of heavy flavour,

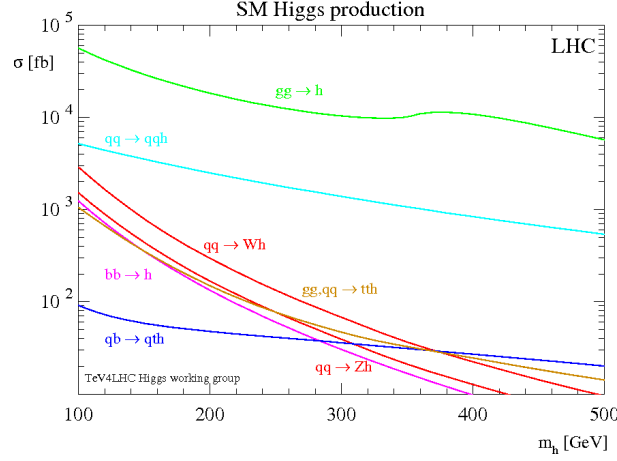


FIGURE 1.4 – Cross-section for Higgs boson production at the TEVATRON (Run II). From [41].

the value of the square matrix element associated to this event (See Eq. 2.3), ... and combines them in a non-linear formula in order to return a single number : zero or one. The formula is obtained by training the neural network on Monte-Carlo data. i.e., the formula is adapted iteratively in order to maximise the occurrence of a correct answer that the Monte-Carlo returns the correct answer (one for signal and zero for the backgrounds) [42].

At the time of this work, CDF collected and analysed $5.9fb^{-1}$ of data while $D\emptyset$ reaches $6.7fb^{-1}$. The combined results –for all channels and for both experiments– leads to the exclusion at 95 % of confidence level of a Standard Model Higgs between 158 and 175 GeV [2] (see Fig. 1.5).

1.2.4 LHC searches

The LHC is a proton-proton collider running at higher energy (designed for 14 TeV but currently running at 7 TeV). As a consequence, the main production mode for a Higgs (See Fig. 1.6) are gluon fusion and the weak boson fusion. Gauge boson associated production is suppressed due to the absence of valence anti-quarks in the proton.

Depending on its mass, the Higgs can be discovered in different channels. In the very low mass region ($m_{h^0} \lesssim 130$ GeV) the $gg \rightarrow h^0 \rightarrow \gamma\gamma$ process is probably the only useful discovery mode with a very clear signature but with a very small cross section

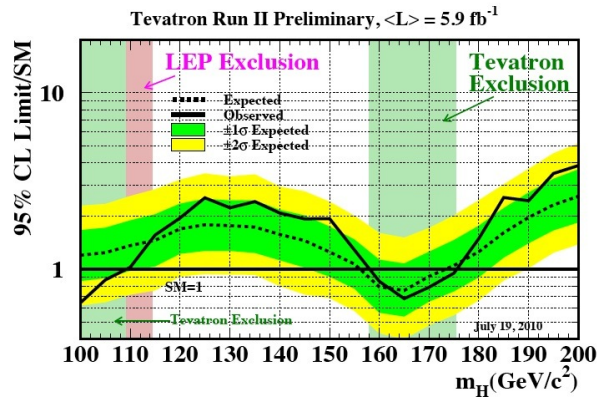


FIGURE 1.5 – Observed and expected 95% confidence level upper limit on the ratio to the SM cross section as a function of the Higgs mass.

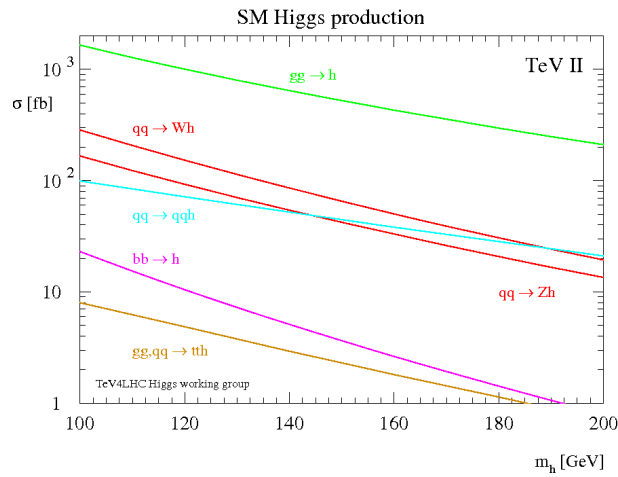


FIGURE 1.6 – Cross-section for Higgs boson production at the LHC ($\sqrt{s} = 14 \text{ TeV}$). From [41].

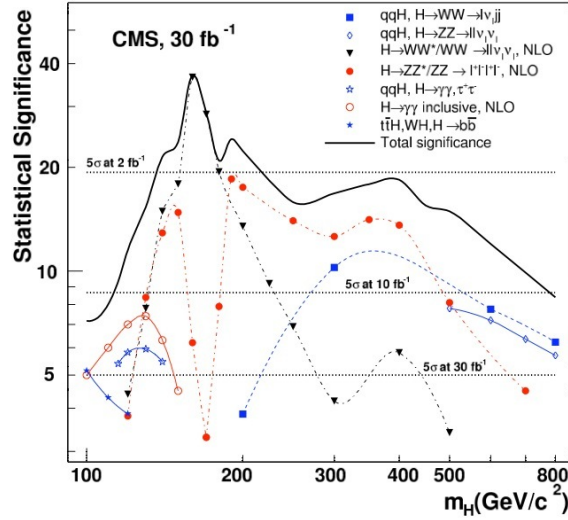


FIGURE 1.7 – CMS expected discovery potential for the SM Higgs boson at 14 TeV with 30 fb^{-1} in luminosity.

and a large background. Above the $2m_Z$ threshold, the golden channel $gg \rightarrow h^0 \rightarrow ZZ \rightarrow 4l$ should allow for Higgs detection up to masses of order 1 TeV. In the mid-region ($130 \lesssim m_{h^0} \lesssim 180 \text{ GeV}$) the $gg \rightarrow WW^{(*)} \rightarrow l^+l^-\nu\bar{\nu}$ mode turns out to be the best option by offering a sizeable rate together with good background rejection possibilities.

As shown in Fig. 1.7 the LHC was originally built such that the Standard Model Higgs can be found whatever the Higgs mass. If the LHC continues to run at 7 TeV for about one year, he is expected to reach quite similar sensitivity as the current one of the TEVATRON (See Fig. 1.8).

1.2.5 Indirect constraints from precision measurements

Independently of direct searches, there are other ways to indirectly determine or constraint the mass of the Higgs boson. The Higgs can be produced in loops, and then precise measurements can be sensitive to the Higgs mass. This method was used by the LEP experiment to determine the mass range for the top-quark mass before its discovery [43].

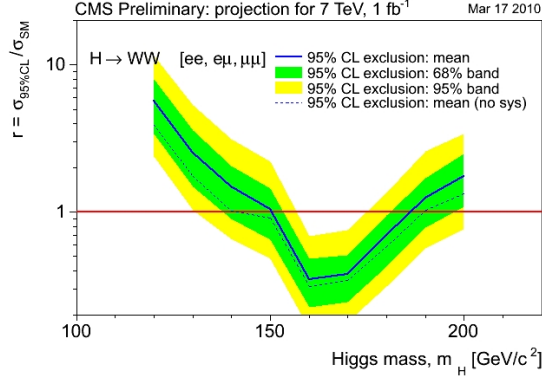


FIGURE 1.8 – CMS expected discovery potential for the SM Higgs boson at 7 TeV with 1 fb^{-1} in luminosity.

In order to restrict the Higgs boson mass range by studying radiative corrections to electroweak parameters, one first needs to select a proper renormalisation scheme. We selected the Veltman scheme [44] where the free parameters are g_L and $\sin \theta_W$. Consequently the relation $m_W = m_Z \cos \theta_W$ is no longer valid beyond tree-level. To study the deviation to this relation, it's usual to use the ρ parameter defined as

$$\rho \equiv \frac{m_W^2}{m_Z^2 \cos^2 \theta_W}. \quad (1.18)$$

The accidental presence of a $SU(2)_L \times SU(2)_R$ global symmetry in Eq. (1.8) [45] has important phenomenological consequences. Indeed, as demonstrated in [46] the ρ parameter can be linked in a suitable gauge to the ratio of the renormalisation constants for the Goldstone fields $\pi^1 \pm \pi^2$ and π^3 . Since these fields transform as a triplet under $SU(2)_V$ –the remaining symmetry after the spontaneous symmetry breaking which is called *custodial symmetry*– these renormalisations are kept constant and $\rho = 1$ at all orders of perturbation as long as pure scalar interactions are present.

Unlike to the pure scalar part of the Lagrangian, both gauge and Yukawa interactions (if up and down quark are not degenerated) break the custodial symmetry. In the one loop corrections to the ρ parameter there is a quadratic dependence in both heavy fermions and gauge bosons masses and only a logarithmic dependencies for the Higgs mass. For the explicit details on the $\Delta\rho$ corrections at one loop in the Standard Model,

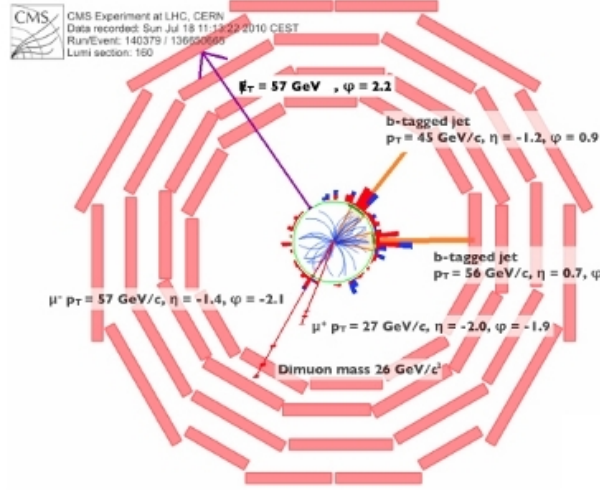


FIGURE 1.9 – One of the first top candidates observed in the CMS detector.

the interested reader is invited to consult original works [44,47,48] or the review [49].

$$\Delta\rho_{top} \approx \frac{3G_F}{8\sqrt{2}\pi^2} m_t^2, \quad (1.19)$$

$$\Delta\rho_h \approx -\frac{3G_F}{8\sqrt{2}\pi^2} \tan^2 \theta_W m_W^2 \log \frac{m_{h^0}^2}{m_W^2}. \quad (1.20)$$

Those equations link m_t , m_{h^0} , m_W and $\sin^2 \theta_W$ in a non trivial way. A global fit [8] shows that the preferred value is $m_{h^0} = 76_{-24}^{+33} GeV$. Similar studies based on likelihood ratios [50] show equivalent results.

As emphasized in [51], the two most accurate measurements of $\sin \theta_W$ do not agree very well, leading to conflicting predictions for the Higgs mass. The rather large value obtained for the $b\bar{b}$ asymmetry at LEP favours a relatively heavy Higgs ($m_{h^0} = 420_{-190}^{+420} GeV$) while the $\sin^2 \theta_W$ value extracted at SLD [52, 53] favours a lighter Higgs ($m_{h^0} = 31_{-19}^{+33} GeV$) in contradiction with the LEP exclusion bound.

1.3 Top-Quark Mass measurement

As discussed in previous sections, an accurate measurement of the top mass is necessary to give a precise indication of the Higgs mass. Since it is the heaviest particle known so far it provides the largest contribution to loop corrections.

CMS and ATLAS have already collected their first top candidate events (see Fig. 1.9) and started to study the associated physics and particularly the top-quark mass [3]. One of the techniques used to obtain such a measurement is *Kinematical Fitting*. The kinematical fitting technique tries to improve the resolution of the measured quantities and determines the momenta of the invisible particles by imposing a series of well established kinematic hypotheses like the invariant mass of some particles and/or energy-momentum conservation. Due to the uncertainties in the measured quantities, those constraints are not always exactly fulfilled. A chi-square minimisation method –under constraint– is then used to find the optimal kinematical configuration which fulfills the constraints and which agrees with the observed events in the resolution interval.

Let us focus on the top-quark mass measurement made with the Kinematical Fit method on the fully leptonic channel. The chi-square minimisation is performed under the following constraints [3, 19, 20] :

- The invariant mass of the leptons and the neutrino should be equal to the W mass.
- The reconstructed invariant mass for the two tops in the two branches should be identical.
- The kinematics of the events should verify the conservation of energy-momentum.

Since the TEVATRON has run for a longer time, the detector behavior is better characterised, allowing accurate parameterisation of the detector response. In this context, CDF and DØ developed a method to use the maximum of theoretical constraints by using the squared matrix element. This method called the Matrix Element Method [54, 55, 56, 57, 58, 59, 60] builds a likelihood based on the probability to observe a set of events. This probability is the convolution of the squared matrix element with the probability that the parton event evolves in the given signature into the detector. A maximisation of the likelihood leads to the single most precise measurement of the top-mass up to now : 173.3 ± 1.1 GeV [1]. This technique is the main topic of this thesis and will be explained more in details in the next Chapter.

1.4 Physics Beyond the Standard Model

Even though the Standard Model is currently an exceptionally accurate theory both in the electroweak and the QCD sectors, there is a potential theoretical problem in the scalar sector. In the Standard Model written as an effective field theory, the radiative corrections to the Higgs mass are proportional to the square of the cutoff-scale Λ (see [61] for instance) :

$$\delta m_H^2 = \frac{3}{8\pi^2 v^2} (4m_t^2 - 2m_W^2 - 4m_Z^2 - m_{h_0}^2) \Lambda^2. \quad (1.21)$$

The cutoff Λ can be identified with the scale at which some new physics sets in. If the Standard Model is the only valid theory up to where gravity ceases to be negligible then Λ should be of the order of the Planck scale $M_{pl} \sim 10^{19}$ GeV. Radiative corrections for the Higgs mass are then much larger, by many orders of magnitude, than the final mass (which cannot be larger than ~ 800 GeV). In the Standard-Model the only solution is to apply *fine-tuning*, i.e. , to let the bare Higgs mass perfectly balance the radiative corrections. With radiative corrections for $m_{h_0}^2$ of the order of M_{pl}^2 , the bare mass squared should be precisely tuned to more than thirty orders of magnitude. This problem is called the *hierarchy problem*.

Efforts to solve the hierarchy problem are mainly going in three directions :

1. Protecting the Higgs mass from large radiation corrections by introducing some new symmetry. Along this direction we have Supersymmetry [12, 13] (which we will discuss below) and Little Higgs theories [62].
2. Get rid of the large mass hierarchy by approaching the Planck scale from the electroweak scale. This can be achieved by considering large extra dimensions [10, 11]. In these models the Planck scale is actually around 1 TeV. Only gravity is allowed to propagate in the extra dimensions and appears then as the weakest force.
then appears as weak.
3. Make a composite Higgs. This is accomplished for example in Technicolor theories where the electroweak $SU(2)_L$ symmetry is broken dynamically and the Higgs particle corresponds to a condensate of fermions [14, 15].

In addition to the hierarchy problem, there are other reasons for enlarging the SM. For instance, the indications coming from the Cosmological Microwave Background that a large part (80%) of the matter density in the universe consists of non-baryonic slow moving particles [63]. No particle in the Standard Model has the correct characteristics (mass/coupling) in order to fit the cosmological restrictions, and therefore new physics must be introduced.

1.5 Minimal Super-symmetric Standard Model

As explained in the previous section the hierarchy problem can be resolved by adding a new symmetry. One possible solution is Supersymmetry which transforms a boson in a fermion and vice-versa :

$$Q|fermion\rangle = |boson\rangle, \quad Q|boson\rangle = |fermion\rangle. \quad (1.22)$$

Since this symmetry changes the Lorentz representations, the algebra is non trivially connected to the Poincaré group. For example the MSSM has the following algebra ($N = 1$ super-symmetry without any central charges)

$$\{Q, Q^\dagger\} = 2\gamma^\mu CP_\mu, \quad (1.23)$$

$$\{Q, Q\} = \{Q^\dagger, Q^\dagger\} = 0, \quad (1.24)$$

$$[Q, P_\mu] = 0, \quad (1.25)$$

$$[Q, M_{\mu\nu}] = \frac{1}{2}\sigma_{\mu\nu}Q, \quad (1.26)$$

with C being the charge conjugation matrix.

From those relations it is straightforward to demonstrate the following properties (see for example [13]) :

- All particles belonging to the same irreducible representation of super-symmetry have the same mass.
- Any super-multiplet has the same number of bosonic and fermionic degrees of freedom.

This first property is clearly not realised in nature since we do not observe any charged scalar particles with the mass and couplings of the electron. However it is still possible that super-symmetry could be an approximate symmetry which is broken either explicitly or by some spontaneous symmetry breaking of the same type as the BEH mechanism. The super-partners of the Standard Model particles can then differ not only with respect to spin but also to mass, which could then be larger.

The second property implies that every Standard Model fermion should correspond to two scalars (called right/left handed degrees of freedom). The name of those particles starts with a “s” (for scalar) before the name of the SM particle. For example selectron (right/left), stop (right/left), ... Those scalars are also called generically the squarks and the sleptons. For the partners of bosons, the rule is to add the suffix “-ino” like gluino, wino, higgsino, ... The higgsino, the photino and the Zino mix together in mass eigenstates called the neutralinos.

The introduction of those particles solves the instability of the Higgs mass since a loop with fermionic particles enters in the amplitude with a negative sign as compared to

the equivalent bosonic loop. Therefore the quadratic divergences in the corrections to the Higgs mass are exactly cancelled by the presence of the super-partners. This is true to all orders in perturbation theory

$$\delta m_{h^0}^2 \sim \frac{\alpha}{2\pi}(\Lambda^2 + m_B^2) - \frac{\alpha}{2\pi}(\Lambda^2 + m_F^2) + \text{logarithmic divergencies.} \quad (1.27)$$

This cancellation still works when supersymmetry is broken, as long as it is done in a special manner, called *soft super-symmetry breaking* [64].

Another nice feature of super-symmetry occurs if a parity, called R-parity is conserved [65]. R-parity can be defined as $R = (-1)^F(-1)^{B-L}$ where $F = 1$ for fermion and zero for boson, B is the baryon number and L the lepton number. Super-symmetric particles have $R = -1$ and Standard Model particles have $R = 1$. In this case the super-particles can only be produced in pairs. In addition the decay of a any super-particles should have a odd number of super-particles. Then the lightest super-symmetric particles (LSP) is stable. If the LSP is neutral and not strongly interacting, then it is a perfect candidate for cosmological dark matter. Calculations have shown that there are large regions in the super-symmetric parameter space where the LSP has the right mass and coupling to explain the abundance of the observed dark matter [66].

1.6 Characterise new physics

In some specific scenarios, discovering the particles beyond the Standard Model should not be too difficult. In particular when the energy threshold is reached and the cross-section is significant (take for instance squarks and gluinos). Determining the correct BSM scenario, on the other hand, will be quite difficult as it will require the determination of the characteristics of the new particles, i.e., their mass, their couplings and their spins.

The mass is the first quantity that can be obtained from a limited sample of events. As a first step, a theory independent method can be used to determine the mass-spectrum of the theory. In this context, different methods have been proposed to measure the masses of the new states in a model-independent way : specific observables are chosen that are mostly sensitive to the mass of the new heavy resonances entering the decay chains. The final power of a given method is a balance between how well the information of the visible quantities can be used to restrict the unknown masses and the dependence on the experimental and theoretical systematic uncertainties.

Examples in the literature include the end-point method [16] –based on the end-point regions of the invariant mass distributions built from visible particles–, and the polynomial method [67, 68] –attempting to reconstruct the whole event from the visible

momenta. These two methods can also be combined to give a better constraint on the mass spectrum. The M_{T2} method [17, 18], and its recent developments –although based on more complicated observables– also follows the same philosophy. For a recent review on these kinematic methods see [19] and references therein.

The opposite philosophy should be to use the full theoretical information provided by the different scenarios and to discriminate them according to their predictive power on the measured sample. This can be achieved by looking at a specific set of kinematical variables, but also by looking at the probability that the sample could be produced for a given theory. This corresponds to the Matrix Element Method that we will detail in the next Chapter and develop throughout this thesis.

Chapitre 2

Matrix element re-weighting

“We are driven by the usual insatiable curiosity of the scientist, and our work is a delightful game.”

Murray Gell-Mann

In many of the new physics scenarios, like the MSSM described in the previous Chapter, the non Standard Model particles decay very quickly and are not expected to leave any trace in the detector. Hence their existence and properties have to be inferred from the Standard Model particles into which they decay.

The problem of identifying decay patterns and measuring the properties of the new states is particularly intricate when the expected experimental signatures involve a complex final state, typically with several jets, leptons and missing energy. In Chap. 1, we briefly introduced several model-independent techniques which are mostly sensitive to the masses of the new heavy resonances entering the decay chains.

Such strategies will be determinant in restricting the mass spectrum of new resonances. However, *by construction*, most of them will not exploit or provide any information on other properties such as their spin and/or coupling structure. As another example, the precise measurement of the absolute mass of each particle entering a specific decay chain that ends with two missing particles remains challenging, especially in the case of short-length decay chains initiated by proton-proton interactions. In this context, it is useful to consider complementary and model-dependent tools for the investigation of properties of the new physics states.

Here, we will focus on an event by event re-weighting technique which dramatically differs from the methods outlined above, mainly because we made a maximal use of theoretical assumptions. The idea is to associate to each experimental event – characterised by the set of momenta \mathbf{p}^{vis} ¹ – a weight defined as the probability to produce and observe event in a given model, labelled by the letter α .

Let us first evaluate such probability in the ideal situation where the resolution of the detector is perfect. The probability is then given by the theoretical squared matrix element, averaged over the unmeasured quantities : the momenta of the initial and non reconstructed particles (neutrino and/or weakly interacting particles). In consequence the weight reads

$$\mathcal{P}_{ideal}(\mathbf{p}^{vis}|\alpha) = \frac{1}{\sigma_\alpha} \int dx_1 dx_2 f_1(x_1) f_2(x_2) \int d\Phi |M_\alpha(\mathbf{p})|^2 \prod_{i \in vis} \delta(p_i - p_i^{vis}). \quad (2.1)$$

Here f_1 and f_2 are the parton distribution functions, M_α is the theoretical matrix element, $d\Phi$ is the phase-space measure and σ_α is the total cross section, computed with the same matrix element. The normalisation ensures that

$$\left[\prod_{i \in vis} \int d^3 p_i^{vis} \right] \mathcal{P}_{ideal}(\mathbf{p}^{vis}|\alpha) = 1. \quad (2.2)$$

In order to take into account not only the resolution of detector but also the fact that partons will first radiate and then hadronize, the density of probability \mathcal{P}_{ideal} should be reformulated as a convolution between the probability to create an event at partonic level –with momenta \mathbf{p} – and a “transfer function” $W(\mathbf{p}, \mathbf{p}^{vis})$, i.e. the probability for a partonic configuration to evolve to reconstructed momenta \mathbf{p}^{vis} .

$$\mathcal{P}(\mathbf{p}^{vis}|\alpha) = \frac{1}{\sigma_\alpha} \int dx_1 dx_2 f_1(x_1) f_2(x_2) \int d\Phi |M_\alpha(\mathbf{p})|^2 W(\mathbf{p}, \mathbf{p}^{vis}). \quad (2.3)$$

This equation associates a weight to each experimental and allows us to use the full theoretical information but also the experimental one which can improve the sensitivity of measurement. This thesis will focus on this formula and put in evidence its experimental interest.

The practical evaluation of such probability requires first a series of approximations, beginning by considering the tree-level approximation for the squared matrix-element. For the transfer function, it is natural to see it as a product of resolution functions

¹. In general some other information can be used to characterise the events, like particle identification and flavour tagging. In order to have a convenient notation, this will not be written out explicitly.

associated to the energy, the rapidity and the azimuthal angles of each final partonic particle,

$$W(p, p^{vis}) = \prod_{i \in vis} W_i(p_i, p_i^{vis}), \quad (2.4)$$

$$W_i(p_i, p_i^{vis}) = W_i^E(E_i, E_i^{vis}) W_i^\eta(\eta_i, \eta_i^{vis}) W_i^\phi(\phi_i, \phi_i^{vis}), \quad (2.5)$$

where p_i^{vis} , p_i stands for the measured quantities and the phase-space variables associated with the particle i , respectively. A common simplification, linked to the precision of the detector, is to consider a delta-function for all resolution functions but those related to the energy of hadronic object.² The latter are fitted by using Monte-Carlo and validated over control samples.

An important drawback of the parameterisation in resolution functions comes from the implicit one-to-one correspondence between a parton and a reconstructed jet (See Eqs.(2.4) and (2.5)). Two different problems appear due to this correspondence. First, in the case of indistinguishable particles, it is not possible to know in advance which assignment is the correct one. The solution is to average the weight on all possible permutations.³ The second problem arises when the number of reconstructed particles does not correspond to the number of visible particles which is often the case due to the presence of initial (and final) state radiation. We discuss how to treat this case in Chap. 5.

One of the main interests of Eq. (2.3), resides in the the Matrix Element Method (MEM) [54, 55, 56, 57, 58, 59, 60] (see Sec. 4.1) which combines these weights in a likelihood function defined as

$$\mathcal{L}(\alpha) = \prod_{events} \mathcal{P}(p^{vis}|\alpha). \quad (2.6)$$

For instance, the most accurate top-quark mass measurement [69, 70, 71, 72, 73] were achieved with this type of likelihood by the CDF and DØ collaborations. Beyond the use of the matrix re-weighting for the MEM, the event-by-event probability can be used in other types of analyses. It was exploited in the observation of single-top production –via a Template method [74, 75] – and in the determination of the exclusion limits for a Standard Model Higgs with a mass $158 \text{ GeV} < m_H < 175 \text{ GeV}$, as an input to a Neural Network [76].

Let us illustrate the MEM method in an “*idealised*” case : the measurement of the W^\pm mass from the process : $pp \rightarrow W \rightarrow l\nu_l$.⁴ In Fig. 2.1 we show the likelihood for a

2. The τ lepton is of course an exception since it is often considered more as an hadronic object.

3. In general, only one of the permutations has a significative contribution since the wrong permutations have much smaller probabilities due to “wrong” invariant mass. We have checked that in consequence this procedure does not induce a large effect on the precision of the method.

4. Chap. 4 will illustrate the method in more complex cases and in more interesting scenarios.

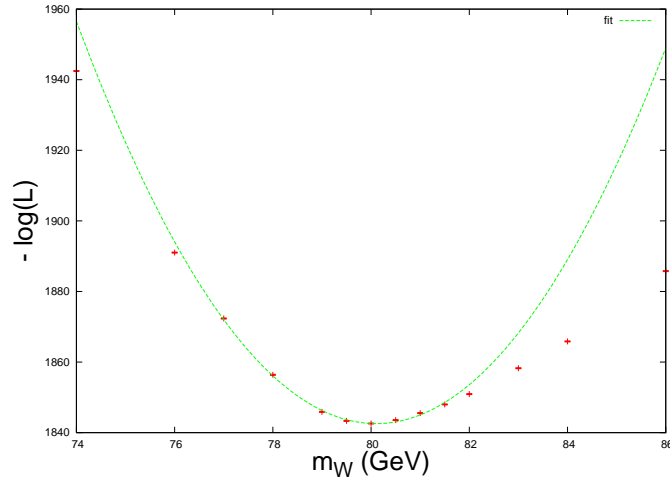


FIGURE 2.1 – Logarithmic likelihood values for a sample of 250 partonic events generated with $m_W = 80$ GeV. The dashed line is a parabolic fit to the points close to the minimum. The statistical error is estimated by the half width of the distribution at $\log(L/L_{\max}) = 0.5$ and is extracted from the fit : $m_W = 80.1 \pm 0.4$ GeV.

sample of 250 Monte-Carlo events – at partonic level and without any background– generated with a test mass of $m_W = 80$ GeV. The displayed curve presents a parabolic behaviour, consistent with a Gaussian distributed likelihood. We use this behaviour to fit to a parabola and accordingly extract the measurement : $m_W = 80.1 \pm 0.4$ GeV. This shows that in an idealised case the estimator is unbiased⁵ and that the method can be used for extremely short decay chains where other methods hardly (or even do not) provide results.

5. We checked that no bias appears at higher luminosity.

Chapitre 3

Computation of the weights : a general method

“Anyone who attempts to generate random numbers by deterministic means is, of course, living in a state of sin.”

John von Neumann

As presented in the previous Chapter, matrix element re-weighting consists in associating a weight to each event, corresponding to the integral described in Eq. (2.3). Such a calculation is very challenging since large variations of the integrands occur not only in the matrix elements – which can be dealt with standard phase-space integrators [77, 78, 79]– but also by the presence of the transfer functions and the associated resolution functions. Such large, fast and non-trivial variation in a high dimensional space cannot be solved either by multi-purpose integrators or by standard phase-space integrators. A dedicated integrator is therefore required.

To explain how to build such an integration algorithm, we will first present different Monte-Carlo techniques, by following the review by Weinzierl [80]. Then we will continue this Chapter by presenting a general strategy –based on those MC techniques– for re-weight events corresponding to any type of decay-chain topologies. This algorithm was implemented in a fully automatic way in the MADGRAPH framework [81]. The corresponding code was dubbed MADWEIGHT [23]

3.1 Monte-Carlo techniques

Monte Carlo (MC) integration is the most efficient numerical integration technique to estimate multi-dimensional integrals. It is the only method where the error decreases like $1/\sqrt{N}$ independently of the number of dimensions. If the number of dimensions is large, it converges more rapidly than a trapezoidal ($N^{-2/d}$) or a Simpson formula ($N^{-4/d}$) [80].

Given a real function $f(\mathbf{z})$ defined in the d -dimensional volume $V = [0, 1]^d$, the basic idea of a Monte Carlo integration is to generate a sample of N random points $\mathbf{z}_1, \mathbf{z}_2, \dots, \mathbf{z}_N$ in this volume according to a uniform distribution in order to approximate the integral $I = \int d\mathbf{z} f(\mathbf{z})$ by

$$E = \frac{1}{N} \sum_{n=1}^N f(\mathbf{z}_n). \quad (3.1)$$

For the discussion of interest, we can restrict ourselves to the case of a positive-definite function f . If this function is sufficiently smooth, the law of large numbers guarantees that this estimator converges to the true value of the integral I for arbitrary large N . The error on the estimator is related to the variance of the function

$$\sigma_I = \frac{\sigma(f)}{\sqrt{N}} \approx \frac{S}{\sqrt{N}}. \quad (3.2)$$

In turn, this variance is estimated by the following estimator :

$$S^2 = \frac{1}{N-1} \sum_{n=1}^N [f(\mathbf{z}_n) - E]^2. \quad (3.3)$$

As an example, and in order to quantify the future improvement of the method, let us consider the following integral : $\int_{-100}^{100} e^{-z^2} dz$. The theoretical value is given by $\sqrt{\pi} \approx 1.77245$, where the variance of the function is $\sigma^2(f) = \int_{-100}^{100} (e^{-z^2} - I)^2 dz \approx 585$. Table 3.1 shows different estimation of the integral for different number of Monte-Carlo points. The estimated as well as the theoretical errors are also given. All values are in agreement, but the error is clearly underestimated.

In the computation of cross sections, one is often led to integrate a scattering amplitude that varies by several orders of magnitude over the region under integration. In that case, the very large variance $\sigma^2(f)$ of the integrand severely limits the convergence of the Monte Carlo integration. One way to improve the convergence is to decrease the factor $\sigma(f)$ appearing in Eq. (3.2) by applying a change of variables $\mathbf{z} \rightarrow \mathbf{z}' = \mathbf{P}(\mathbf{z})$.

Number of points	I	$\sigma(f)/\sqrt{N}$
10^2	3.3 ± 2.3	2.5
10^3	1.3 ± 0.4	0.79
10^4	1.90 ± 0.16	0.25
10^5	1.73 ± 0.05	0.079
10^6	1.758 ± 0.016	0.02
10^7	1.764 ± 0.004	0.007

TABLE 3.1 – Estimation of the integral $I = \int_{-100}^{100} e^{-z^2} dz = 1.77245385$ by Monte-Carlo techniques for a given number of points. The second column provides the theoretical expected error on the estimator.

By defining the Jacobian function $p(\mathbf{z}) = \text{Jac}[\mathbf{P}(\mathbf{z})]$, the integral I can be rewritten in terms of the new variables as follows

$$\int d\mathbf{z} f(\mathbf{z}) = \int \frac{f(\mathbf{z})}{p(\mathbf{z})} p(\mathbf{z}) d\mathbf{z} = \int \frac{f[\mathbf{P}^{-1}(\mathbf{z}')] }{p[\mathbf{P}^{-1}(\mathbf{z}')] } d\mathbf{z}'. \quad (3.4)$$

If we restrict the Jacobian function $p(\mathbf{z}) : [0, 1]^d \rightarrow \mathbb{R}^+$ to be normalised to unity ($\int p(\mathbf{z}) d\mathbf{z} = 1$), we can interpret it as a probability density. The integral I can be estimated from a sample of random points $\mathbf{z}'_1, \mathbf{z}'_2, \dots, \mathbf{z}'_N$ distributed according to the probability density $p(\cdot)$, in which case the estimator E and the new variance S^2 are

$$E = \frac{1}{N} \sum_{n=1}^N \frac{f(\mathbf{z}'_n)}{p(\mathbf{z}'_n)}, \quad (3.5a)$$

$$S^2 = \frac{1}{N-1} \sum_{n=1}^N \left[\frac{f(\mathbf{z}'_n)}{p(\mathbf{z}'_n)} - E \right]^2. \quad (3.5b)$$

The efficiency is increased if the variance in Eq. (3.5b) drops, which is achieved if the probability density $p(\mathbf{z})$ is taken to be proportional to $f(\mathbf{z})$ as much as possible : $p(\mathbf{z}) \approx f(\mathbf{z})/I$. When computing cross sections, the analytical expressions of the required phase-space mappings $\mathbf{z} \rightarrow \mathbf{z}' = \mathbf{P}(\mathbf{z})$ are well-known [82].

3.1.1 Adaptive Monte Carlo techniques

Generally, determining the optimal phase-space mapping for a given integrand is a difficult task because the relevant information on the shape of the integrand may be hidden in complicated expressions. Analytical changes of variables can then be replaced by – or better combined with – an adaptive technique, i.e. an algorithm that learns

about the function as it proceeds and adapts the integration measure using an iterative procedure. VEGAS [83] and MISER [84] are examples of such algorithms. Since MADWEIGHT, our phase-space integrator, uses VEGAS we will concentrate in this section on this specific adaptive method.

To reduce the variance of the estimator, VEGAS tries to approximate at each iteration the optimal density function $p(\mathbf{z}) \approx f(\mathbf{z})/I$ by a series of step functions, *i.e.*, the so-called grids. Due to storage and efficiency requirements, VEGAS uses a separable probability density function in d dimensions :

$$p(\mathbf{z}) = p_1(z^1) p_2(z^2) \dots p_d(z^d). \quad (3.6)$$

If such a parameterisation of the probability density function is appropriate to approximate the shape of the integrand, the adaptive integration procedure speeds up the convergence by decreasing the variance in Eq. (3.5b) through the adjustment of the grid. In the case of a very sharp integrand, this condition is essentially fulfilled provided that the strength of each narrow peak in the integrand is associated with a single variable that in turn can be mapped onto one variable of integration z^i . In that case, the integrand expressed in the parameterisation \mathbf{z} is of the form

$$f(\mathbf{z}) = \left(\prod_{i=1}^d f_i(z^i) \right) \times R(\mathbf{z}), \quad (3.7)$$

where the functions f_i 's may vary abruptly while the "remainder" non-factorizable function $R(\mathbf{z})$ is essentially flat over the region under integration. The probability density function $p(\mathbf{z})$ can be adapted to flatten the peaks of the integrand in Eq. (3.7) by cancelling each sharp function f_i appearing in the numerator of the ratio $f(\mathbf{z})/p(\mathbf{z})$ in Eqs. (3.5).

In order to show the interest of an adaptive technique, we return to our previous example where we tried to evaluate the integral $\int_{-100}^{100} e^{-z^2} dz$. The evaluation of the integral will be done by VEGAS in five successive iterations with a grid adaptation between each iteration. In order to have a fair comparison with Table 3.1, the number of events presented in Table 3.2 is the total number of events used on the five iterations. The integral estimation presented in that table shows a significative improvement of the accuracy of the method.

If the integrand expressed in the phase-space mapping \mathbf{z} presents a structure of sharp peaks that does not follow the factorized form in Eq. (3.7), the adaptive integration procedure is bound to converge slowly. However, if enough information about the shape of the integrand is available, a first change of variables $\mathbf{z} \rightarrow \mathbf{z}' = \mathbf{P}(\mathbf{z})$ that rotates the axes of integration can sometimes be applied such that in the new phase-space

Number of points	I	$\sigma(f)/\sqrt{N}$
10^2	2.8 ± 0.7	2.5
10^3	1.82 ± 0.02	0.79
10^4	1.7720 ± 0.0012	0.25
10^5	1.77248 ± 3.10^{-5}	0.079
10^6	$1.772453 \pm 1.1.10^{-6}$	0.02
10^7	1.77245384 ± 3.10^{-8}	0.007

TABLE 3.2 – Estimation of the integral $I = \int_{-100}^{100} e^{-z^2} dz = 1.77245385$ obtained by VEGAS. The first column indicates the number of points used to evaluate the integral. The last column indicate the error in the case of the non adaptive Monte-Carlo technique.

mapping z' , the importance of each peak in the integrand is controlled by a single variable of integration. After this change of variables is applied, the integrand expressed in the new variables z' is of the form given by Eq. (3.7), and the separable density function $p(z')$ can be successfully adapted to reproduce the shape of the integrand.

3.1.2 Multi-Channel method

Sometimes the integrand presents different peaks f_i in different regions of the domain of integration. Even if each of those peaks can be independently written in the form of Eq. (3.7) ensuring efficient integration of each peak separately, this does not mean that the whole function can be written in such a way. A natural solution is to split the domain of integration in different parts, defined by characteristic functions $\beta_i(z)$, each of which being associated to a single peak f_i and an associated change of variables p_i (numerical and/or analytical). The integral can then be seen as a sum of sub-integrals :

$$\int dz f(z) = \int f(z) dz = \sum_{i=1}^N \int \beta_i(z) f(z) dz \approx \sum_{i=1}^N \sum_j \beta_i(z'^j) \frac{f_i(z'^j)}{p_i(z'^j)}. \quad (3.8)$$

In practice, this expression converges to the correct value, as long as the $\beta_i(z)$ functions are normalised such as

$$\sum_i^N \beta_i(z) = 1. \quad (3.9)$$

But they do not need to be characteristic functions. The use of arbitrary functions for the $\beta_i(z)$ explains the term “channel”, since the integrals is then divided into smaller

integral corresponding to a different structure of the integrand. In order to gain in efficiency, the $\beta_i(\mathbf{z})$ should be chosen in a smart way such that the $\beta_i(\mathbf{z})$'s are close to 1 in the area where the associate change of variable corresponds to the peak structure f_i . A convenient choice is given by [77]

$$\beta_i(\mathbf{z}) = \frac{1}{\text{Norm}(\mathbf{z})} f_i(\mathbf{z}), \quad (3.10)$$

$$\text{Norm}(\mathbf{z}) = \sum_i f_i(\mathbf{z}). \quad (3.11)$$

3.2 Strategy of the integrator

For the computation of the weights, there is generally no simple phase-space parameterisation that maps all the peaks in the integrand and in which the boundaries of the phase-space volume can be easily expressed. Our strategy is to start from a standard parameterisation of the phase-space measure

$$d\Phi = \left(\prod_{i=3}^n \frac{|\mathbf{p}_i|^2 d|\mathbf{p}_i| \sin \theta_i d\theta_i d\phi_i}{2E_i (2\pi)^3} \right) dq_1 dq_2 (2\pi)^4 \delta^4 \left(p_1 + p_2 - \sum_{j=3}^n p_j \right), \quad (3.12)$$

where $i = 3, \dots, n$ labels the final particles. In this parameterisation, the strength of each peak in the transfer function is already mapped onto a single variable of integration, whereas none of the propagator enhancements in the squared amplitude is. Identifying the Lorentz invariants associated with the Breit-Wigner resonances and expressing them as functions of the integration variables in Eq. (3.12) is straightforward. The difficult task is then to invert these functions in order to derive a phase-space measure parametrised by both these Lorentz invariants and the variables mapping the peaks in the transfer function. Along with this inversion, the δ function associated with energy-momentum conservation in Eq. (3.12) has to be resolved in an efficient way.

The requested change of variables can be decomposed in a series of successive changes of variables. In Fig. 3.1 we represent those changes of variables, also called blocks, by boxes. Each box will correspond to an appropriate change of variable¹ in order to generate efficiently the dynamics of the particles contained in the box.

This decomposition in a series of change of variables is already used by phase-space integrators designed for the computation of cross-sections. In that case, those blocks

1. The identity is sometimes an appropriate change of variables.

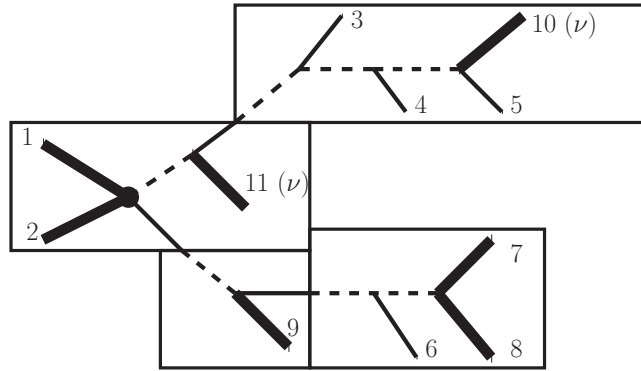


FIGURE 3.1 – Illustration of the structure in blocks optimising the parameterisation of the phase-space measure in the case of a specific decay chain. The missing particles are indicated by the Greek letter ν .

are designed, such that each of them preserves explicitly the energy-momentum conservation. They start to build the set of impulsion of the events by fixing the momenta of the initial particles, and then generate the different particles following the different decay branches. At each step, they use the Breit-Wigner to fix the mass of the decay product, and generates randomly the angles of the decay product. Even if this procedure is extremely efficient for estimating cross-sections –indeed every sharp variation is mapped into a single variable of integration–, this is irrelevant for the matrix-element re-weighting, since it's not possible to adapt this procedure to include the angles of visible particles in the phase-space parameterisation. The associate peaks being extremely narrow –quite often delta functions–, the phase-space integration hardly succeed to converge with this parameterisation of the phase-space.

In consequence, we need to develop a completely new strategy. The idea is to resolve the conservation of Energy-momentum in the last changes of variables (blocks). An unefficiency then occurs since it's not possible to ensure that the conservation of Energy-momentum can be fixed at this stage. If such case happens, we just throw away the points. As long as we don't face this situation too often, the integration process remains efficient. Indeed, generating a point is usually much faster than estimating the corresponding squared-matrix element. In practise this point will not be critical.

Due to our generations choices, we will distinguish two types of blocks : the *primary blocks*, which do not resolve the energy momentum conservation, and the *Final blocks* which resolve energy-momentum conservation leading to the final parameterisation of

the phase-space. In the next two Sections, we will discuss these changes of variables. Then we will see how we choose and combine them.

3.3 Primary change of variables

Each Primary Block (PB) starts with the standard parameterisation of the phase-space measure associated with the m external legs contained in the block,

$$\prod_{i=1}^m \frac{|\mathbf{p}_i|^2 d|\mathbf{p}_i| \sin \theta_i d\theta_i d\phi_i}{2E_i (2\pi)^3}. \quad (3.13)$$

Notice that we choose to never include x_1 and x_2 in a primary block since those quantities are strongly related to the total energy in the process and are not related to any sharp variation of the integrand. It is then a natural choice to leave those variables for the final block.

The change of variables of the simplest block is just the identity, in which case the variables in this block are maintained in the parameterisation of the phase-space measure in Eq. (3.13). For the purpose of listing the other changes of variables that we have investigated, it is useful to represent a block and its corresponding change of variables by a diagram in the following way :

- The variables involved in the transformation are written explicitly. The legs associated with the initial variables appear as thick lines. The legs associated with the final variables –which correspond to the invariants that enter into the expression of specific propagators– are shown as dashed lines.
- A blob stands for a branch of legs of which total momentum parametrises the change of variables related to the block.

In this representation, a blob can a priori be itself decomposed into several primary blocks. However, the change of variables associated with a given primary block is only parametrised by the total momentum of each branch represented by a blob, it does not depend on the details of these branches.

As the detector has an excellent precision on the direction of all visible particles, it's important to preserve those variables in the final parameterisation of the primary blocks. On the contrary, undetected particles such as the neutrino are not constrained by any transfer functions² and removing these variables of the integrand parameterisation

2. Since these particles are not measured, no transfer functions are associated to them. A common mistake is to consider the missing energy as a measurement, but this quantity is roughly the sum of all the observed particles in the process. Including this as a measurement and associating to it a transfer function is then like a double counting of the visible particles measurement.

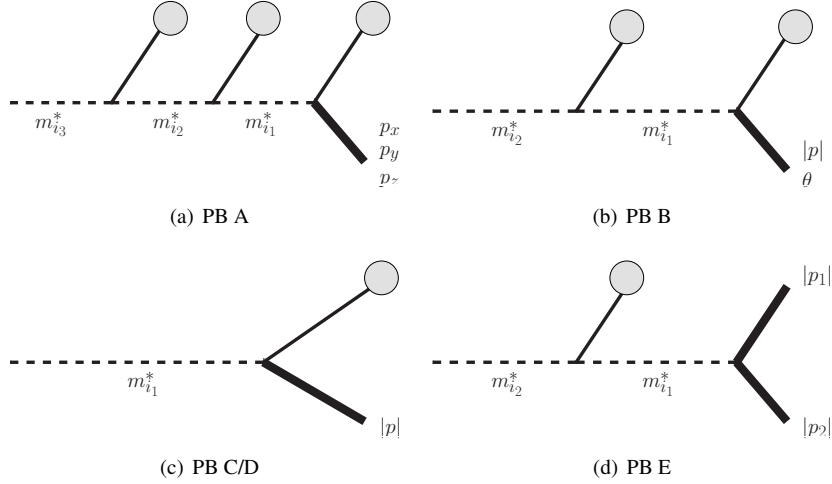


FIGURE 3.2 – The four primary blocks with their corresponding change of variables. Initial (resp. final) variables are written explicitly, and the corresponding legs are represented by thick lines (resp. dashed lines).

can improve by a huge factor the convergence of the integral. Finally since some of the particles can have poor resolution in the energy, replacing this variable by an invariant mass can sometimes improve the estimation of the integrals.³

Additionally, the number of implemented blocks in our algorithm is reduced by our requirement of analytically invertible changes of variables. For an arbitrary phase-space point, given the momenta of all the legs ending by the blobs and the invariant mass of each leg represented by a dashed line in the reduced diagram, the variables in the final block are determined by means of analytical expressions. We checked that the analytical change of variables -when it exists- is faster than the numerical counterpart.

These blocks are displayed in Fig. 3.2. The changes of variables associated with each block are discussed in Section A.2 of the Appendix.

PB A. The transformation removes the 3-momentum of a missing particle from the set of integration variables in the parameterisation of the phase-space measure. The new integration variables are the Lorentz invariants $m_{i_1}^*$, $m_{i_2}^*$ and $m_{i_3}^*$ associated with the first, second and third mother particles of this missing particle.

³. Using such type of transformation is not optimal since this means that some of the variation of the integral cannot be mapped in the new parameterisation. Section 3.5 provides a discussion of the interest of such change of variables.

- PB B.** The transformation removes the energy and the polar angle of a missing particle from the set of integration variables in the parameterisation of the phase-space measure. The new integration variables are the Lorentz invariants $m_{i_1}^*$ and $m_{i_2}^*$ associated with the first and second mother particles of this missing particle.
- PB C/D.** The transformation removes the energy of a missing particle from the set of integration variables in the parameterisation of the phase-space measure (version C). The new integration variable is the Lorentz invariant $m_{i_1}^*$ associated with the mother particle of this missing particle. In version D of this block, the missing particle is replaced by a visible particle, but the transformation remains the same one.
- PB E.** The transformation removes the momenta $|\mathbf{p}_1|$ and $|\mathbf{p}_2|$ of two visible particles produced by the same resonance from the set of integration variables in the parameterisation of the phase-space measure. The new integration variables are the Lorentz invariants $m_{i_1}^*$ and $m_{i_2}^*$ associated with the first and second mother particles of these visible particles. The corresponding change of variables is invertible analytically only if at least one of the two visible particles is massless.

3.4 Change of variables fixing the conservation of energy-momentum

After having applied the different primary blocks, the parameterisation of phase-space not linked to any Primary blok reads

$$\prod_{i=1}^m \frac{|\mathbf{p}_i|^2 d|\mathbf{p}_i| \sin \theta_i d\theta_i d\phi_i}{2E_i (2\pi)^3} dx_1 dx_2 \delta^4 \left(p_1 + p_2 - \sum_{j=3}^n p_j \right), \quad (3.14)$$

where m is the number of external particles which are not in any of the primary blocks. By construction the main interest of the final block is to restore the energy-momentum conservation. In order to see how this is done in practice, we will study two specific cases before treating the general case.

Fully reconstructed process. We first consider a topology with no missing particle. An example of such a decay chain is illustrated in Fig. 3.3(a). In order to restore energy momentum conservation in this case, we need four independent variables that can be fixed accordingly. Since the fractions of the beam energy taken by the two initial parton are not linked to any sharp dependencies should be two of these variables. For the final states particles –and especially for jets–, the resolution in energy is much

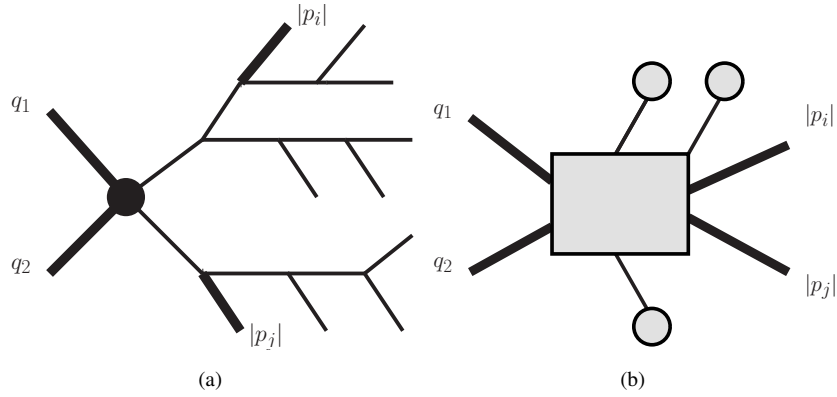


FIGURE 3.3 – Illustration of a decay chain with no missing particle : (a) the full topology, (b) the corresponding reduced diagram. The variables in the final block are written explicitly.

poorer than the resolution in angles. For this reason, a relatively efficient choice is to complete the final block by adding two momentum variables $|\mathbf{p}_i|$ and $|\mathbf{p}_j|$ of particles i and j that are relatively less constrained by the transfer function. In this example, the final block contains exactly four variables, and the effect of the variable transformation is to integrate out the δ function with these four variables.

Process with one unreconstructed particles. We next move on to the case of a decay chain including missing particles in the final state. The phase-space variables associated with the momenta of missing particles are not directly constrained by the transfer function. Therefore they do not need to be mapped onto variables of integration in the phase-space mapping. We can identify the final block by selecting the momentum components of some missing particles instead of the energies of visible particles. A specific example of a topology with missing particles is displayed in Fig. 3.4(a). One way to define the final block is to choose the set including the Bjorken fractions and the momentum components of the missing particle shown as a thick line in Fig. 3.4(a). The change of variables associated with this final block removes these five variables from the set of integration variables in order to integrate out the δ function in Eq. (3.12) and to map the invariant mass of the resonance decaying into the missing particle onto a variable of integration in the new parameterisation of the phase-space measure.

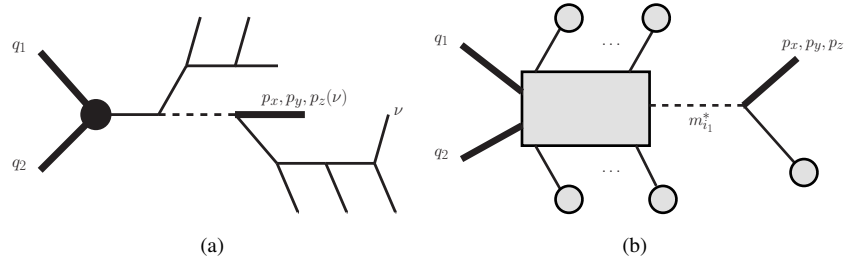


FIGURE 3.4 – Illustration of a decay chain with two missing particles (identified by the letter ν) : (a) the full topology, (b) the corresponding reduced diagram. The initial (resp. final) variables of the transformation associated with the final block are written explicitly, and the corresponding legs are shown as thick lines (resp. dashed lines).

General case. In order to generalise the discussion of the choice of the final block to the case of an arbitrary decay chain, it is useful to introduce a representation of the final block and the corresponding transformation of variables :

- The variables in the final block are written explicitly and the corresponding legs are shown as thick lines.
- An incoming arrow means a momentum which is supposed to be generated by some previous primary blocks (see Sec. 3.3).
- The new integration variables resulting from the change of variables associated with the final block are also written explicitly, and the corresponding intermediate legs are shown as dashed lines.
- All other intermediate legs that do not touch a blob are hidden behind a rectangular box.

We refer to the resulting graph as the *block representation*. As an illustration, the block representation for the two topologies shown in Figs. 3.3(a) and 3.4(a) are displayed in Figs. 3.3(b) and 3.4(b), respectively. In general an incoming line may hide a complicated branch of particles. But the change of variables associated with the final block is parametrised only by the total momentum of those particles by construction.

The presence of the box in the final block, is a source of possible inefficiency. Indeed no mapping can be made in order to compensate the presence of a sharp peak in this part of the diagram. The choice of the final block should always be done in order to minimise the content of this box, in order to reduce as much as possible the possibility of slow convergences.

Each of the final blocks treated in our code is illustrated by a block representation in Fig. 3.5. Their number is restricted because we only keep the final blocks for which

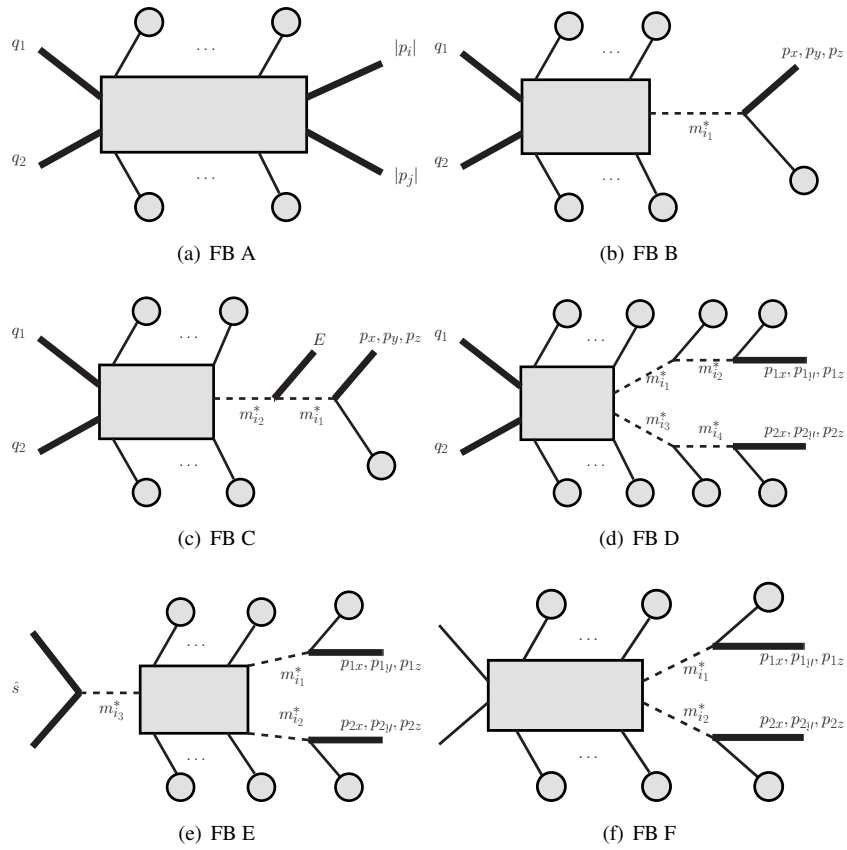


FIGURE 3.5 – The reduced diagrams representing the six final blocks that have been investigated in our procedure.

the corresponding change of variables is invertible analytically. The corresponding formulas are discussed in Appendix. A.1.

FB A. The transformation removes the Bjorken fractions q_1 and q_2 and the norm of the three-momenta $\mathbf{p}_i, \mathbf{p}_j$ of two visible particles from the set of integration variables in the parameterisation of the phase-space measure.

Example : $pp \rightarrow ZZ \rightarrow 4j$.

FB B. The transformation removes the Bjorken fractions q_1 and q_2 and the 3-momentum of a missing particle from the set of integration variables in the parameterisation of the phase-space measure. The new integration variable is the invariant mass of the particle decaying into the missing particle.

Example : $pp \rightarrow Z(W^+ \rightarrow l^+\nu)$.

FB C. The transformation removes the Bjorken fractions q_1 and q_2 , the 3-momentum of a missing particle and the energy of a massless visible particle⁴ from the set of integration variables in the parameterisation of the phase-space measure. The new integration variables are the Lorentz invariants $m_{i_1}^*$ and $m_{i_2}^*$ associated with the mother particles decaying into the missing and the massless particles, respectively.

Example : $pp \rightarrow [t \rightarrow b(W^+ \rightarrow l^+\nu)][\bar{t} \rightarrow \bar{b}(W^- \rightarrow jj)]$ with massless b quarks.

FB D. The transformation removes the Bjorken fractions q_1 and q_2 and the 3-momenta of two missing particles from the set of integration variables in the parameterisation of the phase-space measure. The new integration variables are the Lorentz invariants $m_{i_1}^*, m_{i_2}^*, m_{i_3}^*$ and $m_{i_4}^*$ associated with the first and second mother particles of each missing particle.

Example : $pp \rightarrow [t \rightarrow b(W^+ \rightarrow l^+\nu)][\bar{t} \rightarrow \bar{b}(W^- \rightarrow l^-\bar{\nu})]$.

FB E. The transformation removes the 3-momenta of two missing particles from the set of integration variables in the parameterisation of the phase-space measure. The new integration variables are the Lorentz invariants $m_{i_1}^*$ and $m_{i_2}^*$ associated with the mother particles of each missing particle. The integration over the Bjorken fractions is expressed as an integration over the invariant mass and the rapidity of the colliding partons.

Example : $pp \rightarrow H \rightarrow (W^+ \rightarrow l^+\nu)(W^- \rightarrow l^-\bar{\nu})$.

FB F. The transformation removes the 3-momenta of two missing particles from the set of integration variables in the parameterisation of the phase-space measure. The new integration variables are the Lorentz invariants $m_{i_1}^*$ and $m_{i_2}^*$ associated with the mother particles of each missing particle.

Example : $pp \rightarrow (W^+ \rightarrow l^+\nu)(W^- \rightarrow l^-\bar{\nu})$.

4. In case the particle is massive, the corresponding change of variables turns out to be not analytically invertible.

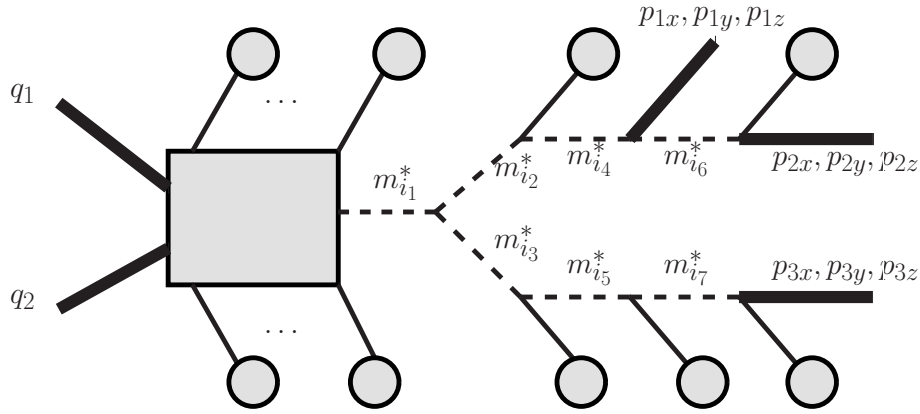


FIGURE 3.6 – A example of reduced diagram for which the transformation that is applied to the FB cannot be inverted by means of analytical formulas.

Limitation of our strategy. It should be stressed once again that each transformation of variables that is applied to the variables in the final block has been implemented in the code analytically : for an arbitrary phase-space point, given the momenta of all the legs ending by the blobs and the invariant mass of each leg represented by a dashed line in the reduced diagram, the variables in the final block are determined by means of analytical expressions. We checked that the analytical change of variables -if it exists- is faster than the numerical counter part. Associated to the fact that analytical changes of variables can efficiently deal with a large class of processes, we did not study further the possibility to use non-analytical changes of variable.

For example, the final block displayed in Fig. 3.6 with three missing particles has not been considered. In principle, the 3-momenta of the three missing particles and the Bjorken fractions could be adjusted to satisfy eleven constraints induced by the seven resonances and the conservation of 4-momentum, but this adjustment cannot be done by means of analytical expressions. In our strategy, this type of situation is dealt with by using a multi-channel method with the most(s) efficient(s) final blocks associated to the process, in this case the final blocks B, C and D will be used.

3.5 Combining the blocks

With the set of primary and final blocks presented in the previous Sections, it is possible to generate efficiently the dynamics of a large variety of processes. Finding this optimal parameterisation is just a matter of testing which combination of the blocks

is the correct one (see Sec. 3.6). But some processes are intrinsically impossible to optimise completely, i.e., put in the form of Eq. (3.7). This is for example the case for top-quark pair production decaying in a semi-leptonic channel. Indeed the number of independent sharp variations in the integrand –nineteen⁵– is larger than the dimension of the integrand –sixteen⁶.

In such a case, we keep several channels and combine them by a multi-channel method (See sec. 3.1.2). The changes of variables that we consider for this multi-channel will be those which have the minimal number of un-aligned peaks. The different channels will correspond to different choices of mapped peaks. For example, the primary block D will always be considered in a multi-channel since it forbids the mapping of the transfer functions associated to energy of the outgoing particle.

In comparison with previous implementations for the evaluation of the matrix element weights, this multi-channel approach speeds up the convergence of the integration in case of an over-constrained topology. The previous topology has been investigated in [70, 71, 85], where either the helicity of the W boson or the mass of the top quark is reconstructed from $t\bar{t}$ events in the semi-leptonic channel. In these analyses, a single channel was used for the evaluation of the weights, leaving unmapped a subset of peaks in the integrand. On the contrary, our procedure always maps a given peak in the integrand onto a variable of integration in at least one channel.

3.6 Finding the appropriate change of variable

With more than 10 different changes of variables, finding the appropriate combination(s) of block in order to achieve the optimised phase-space parameterisation is a non trivial problem in itself. This problem can seem quite easy –after a bit of practise– but is not straightforward to implement in fully automate code. In MADWEIGHT, We have implemented it in a Python Module with the following strategy :

1. Localise the different invisible particles in the process.
2. Identify the two invisible particles (and the two visible particles) which are the closest one of the initial particles. The distance between two particles being defined has the number of s-channel propagators needed to go from one particle to the other.
3. Build a solution based on the final block a (zero neutrino) without using primary block D and E.

5. They are 4 peaks associated to the Breit Wigner of the four propagators, and then 3 peaks associated to the 5 visible particles corresponding to the resolution functions in energy, rapidity and azimuthal angle.

6. The six final particles have 3 degrees of freedom each and each of the incoming parton has one. This makes a total of twenty, but four are correlated due to the conservation of energy-momentum.

4. Build a solution based on the final block b (one neutrino) without using primary block D and E.
5. Build a solution based –depending of the situation– on final block d or e (two neutrinos) without using primary block D and E.
6. Compare those three solutions and select the one –or those– which optimised the number of mapped peaks.
7. If some peaks are left unmapped, we go to in multi-channel mode, and find the other changes of variables linked to the previous solution. Those can be obtained easily by simple equivalence rules. At this stage the blocks D and E are considered for building the different phase-space mappings.

Finally, the code write automatically a series of Fortran code which is used by MAD-WEIGHT in order to know how to make the integration and what the expression of the multi-channel coefficient is.

3.7 One-channel phase-space generator

Given an optimised phase-space mapping defined by its structure in blocks, one can then consider a phase-space generator built upon this phase-space mapping. The generation of an arbitrary phase-space point proceeds in two steps :

1. the generation of the integration variables appearing in the optimised parametrisation of the phase-space measure,
2. the determination of the momentum of each leg in the decay chain and the computation of the Jacobian factors.

Concerning the first step, any variable of integration associated with the new phase-space mappings introduced in the previous Section enters into one of the three following categories :

1. The variable controls the strength of a resolution function. If the resolution function is a δ distribution, the variable is fixed to the value associated with the experimental event. Otherwise, the grid of VEGAS is adapted such that the variable is generated according to a probability density that reproduces approximately the shape of the resolution function.
2. The variable controls the strength of a propagator enhancement. In this case, the variable can be generated according to a probability density that reproduces exactly the shape of the propagator by using the inverse primitive function of a Breit-Wigner.
3. The variable is either the polar or the azimuthal angle of a missing particle. In this case, the variable is generated according to a uniform distribution in the

interval $[0, \pi]$ or $[0, 2\pi]$ at the first iteration. The grid is adapted at each iteration to approximate the optimal probability density.

Once the integration variables have been generated, the kinematics of the whole decay chain and the Jacobian factors are computed. For each block, the formulas that give the expression of the external momenta as a function of the variables of integration are discussed in Appendix. A. These formulas are parametrised by the momentum of the branches represented by the blobs that appear in the graphical representation in Fig. 3.5 and 3.2. For this reason, one needs to fill the kinematic variables in each block in a specific order, starting with the primary blocks at the very end of the decay chain, and ending with the final block.

This procedure is best illustrated with the example in Fig. 3.1. A phase-space point is defined by generating all the integration variables in the transformed expression of the phase-space measure : the invariant mass of each leg are shown as a dashed line, the direction (θ, ϕ) of any visible particle, and the energy of the visible particles are represented by the solid thin lines. Then all other kinematic variables are determined as a function of the generated variables, first in the primary blocks A and E, then in the primary block D (by means of formulas that are parametrised by the kinematics in block E), and finally in the final block B (by means of formulas that are parametrised by the kinematics of all the secondary blocks). Such an approach can be easily generalised to the case of an arbitrary decay chain.

The whole procedure that we have presented so far has been implemented in the Mad-Graph framework, and the corresponding module has been named MADWEIGHT. For a given decay chain and a transfer function for the final state objects, the optimised phase-space mappings are automatically selected, and the resulting multi-channel phase-space generator is used for the evaluation of the weights. While this procedure applies for virtually all cases, the speed of convergence of the numerical integration strongly depends on the process under investigation, and whether the calculation time is a serious limitation or not has to be assessed on a case-by-case basis.

3.8 Validation of the phase-space generator

One potential issue related to our phase-space mappings optimised for the computation of the weights is the fact that some of the associated Jacobians develop singularities in specific phase-space regions. These singular regions are an artefact of the change of variables. In our case they have a null measure in the integration volume. One can therefore split the integration volume into a volume V_1 where the Jacobian is finite and a volume V_2 that contains the singular region and that can be made arbitrary small

l	blocks	integrated volume
3	FB A	6.30×10^{-5}
3	FB B	6.30×10^{-5}
3	FB C	6.30×10^{-5}
6	FB D	694 GeV^6
4	FB E	0.0166 GeV^2
4	FB F	0.0166 GeV^2
5	FB B + PB A	3.89 GeV^4
4	FB B + PB B	0.0166 GeV^2
3	FB B + PB C	6.30×10^{-5}
3	FB B + PB D	6.30×10^{-5}
4	FB B + PB E	0.0166 GeV^2

TABLE 3.3 – Phase-space volumes $\int dq_1 dq_2 d\phi_n 1/(sq_1 q_2)$ for l massless particles produced in hadron-hadron collisions at $\sqrt{s} = 1 \text{ TeV}$. The number l of final-state particles is indicated in the first column. The second and third columns indicate the structure in blocks defining the phase-space mapping used to calculate the volume with our phase-space generator, and the numerical value we obtained. Those numbers correspond to the theoretical expected value up to three digits.

compared to the volume V_1 . To any given accuracy, we can ignore the contribution from the volume V_2 provided that $\epsilon = V_2/V_1$ is sufficiently small. At the numerical level though, one may fear that instabilities will appear in this procedure.

In practice, we have not encountered any numerical instabilities resulting from a change of variables that is associated with a specific phase-space block. Any phase-space block and the related changes of variables that have been defined in our procedure have been checked by reproducing the volume of the entire phase-space region with our phase-space generator using a parameterisation of the phase-space measure that involves this block. This Monte Carlo procedure to compute the phase-space volume has a very poor convergence, as the phase-space mappings that are optimised for the computation of the weights are clearly inefficient for the computation of just the phase-space volume. Nevertheless, by increasing the number of generated phase-space points, we checked that the phase-space volume is reproduced with an accuracy better than one percent for each tested phase-space mapping. We first set the mass of the final-state particles to zero and obtained the results summarised in Table 3.3. We then considered the case of massive particles in the final state and obtained the results summarised in Table 3.4.

In order to validate the multichannel implementation, we also computed the total cross section of several processes by integrating the squared matrix element with our phase-

l	blocks	integrated volume
3	FB A	3.49×10^{-5}
3	FB B	3.49×10^{-5}
3*	FB C	4.13×10^{-5}
6	FB D	124 GeV^6
4	FB E	$8.17 \times 10^{-3} \text{ GeV}^2$
4	FB F	$8.17 \times 10^{-3} \text{ GeV}^2$
5	FB B + PB A	1.28 GeV^4
4	FB B + PB B	$8.17 \times 10^{-3} \text{ GeV}^2$
3	FB B + PB C	3.49×10^{-5}
3	FB B + PB D	3.49×10^{-5}
4*	FB B + PB E	$9.78 \times 10^{-3} \text{ GeV}^2$

TABLE 3.4 – Phase-space volumes $\int dq_1 dq_2 d\phi_n 1/(sq_1 q_2)$ for l particles with a mass $m = 50 \text{ GeV}$ produced in hadron-hadron collisions at $\sqrt{s} = 1 \text{ TeV}$. The number l of final-state particles is indicated in the first column. A star * indicates that the mass of one of the final state particles is set to zero, as this condition is required by one of the blocks. The second and third columns indicate the structure in blocks defining the phase-space mapping used to calculate the volume with our phase-space generator, and the numerical value we obtained. Those numbers correspond to the theoretical expected value up to three digits.

space generator. This can be achieved by setting all transfer functions to one. Here again, the convergence of the numerical integration is poor, as the phase-space parameterisation is not designed for such computation. By using a very high statistics, we reproduced the total cross sections associated with the processes listed in the first column of Table 3.5.

process	$\sigma^{\text{MW}}/\sigma^{\text{ME}}$	channels	blocks
$pp \rightarrow (W \rightarrow jj)j$	0.982(6)	3	FB A
$pp \rightarrow (W \rightarrow l\nu)$	0.9991(14)	1	FB B
$pp \rightarrow [W \rightarrow \tilde{\nu}_\tau(\tilde{\tau}^- > \tau^- \tilde{\chi})]$	1.003(5)	1	FB B ; PB C
$pp \rightarrow 2[\tilde{\mu} \rightarrow \mu \tilde{\chi}]$	1.020(5)	3	FB B,F ; PB C
$pp \rightarrow 2[t \rightarrow b(W \rightarrow l\nu_l)]$	1.000(25)	1	FB D
$pp \rightarrow t\bar{t} \rightarrow bl\nu_l b jj$	0.94(5)	6	FB B ; PB D,E
$pp \rightarrow h \rightarrow W^+ W^- \rightarrow \mu^+ \nu_m \mu^- \bar{\nu}_m$	0.99(2)	1	FB E

TABLE 3.5 – Validation of the phase-space generator by computing total cross sections. The processes under consideration are written in the first column. The second column gives the ratio of the cross section computed with MADWEIGHT over the one computed with MadEvent [77]. The third column indicates the number of channels that are used in the MADWEIGHT integration, and the last column indicates the blocks that are involved in that integration.

Chapitre 4

Standard Applications of the Matrix Element Re-weighting

“There are two possible outcomes : if the result confirms the hypothesis, then you’ve made a measurement. If the result is contrary to the hypothesis, then you’ve made a discovery.”

Enrico Fermi

In literature, we may find different ways to use the matrix element re-weighting in order to enhance the sensitivity of a measurement. An automatic and efficient method to calculate the weights is therefore suitable. In this Chapter we will provide three examples of applications of the method using MADWEIGHT and also compare the sensitivity with some other techniques. The idea is not only to discuss examples explicitly, but also to check the performance, flexibility and reliability of our implementation in “realistic” cases.

To achieve this we build “pseudo-data” samples using MADGRAPH4 [81] for the partonic events at a centre of mass energy of 14 TeV considering the CTEQ6L1 [86] data set for the parton distribution functions. Parton-level events are then passed to PYTHIA for the showering and the hadronisation with the Initial State Radiation activated (but not the underlying event). Finally, a fast simulation of the detector response was performed using PGS 4 [87] with resolutions tuned to those expected for the CMS detector.

Each transfer function should, in principle, be extracted for each process and for a specific detector. For this analysis, we use the standard approximation for the transfer function explained in Chap. 2. This corresponds to consider infinite resolution on all angles variables and for the energy of the charged leptons. In addition, and for the sake of simplicity, we consider only one parametrisation for the energy of the b-jets and the lights jets. Since we do not make use of the b-tagging techniques, we therefore consider all possible assignments between jets and final states partons involved in the matrix element calculations. In order to estimate this transfer function, we generate hundreds of thousands of jets/b-jets corresponding to the studied topology. Finally, we suppose that the transfer function can be written as a double Gaussian

$$W^E(E, E^{vis}) = \frac{1}{\sqrt{2\pi}(a_2 + a_3 a_5)} \left[e^{-\frac{(E - E^{vis} - a_1)^2}{2a_2^2}} + a_3 e^{-\frac{(E - E^{vis} - a_4)^2}{2a_5^2}} \right], \quad (4.1)$$

where all five parameters depend of the energy as follows :

$$a_i = a_{i,0} + a_{i,1}\sqrt{E} + a_{i,2}E \quad (4.2)$$

In order to fit the 15 constants $a_{i,j}$, we split the range of Energy of interest (20 – 220 GeV) in 10 bin of 20 GeV. In each of them we fit the transfer functions by a double gaussian with $a_i = a_{i,0}$ – no dependencies in energy. Then we fit the dependencies of each parameter separately. The result for the binned method is displayed in Fig. 4.1 and in Fig. 4.2 for different range in Energy. An un-binned likelihood technique [88] hardly improves the result obtained by the binned method. The value for the fitted parameter are displayed in Table 4.1. They show that bias of the first gaussian is about a couple of GeV while it's width is about 15% of the jet Energy (12% at 100 GeV). The second gaussian has a relative weight of 20% with respect to the dominant one and has more important width and bias in order to fit the distribution's tails.

4.1 The Matrix Element Method

As previously stated the Matrix Element Method (MEM) consists in combining the matrix-element weights for a given sample in a likelihood,

$$\mathcal{L}(\alpha) = \prod_{events} \mathcal{P}(p^{vis}|\alpha), \quad (4.3)$$

where $\mathcal{P}(p^{vis}|\alpha)$ is defined in Eq. (2.3).

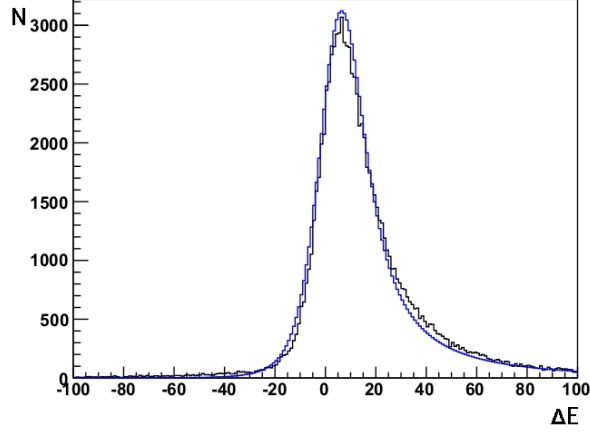


FIGURE 4.1 – Histogram of the difference of energy between the partonic jet and the reconstructed one. The blue curve correspond to the curve obtained by the fit, the black one is the curve observed on a large sample of events (more than 10^6).

The interest of such likelihood comes from the Neyman-Pearson lemma [89] which guarantees that the likelihood ratio is the most powerful discriminant variable. In other words, this is the method which has the lowest probability of mistaking the signal for a background fluctuation. But this holds only if the density of probability \mathcal{P} is correctly normalised. Nevertheless, only a subset of the collisions produced in a detector are kept for the analysis. Both the trigger and event selection imply a limited acceptance, which needs to be taken into account :

$$\bar{\mathcal{P}}(\mathbf{p}^{vis}|\alpha) = \frac{1}{C} Acc(\mathbf{p}^{vis}) \mathcal{P}(\mathbf{p}^{vis}|\alpha), \quad C = \int Acc(\mathbf{p}) \mathcal{P}(\mathbf{p}|\alpha) d\mathbf{p}, \quad (4.4)$$

where C is defined such that $\bar{\mathcal{P}}(\mathbf{p}^{vis}|\alpha)$ is correctly normalised,

$$\left[\prod_{i \in vis} \int d^3 p_i^{vis} \right] \bar{\mathcal{P}}(\mathbf{p}^{vis}|\alpha) = 1. \quad (4.5)$$

with $Acc(\mathbf{p}^{vis})$ the acceptance function. It equals one if the events pass the trigger and the event selection, and zero otherwise. Note that the acceptance term does not depend of the theoretical hypotheses.

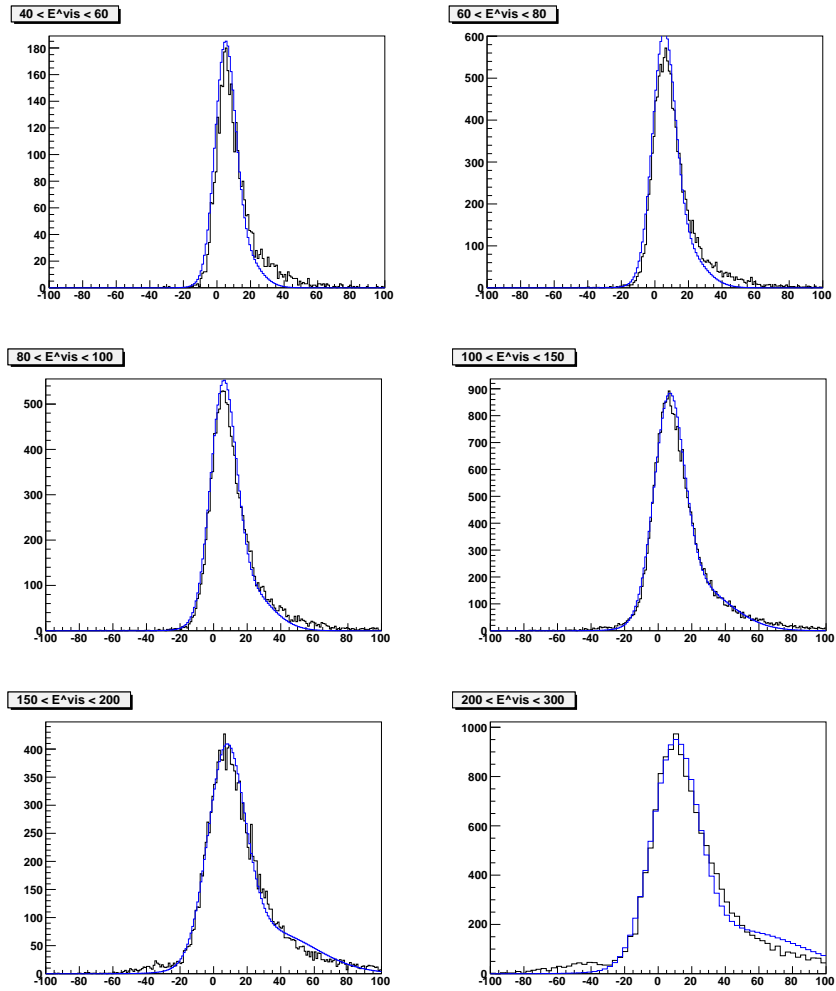


FIGURE 4.2 – Histogram of the difference of energy between the partonic jet and the reconstructed one. The blue curve correspond to the curve obtained by the fit, the black one is the curve observed on a large sample of events (more than 10^6). The last plot corresponds to a range in Energy which was not taken into account in the fit of the parameters.

parameter	type	proportional to	value
$a_{1,0}$	bias first gaussian	independent term	1.56 GeV
$a_{1,1}$		\sqrt{E}	$0.29 \text{ GeV}^{\frac{1}{2}}$
$a_{1,2}$		E	0.010
$a_{2,0}$	sigma first gaussian	independent term	0.95 GeV
$a_{2,1}$		\sqrt{E}	$0.52 \text{ GeV}^{\frac{1}{2}}$
$a_{2,2}$		E	0.019
$a_{3,0}$	ratio of gaussian	independent term	0.20
$a_{3,1}$		\sqrt{E}	$0.0 \text{ GeV}^{-\frac{1}{2}}$
$a_{3,2}$		E	0.0 GeV^{-1}
$a_{4,0}$	bias second gaussian	independent term	11.6 GeV
$a_{4,1}$		\sqrt{E}	$-2.4 \text{ GeV}^{\frac{1}{2}}$
$a_{4,2}$		E	0.32
$a_{5,0}$	sigma second gaussian	independent term	3.3 GeV
$a_{5,1}$		\sqrt{E}	$-0.086 \text{ GeV}^{\frac{1}{2}}$
$a_{5,2}$		E	0.14

TABLE 4.1 – Parameter for the transfer functions optimised for $t\bar{t}$ production.

The likelihood then reads

$$L(\alpha) = \prod_{i=1}^N \bar{\mathcal{P}}(\mathbf{p}_i^{vis}|\alpha) = \prod_{i=1}^N \frac{Acc(\mathbf{p}_i^{vis}) \mathcal{P}(\mathbf{p}_i^{vis}|\alpha)}{\int Acc(\mathbf{p}) \mathcal{P}(\mathbf{p}|\alpha) d\mathbf{p}}, \quad (4.6)$$

$$-\log(L) = -\sum_{i=1}^N \log(\bar{\mathcal{P}}(\mathbf{p}_i^{vis}|\alpha)), \quad (4.7)$$

$$= -\sum_{i=1}^N \log(\mathcal{P}(\mathbf{p}_i^{vis}|\alpha)) + N \log \left(\int Acc(\mathbf{p}) \mathcal{P}(\mathbf{p}|\alpha) d\mathbf{p} \right) - \sum_{i=1}^N \log(Acc(\mathbf{p}^{vis})). \quad (4.8)$$

In practice, the last term of Eq. (4.8) can be dropped since it does not depend on α and therefore has no discriminant power. The second one ($N \log [\int Acc(\mathbf{p}^{vis}) \mathcal{P}(\mathbf{p}^{vis}|\alpha) d^3\mathbf{p}^{vis}]$) is called the *acceptance term* and compensates the bias introduced by the event selection.

The numerical evaluation of the acceptance term can be performed by generating a Monte-Carlo sample of events for each theoretical hypotheses. Indeed it is easy to show that $\int Acc(\mathbf{p}^{vis}) \mathcal{P}(\mathbf{p}^{vis}|\alpha) d^3\mathbf{p}^{vis} = \frac{N_{acc}}{N_{gen}}$ where N_{gen} is the number of events

generated by the Monte-Carlo generation and N_{acc} is the number of those events which pass the selection [88].

In order to see the potential importance of the acceptance term, let us go back to the example of Chap. 2 where we have extracted the W mass from a sample of partonic events in an ideal detector. But this time, we compute the likelihood for a sample of events with¹ $p_T > 40$ GeV. The result likelihood with and without acceptance term are displayed in Fig. 4.3. Neglecting the acceptance term introduces a strong bias leading to $m_W = 82.3 \pm 0.5$ GeV. If, however, we include the correction term we obtain $m_W = 79.4 \pm 0.7$ which is compatible with the input value (80 GeV).

4.2 Top-quark mass measurement

The top-quark mass measurement by means of the matrix element method was published for the first time by the $D\emptyset$ collaboration using the single-leptonic final state arising from top-quark pair production [69]. The method has been later extended to include a simultaneous determination of the Jet-Energy-Scale uncertainty [90]. The accuracy of the experimental determination of m_t has been further improved by the contribution of other studies based on the matrix element method [71, 72, 73]. In these analyses, a dedicated phase-space integration was performed to compute the matrix-element weight (see for one example [88]).

As a first example of application of our automatic re-weighting algorithm, we illustrate the performance of the method for the determination of the top-quark mass at the LHC, by using a small statistics of $t\bar{t}$ events in the single lepton final state :

$$pp \rightarrow [\bar{t} \rightarrow \bar{b}(W^- \rightarrow \mu^- \bar{\nu}_\mu)][t \rightarrow b(W^+ \rightarrow jj)]. \quad (4.9)$$

For the sake of simplicity, we assume that there is no background and use 20 signal events after selection. Pseudo-data have been simulated with an input top-quark mass at 170 GeV. The selection requires one muon with a reconstructed transverse momentum above 10 GeV and exactly four isolated jets with a reconstructed transverse momentum above 20 GeV.

The determination of the top-quark mass from our sample of pseudo-data is obtained by the minimisation of $-\log(L)$ with respect of m_t where the likelihood L is defined in Eq. (4.8). We have checked that for this process and for such luminosity, the bias introduced by the acceptance cuts is very small and can then be freely ignored in this example.

1. The value has been chosen such that the selection cuts are quite strong and strongly increasing between the different test masses.

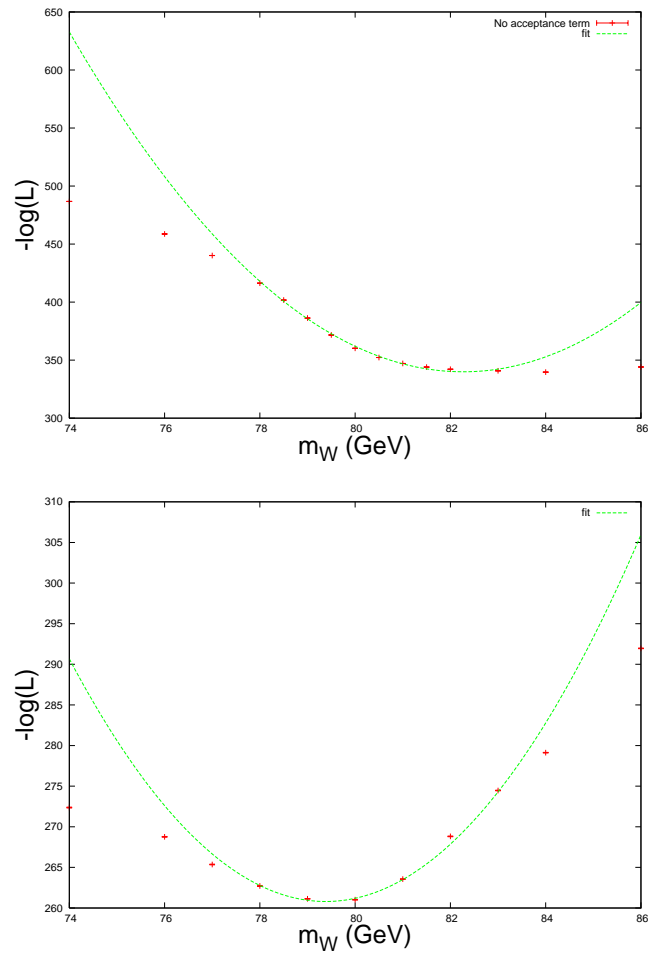


FIGURE 4.3 – Logarithmic likelihood values for a sample of 250 events generated with $m_{W, \text{input}} = 80$ GeV and having a p_T larger than 40 GeV. The top plot doesn't take into account the associate acceptance term, leading to a bias in the measurement : $m_W = 82.3 \pm 0.5$. The bottom plot includes the acceptance term correction which compensates the bias due to the selection cut. The measured value $m_W = 79.4 \pm 0.7$ is then compatible with the input mass.

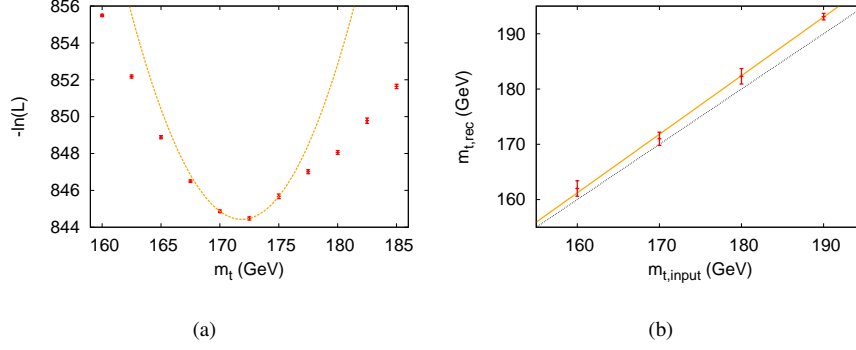


FIGURE 4.4 – (a) Logarithmic likelihood values for a sample of 20 events generated with $m_{t, \text{input}} = 170$ GeV. The dashed line is a parabolic fit to the points close to the minimum. The statistical error is estimated by the half width of the distribution at $\log(L/L_{\text{max}}) = 0.5$ and is extracted from the fit. (b) Calibration of the matrix element mass fitting procedure. The error-bars correspond to the the value of mass of the top quark and the associated statistical error reconstructed from $t\bar{t}$ samples generated with different input values of m_t . The dashed line is a linear fit to the error-bars.

The values of $-\log(L)$ for different assumptions of m_t are displayed in Fig. 4.4(a). A clear minimum is observed close to the input mass value. A parabolic fit gives the value $m_t = 171.9 \pm 2.0_{\text{stat}}$ GeV. Using ten independent samples generated under the same conditions, we extracted the expected m_t value and the expected statistical error for such a measurement : $m_t = 173.5 \pm 3.7_{\text{stat}}$ GeV. By generating $t\bar{t}$ samples with top quark masses of 160, 170, 180 and 190 GeV with the same selection procedure and the same fitting procedure, and with a statistics of 100 events per sample, we identified a small significant shift between the input and the reconstructed mass by repeating the analysis for other input masses, as can be seen from the calibration curve displayed in Fig. 4.4(b). We observed a shift rising with the energy which is at about 1.8 GeV for an input top-quark mass of 170 GeV. As we will discuss in Chap. 5, the presence of Initial State Radiation not correctly dealt with by the MEM is the origin of such bias.

4.3 Smuon production

Over the past fifteen years, numerous developments of techniques for mass reconstruction of new particles that might be produced at the LHC have been realised. According to most scenarios, the hypothetical new physics states are not expected to be directly observed experimentally, *i.e.*, they appear as intermediate states in specific

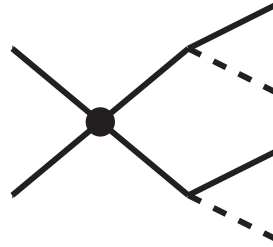


FIGURE 4.5 – Generic decay chain corresponding to the production of two resonances followed by their decay into weakly-interacting and Standard Model particles. The weakly-interacting particles are represented by the dashed lines.

decay chains or they escape from the detector without interacting with it. Their mass can hence only be reconstructed indirectly, by making a number of assumptions on the decay chain at work. The number of assumptions in turn is directly correlated to the amount of information that can be extracted from the decay chain. However, due to the lack of constraints on physics beyond the Standard Model, the proposed techniques have to be general enough, at least if they are aimed at reconstructing the mass of new hypothetical particles in the early stages of investigation. Furthermore, the limited knowledge of the detector has to be taken into account. It is in this context that a number of mass measurement techniques based on kinematic methods have been proposed in the literature. They can be classified according to the type of decay chains that they address and according to the assumptions on which they rely [19].

Despite the plurality of kinematic variables that have been proposed, mass determination remains very challenging for specific decay chains. One well-known example of a difficult topology is the production of two resonances followed by their decay into a weakly-interacting particle and a Standard Model particle, shown in Fig. 4.5. In this case, the kinematic methods that have been proposed to reconstruct simultaneously the mass of the two new particles require a very high luminosity. Whether their sensitivity is sufficient under real experimental conditions still remains to be determined. A complementary way to address the same problem is to ask what would be the maximum sensitivity achievable, given a very detailed set of hypotheses to be tested that not only include masses but also the spin and couplings information, *i.e.*, taking into account the full theoretical model prediction.

The problem can be investigated with the matrix element method that usually makes use of the strongest assumptions on the analysed events [89]. One way to dramatically increase the theoretical information is to assume that the masses of the new physics states are the only unknown properties of the decay chain. We therefore consider a

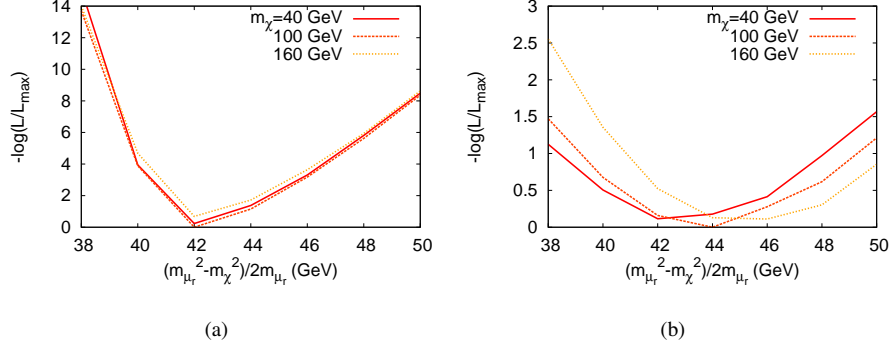


FIGURE 4.6 – Logarithmic likelihood as a function of the hypothesis values for $[(m_{\tilde{\mu}_r}^2 - m_{\tilde{\chi}_1}^2)/2m_{\tilde{\mu}_r}, m_{\tilde{\chi}_1}]$ built upon (a) the matrix element weights, (b) the transverse momentum of the μ^+ and the invariant mass of the muons.

specific decay chain corresponding to the topology in Fig. 4.5 : the production of a pair of smuons followed by their decay into a muon and a neutralino

$$pp \rightarrow (\tilde{\mu}_r^+ \rightarrow \mu^+ \tilde{\chi}_1)(\tilde{\mu}_r^- \rightarrow \mu^- \tilde{\chi}_1). \quad (4.10)$$

We suppose that we have isolated a pure sample of events that correspond to the decay chain in Eq. (4.10). Furthermore, we assume a perfect reconstruction of the kinematics of the two muons in each event. With these assumptions, the significance that can be achieved with the matrix element method provides us with an upper bound on the significance that can be delivered by any realistic analyses at a given luminosity.

We have considered the following input hypothesis for the masses of the sparticles :

$$m_{\tilde{\mu}_r, \text{input}} = 150 \text{ GeV}, \quad m_{\tilde{\chi}_1, \text{input}} = 100 \text{ GeV}. \quad (4.11)$$

Under this hypothesis, we have generated events corresponding to the decay chain in Eq. (4.10). We have built a sample of fifty events with exactly one μ^+ and one μ^- with a transverse momentum larger than 20 GeV, and no other particles except maybe some jets with a p_T less than 20 GeV. These events are regarded as a pseudo-experimental sample in the following.

The sensitivity that can be achieved with the matrix element method has been analysed by computing the weights $\mathcal{P}(\mathbf{p}_i^{\text{vis}} | m_{\tilde{\mu}_r}, m_{\tilde{\chi}_1})$ for each event $\mathbf{p}_i^{\text{vis}}$ in the pseudo-experimental sample and for each tested hypothesis for $(m_{\tilde{\mu}_r}, m_{\tilde{\chi}_1})$, and by analysing the likelihood built upon these weights. This time the acceptance term is not negligible and is then taken into account in the analysis.

It is advantageous to express the likelihood in terms of the variable $(m_{\tilde{\mu}_r}^2 - m_{\tilde{\chi}_1}^2)/2m_{\tilde{\mu}_r}$, which corresponds to the momentum of each final state particle in the rest frame of the smuon from which it originates. The complementary variable can be chosen to be $m_{\tilde{\chi}_1}$. The likelihood for different theoretical hypotheses is shown in Fig. 4.6(a). The optimal value for the variable $(m_{\tilde{\mu}_r}^2 - m_{\tilde{\chi}_1}^2)/2m_{\tilde{\mu}_r}$ is 42 GeV, which corresponds to the input value. In the MEM, we also observe a very mild sensitivity with respect to the variation of the complementary particle, but this may be too sensitive to systematical error in order to be observable in a real experiment.

One way to highlight the increase of sensitivity obtained by using the complete theoretical and experimental information is to compare the profile of the likelihood built upon the matrix element weights (shown in Fig. 4.6(a)) with the likelihood profile that is obtained by keeping only the information contained in the transverse momentum $p_{T\mu}$ of the μ^+ and the invariant mass $M_{\mu\mu}$ of the muons. In order to simplify the computation of this second likelihood profile we neglect the correlations between the two variables $p_{T\mu}$ and $M_{\mu\mu}$. Thus the weight attached to each event is reduced to

$$P(x_i|m_{\tilde{\mu}_r}, m_{\tilde{\chi}_1}) \rightarrow \frac{1}{\sigma} \frac{d\sigma}{dp_{T\mu}}(P_{T\mu}|m_{\tilde{\mu}_r}, m_{\tilde{\chi}_1}) \times \frac{1}{\sigma} \frac{d\sigma}{M_{\mu\mu}}(M_{\mu\mu}|m_{\tilde{\mu}_r}, m_{\tilde{\chi}_1}). \quad (4.12)$$

The resulting likelihood profile is displayed in Fig. 4.6(b). The comparison with Fig. 4.6(a) shows that the sensitivity to the theoretical hypothesis $(m_{\tilde{\mu}_r}, m_{\tilde{\chi}_1})$ is dramatically reduced when only the information contained in the kinematic variables $p_{T\mu}$ and $M_{\mu\mu}$ is used.

4.4 Spin sensitivity : Charged Higgs

As a third illustration we address the challenge of determining the spin of new particles. A simple example is the production of a light charged Higgs boson with a mass close to the W^\pm boson mass. The information on the spin of a resonance is passed through the angular distribution of its decay products. If the momentum of each final-state particle produced in the decay chain is measured, the angular distributions can be reconstructed and the spin of the resonance identified. In fact in many cases, such as the one we have chosen, the final state is characterised by missing transverse energy from undetected particles and the angular distributions of the decay products cannot be fully determined. The interesting question becomes therefore whether the available information from the final state is sufficient to discriminate between different spin assignments in the decay chain. The matrix element re-weighting appears to be particularly relevant in this case, since the event weight will encompass the whole available event kinematics including the spin correlation effects that survive after the experimental reconstruction of the events.

The presence of a charged Higgs in top decays was searched both at DØ et CDF by putting limits on the possible branching ratio of the top in a charged Higgs for different masses of the charged Higgs and different values for $\tan\beta$ [91,92,93]. In those papers two main techniques were used, one based on the matrix element and a second on the p_T distributions.

In the following example, we assume that the production of the signal and its irreducible background proceeds exclusively via the production of top quark pair that subsequently decay into $H^\pm b$ or into $W^\pm b$, with $m_{H^\pm} \simeq m_{W^\pm}$, followed by a leptonic decay of both bosons. The signal process is

$$pp \rightarrow [t \rightarrow b(H^+ \rightarrow \tau^+ \nu_\tau)][\bar{t} \rightarrow \bar{b}(W^- \rightarrow \mu^- \bar{\nu}_\mu)], \quad (4.13)$$

and the corresponding irreducible background results from the production of a pair of W bosons,

$$pp \rightarrow [t \rightarrow b(W^+ \rightarrow \tau^+ \nu_\tau)][\bar{t} \rightarrow \bar{b}(W^- \rightarrow \mu^- \bar{\nu}_\mu)]. \quad (4.14)$$

At the reconstruction level, we required the presence of exactly two jets with a p_T larger than 20 GeV, one τ^+ –assumed to be reconstructed as precisely as the other charged leptons– and one μ^- . The cuts on these leptons are $|\eta| < 2.4$ and $p_T > 5$ GeV. We reject the events containing photons or electrons with $p_T > 5$ GeV and $|\eta| < 2.4$, while, as for previous example, we neglect all radiation with a p_T less than 20 GeV. The transfer functions associated with the other particles have the same parameterisation as described in Section 1.3. We arbitrarily choose a final relative normalisation of signal and background events, working with a sample of 240 signal events and 760 background events.

Before proceeding further, we stress that while providing an interesting case study, this example cannot be regarded as very realistic. First, the relative cross sections and reconstruction efficiencies for the signal and the background have been chosen arbitrarily. Second, such a light charged Higgs is not favoured by present constraints, which point to much higher masses. Finally, the tau lepton reconstruction is idealised as it is considered here on the same footing as a muon. A more realistic approach would consist in taking into account the energy loss from the tau decay with a dedicated transfer function for the energy of the tau. Nonetheless, as shown below, this example illustrates quite well the power of the matrix element re-weighting (used here in a Template Method).

Let us define $P_S(\mathbf{p}^{vis})$, $P_B(\mathbf{p}^{vis})$ as the weights evaluated for the event final state \mathbf{p}^{vis} under the signal and the background hypotheses, respectively. These weights can be calculated from the signal and background full matrix element as defined in Eq. (2.3). Alternatively, as in some experimental analyses [94], they can be associated with a

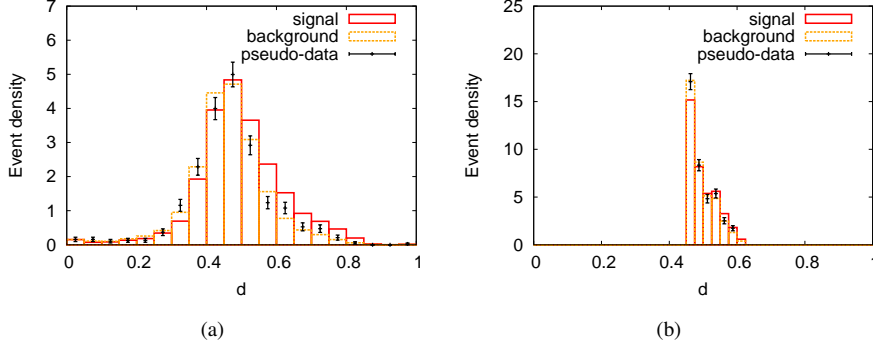


FIGURE 4.7 – Expected normalised distribution of events with respect to the discriminant d built upon (a) the matrix element weight and (b) the p_T of the tau for a pure signal sample (solid histogram) and for a pure background sample (dashed histogram). The error-bars are the distributions associated with the pseudo-experimental sample, assuming that the statistical error on the number N of events in a bin is given by \sqrt{N} .

normalised differential cross section with respect to a single observable, such as the τ^+ transverse momentum

$$P_{S,B}(\mathbf{p}^{vis}) \rightarrow \frac{1}{\sigma_{S,B}} \frac{d\sigma_{S,B}}{dp_T} [p_T(\tau^+)], \quad (4.15)$$

which also captures the spin effects. The advantage of the weights defined in Eq. (4.15) lies in their simplicity. Their evaluation only requires to use a standard phase-space generator that is optimised for the computation of cross sections. Such an observable, for example, is very commonly used in the determination of the polarisation of the W bosons in top events and provides us with a useful benchmark to study the increased sensitivity that the matrix element method might provide.

These weights can then be combined to build an event-by-event discriminating variable

$$d(\mathbf{p}^{vis}) = \frac{\mathcal{P}_S(\mathbf{p}^{vis})}{\mathcal{P}_S(\mathbf{p}^{vis}) + \mathcal{P}_B(\mathbf{p}^{vis})}. \quad (4.16)$$

The normalised-to-one distributions of events as a function of the discriminant variable d are shown in Fig. 4.7 for the two cases. The solid (resp. dashed) histogram is the distribution expected for a pure sample of signal (resp. background) events. These distributions have been generated from large samples, in order to allow us to neglect the statistical fluctuations. Spin correlation effects are expected to give rise to different values for the weights under the two spin hypotheses. Nevertheless, for most

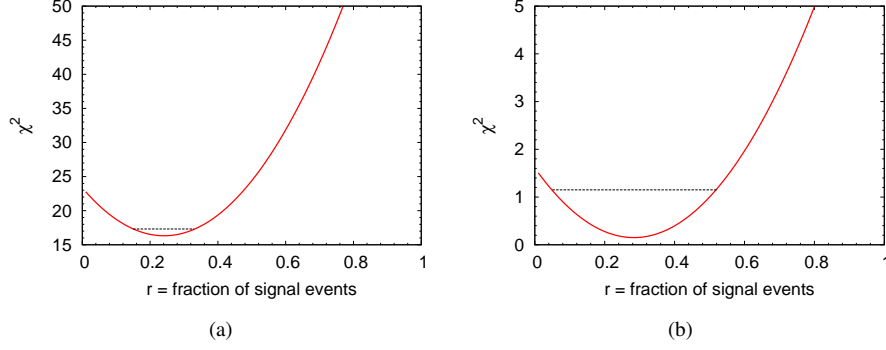


FIGURE 4.8 – χ^2 values associated with the fit of the pseudo-experimental data to the theoretical prediction parameterised by the fraction r of signal events for the weights calculated from (a) the matrix element, (b) the p_T of the tau. Each dashed line represents the one-standard-deviation interval defined by the condition $\chi^2(r) < \chi_{\min}^2 + 1$.

of the events, this disparity is expected to be small, resulting in a discriminant close to $d \simeq 0.5$. Note that in our example, signal and background events are characterised by the same topology with intermediate particles of the same mass. Only the spin of the intermediate W^\pm or H^\pm resonances differ between the two decay chains. The distributions clearly show that the discriminant power is substantially reduced when only the information on the transverse momentum of the τ^+ is retained.

Yet, for some events the discriminant is significantly different from 0.5, corresponding to configurations clearly favoured by one of the two hypotheses. Such events influence the shape of the distributions and allow us to distinguish them. One can take advantage of this difference to find out the fraction of signal events in the pseudo-experimental sample. The normalised-to-one distribution associated with the pseudo-experimental sample as a function of the discriminant variable d is also displayed in Fig. 4.7. The fraction of signal events in the pseudo-experimental sample can be estimated by fitting the points $[\mathcal{P}_{data}(d)]$ with the curve

$$\mathcal{P}_{data}(d) = r\mathcal{P}_S(d) + (1 - r)\mathcal{P}_B(d), \quad (4.17)$$

and minimising the χ^2 with respect to the parameter r that represents the fraction of signal events in the pseudo-experimental sample. The χ^2 values of the corresponding fit as a function of the fraction of signal events are shown in Fig. 4.8. The best fits for each discriminant are obtained for $r = 24 \pm 9\%$ and $r = 28 \pm 23\%$, respectively. Both results are compatible with the true fraction of signal events, but the discriminant using matrix elements increases the accuracy by a factor of about 2.5.

4.5 Differential Matrix Element Method

Even if the re-weighting technique can be used in different ways, it is currently mainly used for precision physics (determination of mass, couplings, cross sections) and as an input to discriminate signal from backgrounds (as an entry of a neural network for example). We can also use the matrix element re-weighting to estimate differential cross-sections.

This original technique is strongly inspired by the techniques consisting in the evaluation of the differential cross section with the Kinematical-Fit method [95, 96] and is a direct extension to the Matrix Template method [97]. We called our new method the *Differential Matrix Element Method* (DMEM).

Building differential cross sections with respect to arbitrary quantities might imply the knowledge of the full kinematics of the events (i.e. estimate quantities like the momentum of a neutrino). This knowledge requires to include some theoretical input in order to discriminate the different partonic configuration. We propose to use the full power of the matrix element by using the marginal events distributions of

$$\frac{1}{\mathcal{P}(\mathbf{p}^{vis})} \frac{\partial \mathcal{P}(\mathbf{p}^{vis})}{\partial Z}. \quad (4.18)$$

as a discriminator between the different kinematical configuration. Since such curves are normalised to unity, summing over them provides an estimation of the shape of the differential cross section.

In order to observe the feasibility of the techniques, we have generated with MADGRAPH [81] top quark pair events decaying in the fully leptonic channel

$$pp \rightarrow t\bar{t} \rightarrow b\bar{b}l^+l^-\nu_l\bar{\nu}_l, \quad (4.19)$$

at a centre-of-mass energy of 14 TeV and with CTEQ6L1 [86] as the set of PDF.

As a first check that our technique provides a sensitive estimator for the differential cross sections, we used a sample of 5000 parton events to estimate the differential cross section for the top-quark pair invariant mass and for the top-diffusion angle in the $t\bar{t}$ rest frame.² The results are displayed in Fig. 4.9. The DMEM differential curve reproduces well the theoretical curves without any significant bias.

We also performed a second, more realistic, comparison at detector level. In order to simulate our sample, we take the parton level sample –generated by MADGRAPH–

² Since we are running at parton level, the transfer functions used for those computations are delta functions.

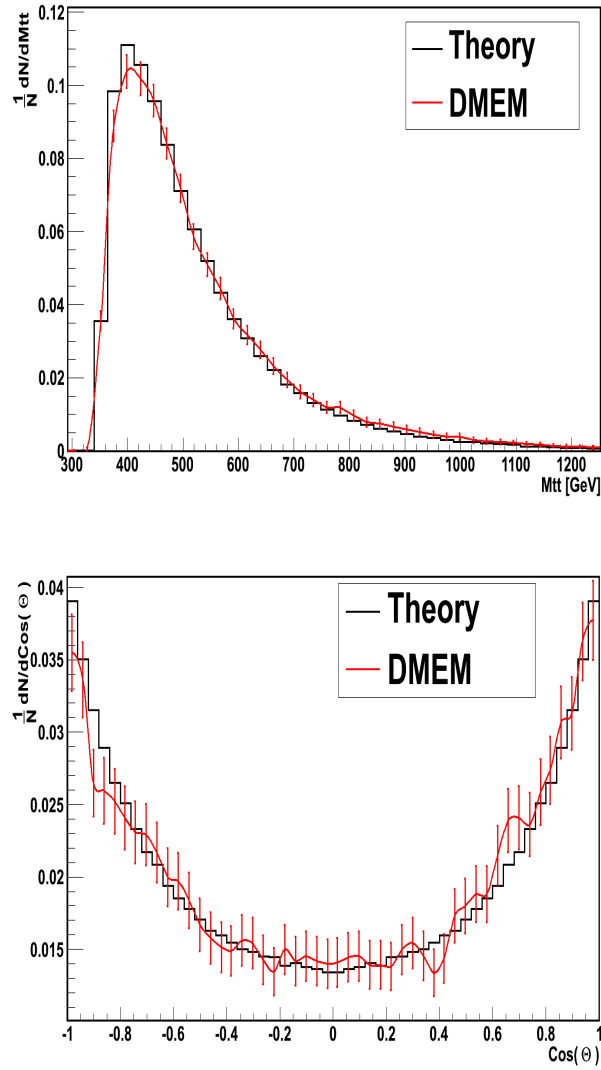


FIGURE 4.9 – Normalised differential cross section of top quark pair production in fully leptonic decay for the $t\bar{t}$ invariant mass (top) and for the top diffusion angle measured in the $t\bar{t}$ rest frame (bottom). The two estimators of the differential cross section are based on a sample of 5000 Standard Model partonic events.

and passed it through PYTHIA – with ISR activated– and then pass the resulting events in a fast simulation of the CMS detector response done with PGS.³ In order to have a quite clean sample, we have applied cuts inspired by the selection performed at CMS [3]. We select events with exactly two jets with transverse momentum larger than 30 GeV, and request the presence of two opposite sign leptons with $p_T > 20$ GeV. Additionally, we ask a transverse missing energy larger than 30 GeV.

Fig. 4.10 displays the same differential cross section as displayed in the parton-level case. For the differential cross section corresponding to the invariant mass, we note a small bias. One possible explanation is that the theoretical curves does not take into account the influence of ISR while this variable is quite sensitive to those effects. The limited resolution of the detector as well as the parameterization of transfer-functions could also induce some bias. On the Opposite, the diffusion angles – less sensitive to those effects– didn't present any bias.

With or without bias, the important point is to check whether a given theoretical prediction (i.e. the Standard Model) reproduces the data or not. To illustrate this point, we will evaluate the differential cross-sections with a sample containing $t\bar{t}$ events induced by a resonant heavy vectorial state.

$$pp \rightarrow Z' \rightarrow t\bar{t} \rightarrow b\bar{b}l^+l^-\nu_l\bar{\nu}_l. \quad (4.20)$$

This is a simple example of typical new physics scenarios for $t\bar{t}$ estimation of the cross section [97, 98].

In order to generate samples with different contamination of Z' events, we generate a pure sample of Z' events with $m_{Z'} = 600$ GeV. These events are generated in the same way and with the same cuts as those described for the SM sample. After cut selection, this sample is mixed with different Standard model events with a fixed fraction of Z' events – we will present results for 5, 8 and 10% of Z' events in the final samples.

It should be stressed that the matrix element used for the computation of the differential cross section is always the Standard Model one. Our method does not have any a priori information on the type of new physics which can be observed in the detector.

Fig. 4.11 shows the result for the differential cross section relative to the invariant mass of the $t\bar{t}$ pair.⁴ A clear tendencies emerge : The more we have new physics events in the sample the more the curve diverges from the SM expected one. The smoothness

3. The transfer functions used in this case are of the double Gaussian type like in Eq. (4.1).

4. Equivalent evaluations of differential cross sections have been performed for different variables with in all cases less sensitivity in comparison to the $t\bar{t}$ invariant mass.

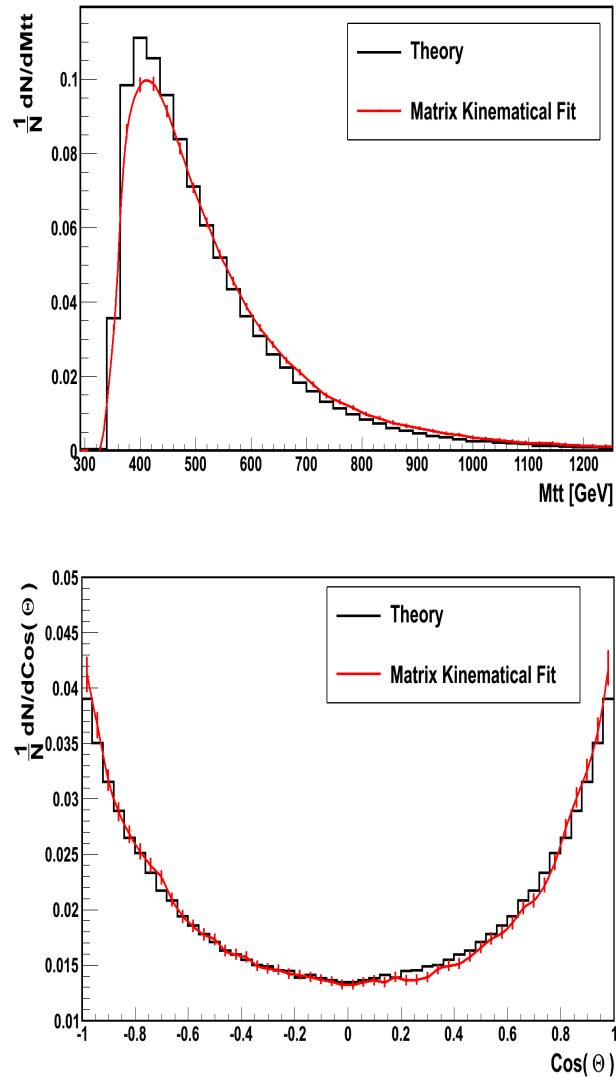


FIGURE 4.10 – Normalised differential cross section of top quark pair production in fully leptonic decay for the $t\bar{t}$ invariant mass (top) and for the top diffusion angle measured in the $t\bar{t}$ rest frame (bottom). The two estimators of the differential cross section are based on a sample of 10000 Standard Model partonic events. The theoretical curve is the expected one at tree-level –no ISR and UE are taken into account.

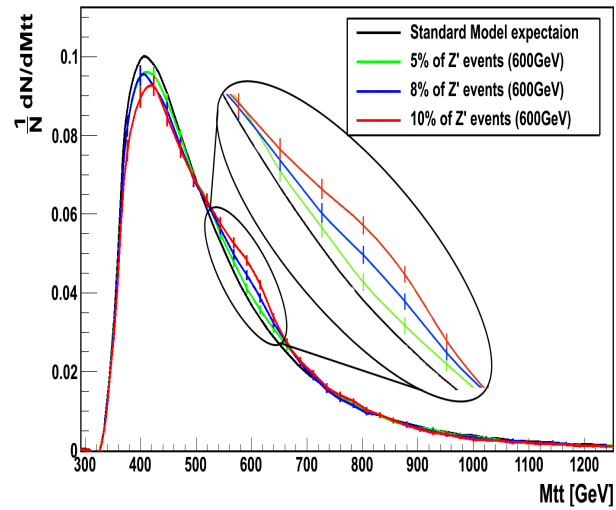


FIGURE 4.11 – Differential cross section for the top quark pair invariant mass for 3 different samples of 5000 events containing different ratios of SM and Z' events. The graph presents the estimation of the differential cross section for the DMEM method. The Standard Model expected curves have been estimated on a sample of 100 thousand Standard Model events.

of the deviation indicates that the DMEM is a sensitive way to discriminate the SM hypothesis.

In order to be able to claim deviation from the Standard Model, we can associate to each curve a chi-squared value measuring the agreement of the curve with the expected one. The details on the chi-square definition are discussed in App. B. In order to have an expression which measures the deviation from the Standard Model, we use the confidence level :

$$CL(\chi_0^2) \equiv P(\chi^2 \geq \chi_0^2). \quad (4.21)$$

The expected value for a pure Standard Model event is 0.50 ± 0.33 . A value close to zero indicates that the samples is not (or unlikely) a pure SM sample, while a value close to one indicates that the two curves are in too perfect agreement.

The expected confidence level value and the one sigma range were evaluated for the different samples containing the Z' events. The standard model can be excluded at 90% of confidence level for already 5000 selected events containing 5% of Z' . Of course, if the ratio of non Standard Model events is bigger the exclusion is reached for lower luminosity.

The way the sensitivity of the DMEM method compare to other techniques as well as the importance of the systematic uncertainties related to method are still to be evaluated. Also the sensitivity to New Physics should be evaluated on a larger class of examples before we can assess the importance of this new method which looks promising anyway.

Chapitre 5

QCD Radiation In the Matrix Element Method

“If someone says that he can think or talk about quantum physics without becoming dizzy, that shows only that he has not understood anything whatever about it.”

Murray Gell-Mann

The MEM was intensively used at the TEVATRON. However, only events for which the number of jets exactly matches the number of coloured partons in the hard matrix element have been included. For instance, only two-jet events have been considered for the analysis of the di-leptonic top-quark pairs. At the TEVATRON, this approach works, since the top quarks are relatively heavy compared to the beam energy and thus the phase space for extra radiation is highly suppressed.

However, at the LHC, radiation of hard jets is expected to be abundant, not only for top pair production but also for new physics processes involving coloured particles with masses of a few 100 GeV [99, 100]. With a centre-of-mass energy of 14 TeV, the number of top pair events is reduced by more than 40% if one requires no extra jets with $p_T > 40$ GeV¹. This estimate is based on events generated with PYTHIA 6.4 [101] and passed through the fast detector simulation PGS 4 [87]. As will be shown later, even the presence of additional jets with $p_T < 40$ GeV can lead to problems with

1. About 27% of events have one additional jet with $p_T > 40$ GeV, while about 15% have two or more extra jets.

fitting the signal events, so that a tighter cut will be necessary to eliminate the influence of jet radiation, hence leading to a large loss of signal statistics.

Alternatively, one could try to take into account events with extra jets by including matrix elements with more partons in the final state. Referring again to the example of di-leptonic top pairs, this would amount to matrix elements corresponding to the processes $pp \rightarrow b\bar{b}l^+l^-\nu\bar{\nu} + n_q q + n_{\bar{q}} \bar{q} + n_g g$, which have n_q quarks, $n_{\bar{q}}$ antiquarks and n_g gluons in the final state beside the usual top decay products. While this approach should allow to correctly include all events, it substantially increases the computation time, due to the complexity of the multi-particle matrix elements, the more complicated structure of the phase space, and the combinatorial related to summing over quark flavours and gluons in the extra jets. Even if one restricts oneself to considering only up to two extra partons in the final state, the computing time of the likelihood fit is increased by more than an order of magnitude.

For all processes of interest –SM and common BSM scenario– most of those additional extra-jets originates from Initial State Radiation (ISR) [99]. Additional radiation have mainly two origin : Underline Event (UE) and Final State Radiation (FSR). While the second one is supposed to be taken into account by the transfer functions,² the first producing low energy jets is an un-reducible source of systematic bias in any attempt to deal correctly with ISR.

In the following two Sections a method will be described which accounts for the main effect of ISR by performing a kinematical correction event by event, using matrix elements for the hard process only, without additional partons in the final state. For concreteness, the numerical analyses has been carried out for two representative processes. Top-quark pair production with di-leptonic decay,

$$pp \rightarrow t\bar{t} \rightarrow b\bar{b}l^+l^-\nu\bar{\nu}, \quad (5.1)$$

is a typical case of pair production of heavy particles with relatively long decay chains. As a second example we will consider Higgs production via gluon fusion,

$$gg \rightarrow h \rightarrow W^+W^- \rightarrow l^+l^-\nu\bar{\nu}, \quad (5.2)$$

with the characteristic feature of a s -channel resonance.

Numerical results shown in the following Sections corresponds to a centre-of-mass energy of $\sqrt{s} = 14$ TeV, but the essential aspects do not change for lower values of \sqrt{s} . The results of these Section have been cross-checked with a specialised private code written by A. Freytas using matrix elements based on COMPHEP 4.4 [102].

². Quite often the assignment between a jet and a parton needed during the transfer functions determination is based on alignment between the two objects. Such rules are broken for hard radiations which are then not taken into account correctly, leading to a systematical bias.

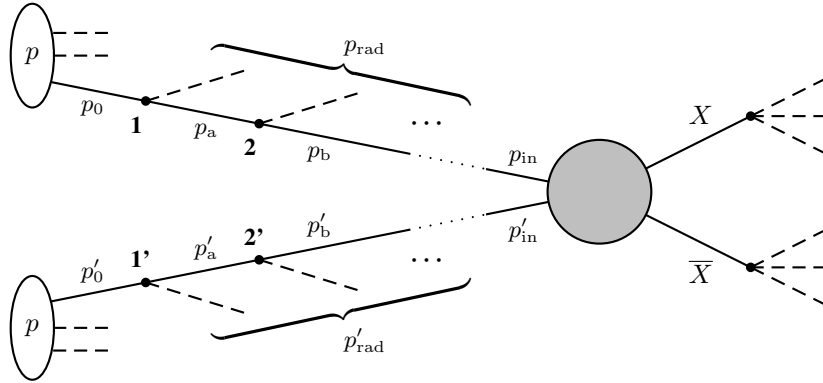


FIGURE 5.1 – Schematic depiction of the event topology for pair production of heavy particles X , together with initial state radiation.

5.1 Initial State Radiation at partonic level

In order to study the effects of ISR on the method, we first restrict ourselves to an analysis at the parton level. Simulated “data” events have been generated with PYTHIA 6.4 [101], and the momenta of the final state particles as well as of the ISR have been extracted from the event record for each event. No cuts on the parton momenta have been implemented and therefore the acceptance term is simply 1. For simplicity and clarity of the discussion, we do not include backgrounds in the analysis.

The proposed technique is based on the observation that the most significant effect of ISR is on the kinematics of the events, since without proper inclusion of ISR the momentum balance would be violated. The proper kinematics of the hard scattering matrix element can be restored by simply boosting the momenta of the particles corresponding to the hard process by the momenta of the ISR. Since the longitudinal incoming momenta are integrated in the computation of the likelihood, it is sufficient to perform the boost for the transverse coordinates only. In practice, instead of boosting the measured final state momenta, we perform the boost on the incoming partons of the matrix element, which is equivalent since the squared matrix element is a Lorentz scalar. As we are only performing a kinematical boost, the ISR momenta for each incoming leg are summed up, and the sequence of individual branching does not play any role.

This boost correction is the simplest possible treatment of ISR, which only maintains the proper momentum balance, while the effects of the particular QCD vertices and internal propagators (labeled by numbers and $p_{a,b,\dots}$ in Fig. 5.1, respectively) are not

taken into account. It has the advantage of not increasing significantly the computing time of the MEM likelihood fit compared to the situation without ISR. On the contrary, the convergence of the integral is usually faster since the kinematics of the events are often in a better agreement with the mapping of the peaks.

However, one can try to do better by including Sudakov re-weighting for the ISR. The Sudakov factor corresponds to the probability for no branching to occur between two scales $p_{T,E1}^2 < p_{T,E0}^2$. For ISR it is appropriate to formulate the Sudakov factor in terms of backwards evolution from the hard process to the incident proton. In this case it is given by [103, 104]

$$\Delta_{\text{ISR}}(p_{T,E0}^2, p_{T,E1}^2) = \exp\left(-\int_{p_{T,E1}^2}^{p_{T,E0}^2} \frac{d(p_{T,E}^2)}{p_{T,E}^2} \frac{\alpha_s(p_{T,E}^2)}{2\pi} \sum_{j \in \{j \rightarrow i+X\}} \int_{z_{\min}(p_{T,E}^2)}^{z_{\max}(p_{T,E}^2)} dz \frac{P_{j \rightarrow i}(z)}{z} \frac{f_j(x_i/z, p_{T,E}^2)}{f_i(x_i, p_{T,E}^2)}\right), \quad (5.3)$$

where the sum runs over all possible assignments of partons i, j (quarks or gluon) in the branching $j \rightarrow i + X$. Here f_j are the parton distribution functions and $P_{j \rightarrow i}$ are the splitting functions, which for massless quarks read

$$P_{gq}(z) = P_{qg} = \frac{4(1+z^2)}{3(1-z)}, \quad (5.4)$$

$$P_{qq}(z) = \frac{1}{2} [z^2 + (1-z)^2], \quad (5.5)$$

$$P_{gg}(z) = 6 \frac{[1-z(1-z)]^2}{z(1-z)}. \quad (5.6)$$

Furthermore, z is the ratio between the squared pre-branching invariant mass of the parton-parton interaction and the squared post-branching invariant mass.

On the other hand, to account for the proper weight of the ISR, one needs the probability of having a splitting $j \rightarrow i + X$ at some kinematic configuration $(p_{T,E}^2, z)$, which is given by taking the derivative of the Sudakov factor :

$$\mathcal{P}_j(p_{T,E}^2, z) = -\frac{d^2}{d(p_{T,E}^2)dz} \Delta_{\text{ISR}}(p_{T,E0}^2, p_{T,E}^2), \quad (5.7)$$

$$= \frac{\alpha_s(p_{T,E}^2)}{2\pi p_{T,E}^2} \frac{P_{j \rightarrow i}(z)}{z} \frac{f_j(x_i/z, p_{T,E}^2)}{f_i(x_i, p_{T,E}^2)} \Delta_{\text{ISR}}(p_{T,E0}^2, p_{T,E}^2). \quad (5.8)$$

The branching probability for any kind of parton, which is the quantity needed in practice, is then given by $\sum_j \mathcal{P}_j(p_{T,E}^2, z)$.

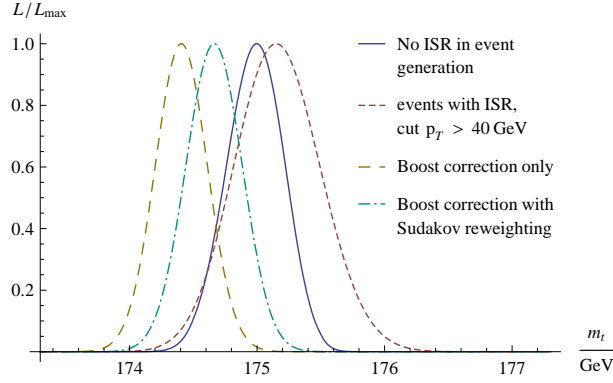


FIGURE 5.2 – Reconstruction of the top quark mass from a matrix element likelihood fit to 1000 parton-level di-lepton $t\bar{t}$ events at the LHC with $\sqrt{s} = 14$ TeV. A top mass of $m_t = 175$ GeV has been used for the event generation. Shown in the plot are the idealised situation without ISR in the event generation (solid curve), the influence of ISR if no correction method is used (short dashed), the result for application of the kinematic boost correction only (long dashed), and the boost correction with Sudakov re-weighting (dash-dotted). The likelihood reflects statistical errors only.

Evidently it is not possible to reconstruct the entire sequence of ISR branchings in the correct order from the event data. For most events, however, one microscopic branching process carries most p_T of all ISR from one leg –due to the p_T dependencies of the Sudakov factor–, so that a reasonable approximation can be obtained by adding up all ISR momenta stemming from one leg and calculating the Sudakov factor for one single branching with the summed momentum $p_{T,E}^2 = p_{T,ISR}^2$.

Since the ISR tends to be emitted at low angle, we approximate the ratio z by the longitudinal momentum components,

$$z \approx \frac{p_{in,z}}{p_{in,z} + p_{rad,z}}, \quad (5.9)$$

where p_{in} is the momentum of the incoming parton of the hard collision process and p_{rad} is the momentum of the ISR associated with this leg, see Fig. 5.1.

Fig. 5.2 shows numerical results for the MEM likelihood fit for the example of top-quark pair production with di-leptonic decays (Eq. (5.1)). The panel illustrates the impact of ISR if no special treatment for it is used : For reference, the solid curve shows the idealised situation without ISR in the event generation, so that each event contains exactly four visible partons (two b -quarks and two leptons). The dashed curve, on the other hand, corresponds to event generation with ISR, but ISR is not accounted for in

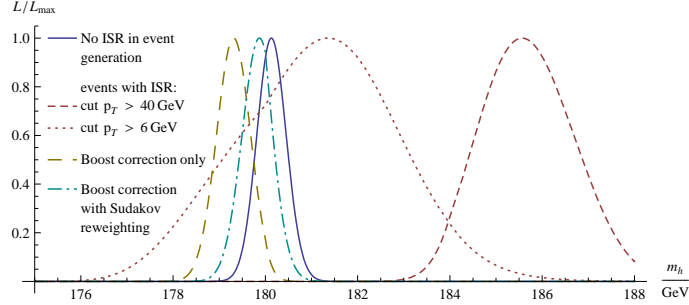


FIGURE 5.3 – Reconstruction of the Higgs boson mass from a matrix element likelihood fit to 1000 parton-level di-lepton events at the LHC with $\sqrt{s} = 14$ TeV. A Higgs mass of $m_h = 180$ GeV has been used for the event generation, so that the W^+W^- is open and dominant. The plot compares the idealised situation without ISR in the event generation (solid curve) with simulation results including ISR, and either no correction (short dashed) or purely kinematical boost correction (long dashed). The likelihood reflects statistical errors only.

the likelihood fit ; instead events with ISR with $p_T > 40$ GeV have been vetoed. This generation is based on the same number of partonic events. As evident from the plot, the fit yields a central value for the top quark mass close to the true input value, but the statistical uncertainty is increased by a factor of about two (as can be seen from the larger width of the curve), partially due to lower number of events passing the selection cuts – about 27%.

Fig. 5.2 demonstrates also the effect of the boost correction. As expected, the statistical error is not increased by applying this method. Applying only the kinematical boost correction, without the Sudakov re-weighting, leads to a central value for the fitted top mass that is shifted downwards by about 0.5 GeV. While this is still marginally consistent within the 2-sigma confidence interval, it is indicative of a slight systematic bias. If in addition the Sudakov factor (5.8) is included, the central value of the reconstructed top mass is much closer to the true input value and fully consistent within 1-sigma interval.

Fig. 5.3 shows results for Higgs production with decay to $l^+l^-\nu_l\bar{\nu}_l$ through a pair of W bosons (Eq. (5.2)). As we can see from the figure, such s -channel resonance processes are even more sensitive to the influence of ISR. Indeed, the Higgs mass is not properly reconstructed by the MEM likelihood fit even if ISR jets with $p_T > 40$ GeV are vetoed –it is only when the veto threshold is lowered to an unrealistically low value of 6 GeV that the fit becomes marginally consistent with the correct input value $m_h = 180$ GeV. On the other hand, the purely kinematical boost correction (without

reweighting) already yields a fit result that is very close to $m_h = 180$ GeV, while inclusion of the Sudakov reweighting leads to near-perfect agreement with the input value.

This strong sensitivity of the MEM fit to ISR is a particular feature of processes with narrow s -channel resonances, where $\Gamma_{\text{res}} \ll m_{\text{res}}$ [*e.g.* process (5.2) with $m_h = 180$ GeV and $\Gamma_h \approx 0.6$ GeV]. By ignoring ISR with transverse momenta of a few GeV, the best-fit centre-of-mass energy of the hard process can be shifted by a similar amount of a few GeV. In contrast, a pair production process without an s -channel resonance is much less sensitive to the precise value of the incident momenta $p_{\text{in}}^{(i)}$.

While the application of the boost correction is straightforward at the parton level, the situation becomes a bit more complex, however, in a more realistic framework with jet fragmentation and hadronisation, as will be shown in the next Section.

5.2 Initial State Radiation at the hadron level

In this Section the influence of ISR is investigated in a setup including parton showering, hadronisation and a simple detector simulation in the event generation. As before, events have been generated with PYTHIA 6.4 [101], but now using the information about the fully hadronised events including also underlying events, which have been passed through the fast detector simulation PGS [87] with general LHC detector parameters. For top-quark pair production with di-leptonic decay (Eq. (5.1)), all events in the sample are required to contain two leptons and at least two reconstructed jets with $p_T > 50$ GeV, but no other selection cuts besides the intrinsic detector acceptance have been applied. Acceptance Term have been fitted according to the method as described in the previous Chapters. We checked that the presence of the initial state radiation didn't have any impact on the reconstruction of jets inside PGS. Accordingly, we use the same transfer functions that the one developed in Chap. 4.

As before and for the sake of the generality and of the simplicity, we will not consider heavy flavour tagging and consider all permutations of the jets in the event, irrespective of their flavour content, as candidates to come from the top quark decay. The remaining jets are interpreted as stemming from ISR.³

Fig. 5.4 shows how ISR can affect the likelihood fit if ISR is not accounted for in the matrix elements. The solid curve shows again the situation without ISR in the event generation. The small bias can be related to FSR effects –which could be corrected with a more accurate parameterisation of the transfer functions. The short-dashed curve

3. If an event has more than four jets we only permute the four hardest jets to save computing time.

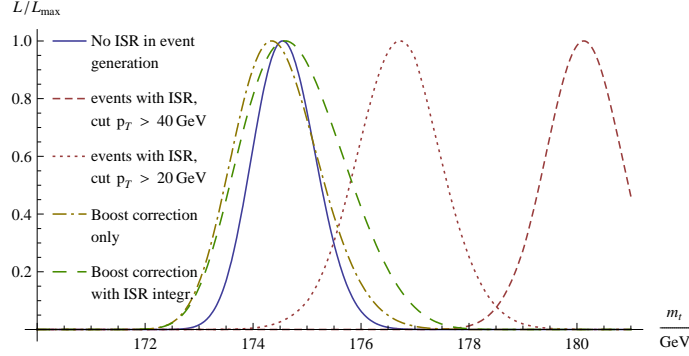


FIGURE 5.4 – Reconstruction of the top quark mass from a matrix element likelihood fit to 1000 hadron-level di-lepton $t\bar{t}$ events at the LHC with $\sqrt{s} = 14$ TeV. A top mass of $m_t = 175$ GeV has been used for the event generation. The solid curve corresponds to the idealised situation without ISR in the event generation, while the result for uncorrected ISR is shown for a veto on extra jets with $p_T > 40$ GeV (short dashed) and $p_T > 20$ GeV (dotted). Also shown are the effect of the purely kinematical boost correction (dash-dotted) and the boost correction with ISR transfer functions (long dashed). The likelihood reflects statistical errors only.

corresponds to inclusion of ISR in the event generation but not in the MEM likelihood fit, and events with more than two jets with $p_T > 40$ GeV have been excluded from the fit. In spite of this cut, the central value for the fitted top mass is shifted significantly compared to the input value $m_t = 175$ GeV, a feature that was not observed in the parton-level analysis (see Fig. 5.2). It can be explained by the fact that ISR typically generates multiple jets per event, and even if each jet has $p_T < 40$ GeV, the total transverse ISR momentum can be much larger. In events with very hard ISR the kinematics of the final state particles are substantially modified, so that the phase-space integration for matrix elements without ISR correction is sometimes pushed into an unphysical region.

The situation improves somewhat when the jet p_T cut is lowered to 20 GeV (long-dashed curve in Fig. 5.4), but the fit result is still inconsistent with the input value $m_t = 175$ GeV. Moreover, such a low cut will be subject to large systematic experimental uncertainties.

Therefore it is necessary to take into account and correct for ISR in the MEM fit, as shown in Fig. 5.4. In order to perform the boost correction, each ISR jet needs to be associated with one of the incoming legs. A simple rule is to assume that jets in the left hemisphere stem from the incident parton coming from the right, and *vice versa*. As a

first step, we will not consider a resolution function for the ISR. Indeed, on average the mis-measurements and UE contributions should compensate each other. Similar to the parton-level analysis, the application of the kinematical boost correction (short-dashed curve) leads to a downward shift in the central value of the fitted top mass.

As evident from the figure, the purely kinematical boost correction already leads to a satisfactory likelihood fit for top-quark pair production events. The situation is different, however, for processes with a narrow s -channel resonance, like Higgs production (Eq. (5.2)), since we have seen that this class of processes is very sensitive to ISR. Numerical results for the MEM fit are shown in Fig. 5.5, which shows that the boost correction does not lead to a good fit. This can be explained by the fact that on average the measured ISR jet momenta do not exactly agree with the parton-level ISR momenta – due both to detector effect but also due to the presence of FSR and UE. Such measurement inaccuracies have a substantial impact for Higgs production processes due to its strong sensitivity on the p_T of ISR.

One can try to account for these effects by including a transfer function for each incident leg (in addition to the transfer functions for the outgoing legs of the matrix element). This transfer function parametrises the relation between the transverse momentum of the incident partons of the hard process and the measured momenta of the ISR jets in each hemisphere. We use a two-component transfer function, employing a double-Gaussian when the measured ISR p_T^{vis} is non-zero, and a single Gaussian in logarithmic scale otherwise :

$$W_{\text{ISR}}(p_T, p_T^{\text{vis}}) = \frac{1}{\sqrt{\pi} b_2 p_T} e^{-(\log(p_T) - b_1)^2 / (2b_2^2)}, \quad \text{for } p_T^{\text{vis}} < p_T^0, \quad (5.10)$$

The boundary p_T^0 between the two regions should be chosen near the sensitivity limit of the detector (typically a few GeV), but we have checked that the results are not appreciably affected by varying p_T^0 between 5 and 15 GeV.

When using ISR transfer functions one needs to integrate over the partonic p_T of each leg, so that the total integration dimension is increased by two. Nevertheless, when using an adaptive algorithm like VEGAS [83], the integration time grows only by a factor of less than 10.

Fig. 5.5 demonstrates the effect of the boost correction without and with ISR transfer functions for the Higgs production process (Eq. (5.2)). The plot shows that the ISR transfer functions properly take into account the typical energy resolution and jet smearing effects and the fit result is consistent with the input value $m_h = 180$ GeV.

Note that Fig. 5.5 shows two curves for the result with ISR transfer functions, which correspond to transfer functions tuned to $t\bar{t}$ and $h \rightarrow WW$ Monte-Carlo events, res-

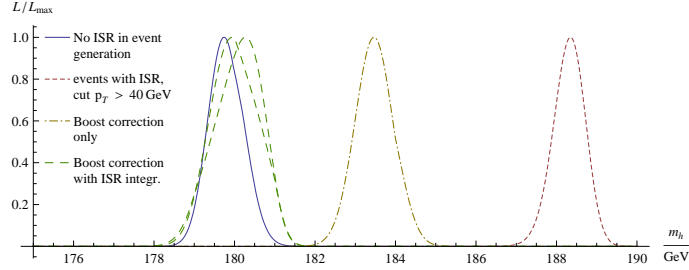


FIGURE 5.5 – Reconstruction of the Higgs boson mass from a matrix element likelihood fit to 1000 hadron-level di-lepton events at the LHC with $\sqrt{s} = 14$ TeV. A Higgs mass of $m_h = 180$ GeV has been used for the event generation. The plot compares the idealised situation without ISR in the event generation (solid curve) with simulation results including ISR, and either no correction (short dashed) or the kinematical boost correction without (short dashed) and with (long dashed) inclusion of ISR transfer functions. The likelihood reflects statistical errors only.

pectively. The likelihood curves are almost identical for the two cases, which demonstrates that the transfer functions are very insensitive to the hard process.

For the case of top-quark pair production, the fit result for the boost correction with ISR transfer functions is shown by the long-dashed curve in Fig. 5.4. It agrees very well with the input value $m_t = 175$ GeV, but in contrast to Higgs production, the purely kinematical boost correction is already satisfactory so that the inclusion of the transfer functions does not lead to a significant improvement here. On the other hand the statistical error is slightly increased but this should be compensated by the fact that this takes into account the systematic effect linked to the scale determination of ISR.

So far we have shown that the boost correction method with ISR transfer functions is a robust and practical technique for dealing with initial-state QCD radiation in experimental likelihood fits based on the MEM. We have still to check how our method is affected by systematic uncertainties. The largest systematic uncertainty is expected to be related to the jet energy scale. This uncertainty can be taken into account by keeping the jet energy scale as a free parameter in the fit [70,71,72,73]. However, a proper analysis of this and other experimental systematic errors requires a more sophisticated detector simulation and is beyond our scope.

We will have a closer look at theoretical systematic error sources. As already mentioned above, we have checked that the variation of the lower p_T cutoff for ISR jets within reasonable ranges has a negligible effect on the fit results. Similarly, it has been shown that the ISR transfer functions are approximately universal and depends very little on the details of the hard scattering process (see Fig. 5.5).

Furthermore, we estimate the systematic error stemming from the parton distribution functions (PDF) by comparing fit results for CTEQ6L1 and CTEQ6M PDF [86]. Here we only modify the PDF in the MEM fit, while using in both cases the same event file and transfer functions, which have been determined with CTEQ6L1 PDF. We find a negligible difference between the results for CTEQ6L1 and CTEQ6M PDF and thus conclude that the systematic error from this source is very small.

Conclusions

“The main purpose of science is simplicity and as we understand more things, everything is becoming simpler.”

Edward Teller

The Matrix Element Method is a powerful analysis technique based on a very simple idea : use a squared matrix element to associate a probability of coming from a specific partonic process to an event as seen in a detector. The maximisation of the likelihood –based on a sample of events– provides then a sensitive and natural variable to disentangle the signal from the background. The effectiveness of this method was proven by DØ and CDF collaboration, not only in the top-quark mass measurement but also the single-top observation and for the exclusion of the intermediate mass Higgs. We can expect that both CMS and ATLAS will follow the same route. Simple as it looks, the method, however, entails a very complicated integration over phase space, a technical issue that has hampered so far its widespread use in other cases as well as a more detailed study of the possible systematic effects that can be hidden in some common assumptions.

In this thesis, we have presented a new general algorithm (and its actual implementation) that solves the problem of the computation of the weights for any decay chain of interest. A dedicated and automated package –MADWEIGHT– integrates over phase space matrix elements together with transfer functions. He performs this by combining different optimised phase-mappings in a process dependent way. At the present stage, the only limitation of our approach stems from the use of mappings which are

invertible analytically. However, the modular structure of our algorithm makes the extension to non-analytical change of variables straightforward.

The availability of a tool such as MADWEIGHT, which is fully automatic, spares the user from focusing on the technical details of matrix element generation and integration over phase-space. This opens the way to a potentially large number of applications. Not only the measurement of masses or cross sections in the Standard Model could be achieved in a effortless and more efficient way, but the re-weighting technique could also be employed in the search and identification of new physics models, as underlined in the example where we measure the charged Higgs cross-sections.

The quest for new physics is a two step process. First a deviation from the Standard Model needs to be identified. Even in this phase, the use of the matrix-element re-weighting procedure can enhance our sensitivity to the presence of new physics processes, in a model independent way. With this aim in mind, we have proposed and developed an original technique to evaluate the differential cross sections from a sample of events. We called this method the *Differential MEM* (DMEM). Based on the Standard Model matrix elements and the detector transfer functions, we re-weight any possible kinematical configuration and use it to evaluate –on a event by event basis– the marginal distribution for any variable of interest. We have shown that the sum of those distributions provides an accurate estimator of the differential cross section. We have also shown, through examples, that this estimator is quite sensitive to the presence of new physics events, leading to observable deviations from the Standard Model expected curve.

Finally, we also performed, for the first time, a systematic study of the impact of QCD radiation on the MEM. Normally, a fixed number of external partons is used (corresponding to the Born process), and it is not possible to include the high-multiplicity initial state radiation. At TEVATRON, events with ISR are eliminated by applying a veto cut. We have shown that, in addition to reduce the statistics, those cuts might induce a non-trivial bias on the measurement. We have then proposed a method to include the effect of ISR by correcting the momenta of the incident partons in the matrix element on an event-by-event basis. Concretely, the incoming parton momenta are boosted by the transverse momenta of the ISR. This method has been first studied and tested at the partonic level before being extended to a more realistic situation with fully hadronized events and a fast detector response simulation. In order to take into account the detector resolution, we have considered a specific transfer function for the ISR. Our results are encouraging as they lead to a stable MEM fit, resulting in excellent agreement with the underlying input value. Finally, we also showed that this method is very robust under the theoretical systematics uncertainties.

In the near future, MADWEIGHT will be included inside the brand-new MADGRAPH 5 framework [105]. This will give the opportunity to improve the code and to make it

more generic in allowing, for example, non decay chain processes which are sometimes important in order to re-weight events according to background hypotheses. Moreover the systematic effect of the method due to Final State Radiation could be studied further.

Since the first top-quark mass measurement made with the Matrix-Element Method made at the TEVATRON, the re-weighting method shows astonishing sensitivity and applications. In the near future, thanks to both TEVATRON and LHC, we can expect that this method will help to measure the mass of the Higgs and/or to identify new particles.

Annexe **A**

Changes of Variables

*“Everything should be as simple as it is,
but not simpler.”*

Albert Einstein

A.1 Phase-space measure associated with the final blocks

A.1.1 FB A

The notation for the phase-space variables associated with this main block is given in Figure A.1. The two momenta p_1 and p_2 correspond to the visible particles that enter into the main block, along with the Bjorken fractions q_1 and q_2 . The standard phase-space parametrisation associated with this main block reads

$$dq_1 dq_2 \frac{d^3 p_1}{(2\pi)^3 2E_1} \frac{d^3 p_2}{(2\pi)^3 2E_2} (2\pi)^4 \delta^4(P_{\text{in}} - P_{\text{fin}}). \quad (\text{A.1})$$

The four-vectors P_{in} and P_{fin} refer to the total momenta in the initial and final states, respectively. In our procedure we apply a change of variables that leads to the following parametrisation of the phase-space measure

$$\frac{1}{16\pi^2 E_1 E_2} d\theta_1 d\phi_1 d\theta_2 d\phi_2 \times J, \quad (\text{A.2})$$

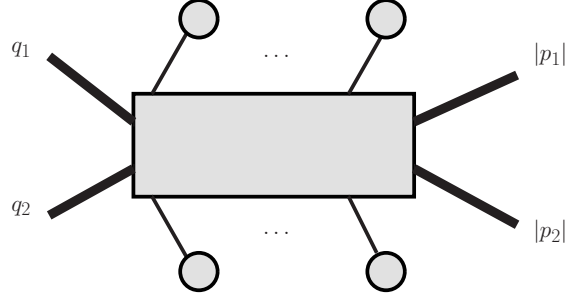


FIGURE A.1 – Notation for the kinematics of FB A.

where θ_i and ϕ_i refer to the polar and azimuthal angles of particle i with respect to the beam axis. The Jacobian J of this transformation reads

$$J = \frac{2}{s} |\mathbf{p}_1|^2 |\mathbf{p}_2|^2 |\cos \phi_1 \sin \phi_2 - \sin \phi_1 \cos \phi_2|^{-1}, \quad (\text{A.3})$$

where s is the squared invariant mass of the colliding hadrons. The energies E_1, E_2 of the final particles in the main block are adjusted to balance the transverse momentum $\mathbf{p}_T^{\text{branches}}$ of all the branches represented by the blobs in Figure A.1. We assume that this transverse momentum is different from zero, except may be in a region of null measure (see the discussion in Section 3.8). This requires the number of particles in the final state to be larger than or equal to three. Then the variables $|\mathbf{p}_1|, |\mathbf{p}_2|$ can be expressed as the solution of the following linear system

$$|\mathbf{p}_1| \sin \theta_1 \cos \phi_1 + |\mathbf{p}_2| \sin \theta_2 \cos \phi_2 = -p_x^{\text{branches}}, \quad (\text{A.4a})$$

$$|\mathbf{p}_1| \sin \theta_1 \sin \phi_1 + |\mathbf{p}_2| \sin \theta_2 \sin \phi_2 = -p_y^{\text{branches}}. \quad (\text{A.4b})$$

The Bjorken fractions q_1, q_2 are then fixed by imposing the conservation of total energy and total momentum along the beam axis.

A.1.2 FB B

The notation for the phase-space variables associated with this main block is given in Figure A.2. The momentum p_1 corresponds to the missing particle that belongs to the main block, along with the Bjorken fractions q_1 and q_2 . The momentum p_2 corresponds to the branch that is directly connected to that missing particle. The variable s_{12} is the invariant $(p_1 + p_2)^2$. The standard phase-space parametrisation associated with this constrained sector reads

$$dq_1 dq_2 \frac{d^3 p_1}{(2\pi)^3 2E_1} (2\pi)^4 \delta^4 (P_{\text{in}} - P_{\text{fin}}). \quad (\text{A.5})$$

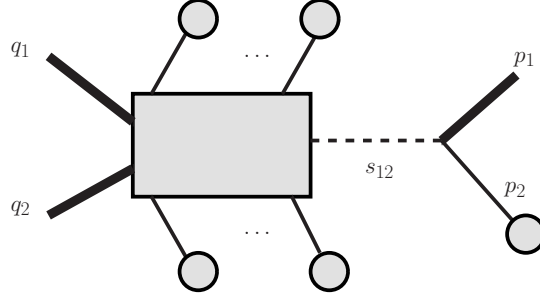


FIGURE A.2 – Notation for the kinematics of FB B.

The four-vectors P_{in} and P_{fin} refer to the total momenta in the initial and final states, respectively. In our procedure we apply a change of variables that leads to the following parametrisation of the phase-space measure

$$\frac{1}{4\pi E_1} ds_{12} \times J. \quad (\text{A.6})$$

The Jacobian J of this transformation is given by

$$J = \frac{E_1}{s} |p_{2z} E_1 - E_2 p_{1z}|^{-1}, \quad (\text{A.7})$$

where s is the squared invariant mass of the colliding hadrons. The transverse momentum the missing particle is fixed by requiring that it balances the transverse momentum of all the branches represented by the blobs in Figure A.2. The component p_{1z} of momentum along the beam axis is fixed by imposing the invariant mass condition

$$(p_1 + p_2)^2 = s_{12}. \quad (\text{A.8})$$

If the energy E_1 of the missing particle is treated as an independent parameter, the left side of Eq. (A.8) is a first-order polynomial in p_{1z} . We therefore obtain a unique expression for p_{1z} in terms of E_1 . The mass-shell condition associated with the missing particle gives rise to up to two solutions for the energy E_1 . Each solution that gives a real positive value for E_1 and that leads to values of the Bjorken fractions q_1 and q_2 between 0 and 1 is kept, as it corresponds to a distinct physical phase-space point at which the Jacobian in Eq. (A.7) and the integrand must be evaluated.

A.1.3 FB C

The notation for the phase-space variables associated with this main blob is given in Figure A.3. The momentum of the missing particle is denoted by p_1 , the momentum

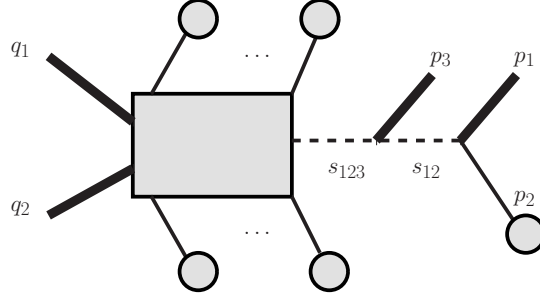


FIGURE A.3 – Notation for the kinematics of FB C.

of the branch directly connected to the missing particle is denoted by p_2 , the momentum of the massless visible particle in the main block is denoted by p_3 . The Bjorken fractions are denoted by q_1 and q_2 . The variables s_{12} and s_{123} refer to the invariants $(p_1 + p_2)^2$ and $(p_1 + p_2 + p_3)^2$, respectively. The standard phase-space parametrisation associated with this main block reads

$$dq_1 dq_2 \frac{d^3 p_1}{(2\pi)^3 2E_1} \frac{d^3 p_3}{(2\pi)^3 2E_3} (2\pi)^4 \delta^4(P_{\text{in}} - P_{\text{fin}}). \quad (\text{A.9})$$

The four-vectors P_{in} and P_{fin} refer to the total momenta in the initial and final states, respectively. In our procedure we apply a change of variables that leads to the following parametrisation of the phase-space measure

$$\frac{1}{16\pi^2 E_1 E_3} d\phi_3 d\theta_3 ds_{12} ds_{123} \times J. \quad (\text{A.10})$$

The Jacobian J of this transformation is given by

$$\begin{aligned} J = & \sin\theta_3 \frac{E_3^2 E_1}{s} \left| \chi E_2 p_{1z} - \chi E_1 p_{2z} - \right. \\ & 2 \cos(\phi_3) \cos(\theta_3) E_2 p_{1x} E_3 \sin(\theta_3) + 2 \cos(\phi_3) \cos(\theta_3) E_1 p_{2x} E_3 \sin(\theta_3) - \\ & 2 \cos(\phi_3) p_{1z} p_{2x} E_3 \sin(\theta_3) + 2 \cos(\phi_3) p_{1x} p_{2z} E_3 \sin(\theta_3) - \\ & 2 \cos(\theta_3) E_2 p_{1y} E_3 \sin(\phi_3) \sin(\theta_3) + 2 \cos(\theta_3) E_1 p_{2y} E_3 \sin(\phi_3) \sin(\theta_3) - \\ & 2 p_{1z} p_{2y} E_3 \sin(\phi_3) \sin(\theta_3) + 2 p_{1y} p_{2z} E_3 \sin(\phi_3) \sin(\theta_3) + \\ & 2 \cos(\phi_3)^2 E_2 p_{1z} E_3 \sin(\theta_3)^2 - 2 \cos(\phi_3)^2 E_1 p_{2z} E_3 \sin(\theta_3)^2 + \\ & \left. 2 E_2 p_{1z} E_3 \sin(\phi_3)^2 \sin(\theta_3)^2 - 2 E_1 p_{2z} E_3 \sin(\phi_3)^2 \sin(\theta_3)^2 \right|^{-1}, \quad (\text{A.11}) \end{aligned}$$

with $\chi = 2p_3 \cdot (p_1 + p_2)/E_3$ and s standing for the squared invariant mass of the colliding hadrons.

If we treat the variables E_1 and $\alpha = 2p_1 \cdot p_3$ as two independent parameters, the components of the three momentum \mathbf{p}_1 of the missing particle and the energy $E_3 = |\mathbf{p}_3|$ of the massless visible particle can be expressed as the solution of the following linear system of four equations

$$(p_1 + p_2)^2 = s_{12} \quad (\text{A.12a})$$

$$(p_1 + p_2 + p_3)^2 = s_{123} \quad (\text{A.12b})$$

$$p_{1x} + E_3 \sin \theta_3 \cos \phi_3 = -p_{Tx}^{\text{branches}} \quad (\text{A.12c})$$

$$p_{1y} + E_3 \sin \theta_3 \sin \phi_3 = -p_{Ty}^{\text{branches}} \quad (\text{A.12d})$$

that is parametrised by the momentum p_2 , by the angles θ_3 and ϕ_3 , by the total transverse momentum $\mathbf{p}_T^{\text{branches}}$ of all the branches represented, by the blobs in Figure A.3 and by the variables α and E_1 . The next step is to determine the values of the variables α and E_1 . The mass-shell condition for the missing particle of momentum p_1 and the equation $2p_1 \cdot p_3 = \alpha$ defines a system of two coupled quadratic equations in the variables E_1 and α , parametrised by the momenta of the blocks. This system can be solved analytically. There are up to four solutions for E_1 and α . Each solution that is physical (*i.e.*, such that $|p_3| > 0$, $E_1 > 0$ and each of the Bjorken fractions q_1, q_2 is between 0 and 1) corresponds to a distinct phase-space point at which the Jacobian in Eq. (A.11) and the integrand must be evaluated.

A.1.4 FB D

The notation for the phase-space variables associated with this constrained sector is given in Figure A.4. The momenta of the missing particles are denoted by p_1 and p_2 ,

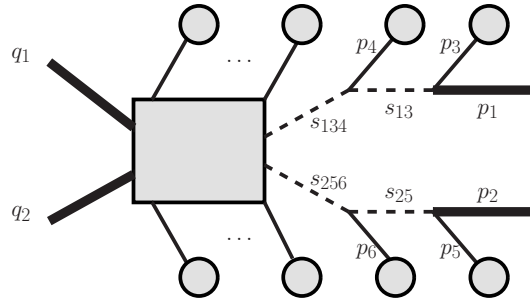


FIGURE A.4 – Notation for the kinematics of FB D.

the momenta of the branches connected to the main block are denoted by p_3, p_4, p_5

and p_6 . The Bjorken fractions are denoted by q_1 and q_2 . The variables s_{ij} and s_{ijk} refer to the invariants $(p_i + p_j)^2$ and $(p_i + p_j + p_k)^2$, respectively. The standard phase-space parametrisation associated with this main block reads

$$dq_1 dq_2 \frac{d^3 p_1}{(2\pi)^3 2E_1} \frac{d^3 p_2}{(2\pi)^3 2E_2} (2\pi)^4 \delta^4 (P_{\text{in}} - P_{\text{fin}}). \quad (\text{A.13})$$

The four-vectors P_{in} and P_{fin} refer to the total momenta in the initial and final states, respectively. In our procedure we apply a change of variables that leads to the following parametrisation of the phase-space measure

$$\frac{1}{16\pi^2 E_1 E_2} ds_{13} ds_{134} ds_{25} ds_{256} \times J. \quad (\text{A.14})$$

The Jacobian J of this transformation is given by

$$\begin{aligned} J = & \frac{E_1 E_2}{8s} \left| E_3 \left\{ E_5 [p_{34z} (p_{1y} p_{2z} p_{56x} - p_{1x} p_{2z} p_{56y}) \right. \right. \\ & - p_{1y} p_{2x} p_{56z} + p_{1x} p_{2y} p_{56z}) + p_{1z} (-p_{2z} p_{34y} p_{56x} + \\ & p_{2z} p_{34x} p_{56y} - p_{2y} p_{34x} p_{56z} + p_{2x} p_{34y} p_{56z}) \left. \right] + \\ & (E_{56} p_{2z} - E_2 p_{56z}) (p_{1z} p_{34y} p_{5x} - p_{1y} p_{34z} p_{5x} - p_{1z} p_{34x} p_{5y} + \\ & p_{1x} p_{34z} p_{5y}) + [E_{56} (p_{1z} p_{2y} p_{34x} - p_{1z} p_{2x} p_{34y} + p_{1y} p_{2x} p_{34z} - \\ & p_{1x} p_{2y} p_{34z}) + E_2 (p_{1z} p_{34y} p_{56x} - p_{1y} p_{34z} p_{56x} - p_{1z} p_{34x} p_{56y} + \\ & p_{1x} p_{34z} p_{56y})] p_{5z} \left. \right\} + E_{34} \left\{ E_5 p_{2z} (p_{1z} p_{3y} p_{56x} - p_{1y} p_{3z} p_{56x} \right. \\ & - p_{1z} p_{3x} p_{56y} + p_{1x} p_{3z} p_{56y}) + E_5 (p_{1z} p_{2y} p_{3x} - p_{1z} p_{2x} p_{3y} \\ & + p_{1y} p_{2x} p_{3z} - p_{1x} p_{2y} p_{3z}) p_{56z} - (E_{56} p_{2z} - E_2 p_{56z}) \\ & (p_{1z} p_{3y} p_{5x} - p_{1y} p_{3z} p_{5x} - p_{1z} p_{3x} p_{5y} + p_{1x} p_{3z} p_{5y}) \\ & - [E_{56} (p_{1z} p_{2y} p_{3x} - p_{1z} p_{2x} p_{3y} + p_{1y} p_{2x} p_{3z} - p_{1x} p_{2y} p_{3z}) + \\ & E_2 (p_{1z} p_{3y} p_{56x} - p_{1y} p_{3z} p_{56x} - p_{1z} p_{3x} p_{56y} + p_{1x} p_{3z} p_{56y})] p_{5z} \left. \right\} + \\ & E_1 \left\{ [E_5 (p_{2z} (-p_{34z} p_{3y} p_{56x} + p_{34y} p_{3z} p_{56x} + \right. \\ & p_{34z} p_{3x} p_{56y} - p_{34x} p_{3z} p_{56y}) + \\ & (-p_{2y} p_{34z} p_{3x} + p_{2x} p_{34z} p_{3y} + p_{2y} p_{34x} p_{3z} - p_{2x} p_{34y} p_{3z}) p_{56z}] + \\ & [E_{56} p_{2z} - E_2 p_{56z}) (p_{34z} p_{3y} p_{5x} - p_{34y} p_{3z} p_{5x} - p_{34z} p_{3x} p_{5y} + \\ & p_{34x} p_{3z} p_{5y}) + (E_{56} (p_{2y} p_{34z} p_{3x} - p_{2x} p_{34z} p_{3y} - p_{2y} p_{34x} p_{3z} + \\ & p_{2x} p_{34y} p_{3z}) + E_2 (p_{34z} p_{3y} p_{56x} - p_{34y} p_{3z} p_{56x} - p_{34z} p_{3x} p_{56y} + \\ & p_{34x} p_{3z} p_{56y})] p_{5z} \left. \right\} \Big|^{-1}, \quad (\text{A.15}) \end{aligned}$$

where $E_{ij} = E_i + E_j$, $p_{ij} = p_i + p_j$, and s is the squared invariant mass of the colliding hadrons in their centre-of-mass frame. If we treat the variables E_1 and E_2

as independent parameters, then the components of the three momenta $\mathbf{p}_1, \mathbf{p}_2$ of the missing particles can be expressed as the solution of the following linear system of six equations

$$(p_1 + p_3)^2 = s_{13}, \quad (\text{A.16a})$$

$$(p_1 + p_3 + p_4)^2 = s_{134}, \quad (\text{A.16b})$$

$$(p_2 + p_5)^2 = s_{25}, \quad (\text{A.16c})$$

$$(p_2 + p_5 + p_6)^2 = s_{256}, \quad (\text{A.16d})$$

$$p_{1x} + p_{2x} = -p_{Tx}^{\text{branches}}, \quad (\text{A.16e})$$

$$p_{1y} + p_{2y} = -p_{Ty}^{\text{branches}}, \quad (\text{A.16f})$$

that is parametrised by the momenta p_3, \dots, p_6 of the branches connected to the main block, by the total transverse momentum $\mathbf{p}_T^{\text{branches}}$ of all the branches represented by the blobs in Figure A.4 and by the variables E_1 and E_2 . The next step is to determine the values of the variables E_1 and E_2 . The mass-shell conditions for the two missing particles of momentum p_1 and p_2 define a system of two coupled quadratic equations in the variables E_1 and E_2 , that can be solved analytically. There are up to four solutions for E_1 and E_2 . Each solution that is physical (*i.e.*, such that $E_2 > 0$, $E_1 > 0$ and each of the Bjorken fractions q_1, q_2 is between 0 and 1) corresponds to a distinct phase-space point at which the Jacobian in Eq. (A.15) and the integrand must be evaluated.

A.1.5 FB E

The notation for the phase-space variables associated with this main blob is given in Figure A.5. The momenta of the missing particles are denoted by p_1 and p_2 , the

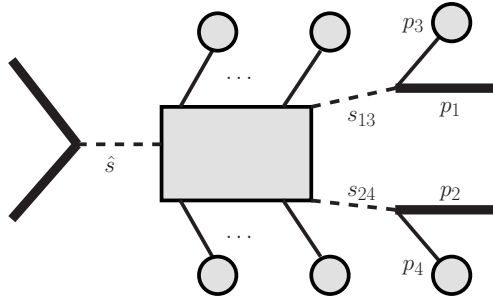


FIGURE A.5 – Notation for the kinematics of FB E.

momenta of the branches directly connected to these missing particles are denoted by p_3 and p_4 . The Bjorken fractions are denoted by q_1 and q_2 . The variables s_{ij} refer to the invariants $(p_i + p_j)^2$ and \hat{s} denotes the squared invariant mass of the colliding partons. The standard phase-space parametrisation associated with this FB reads

$$dq_1 dq_2 \frac{d^3 p_1}{(2\pi)^3 2E_1} \frac{d^3 p_2}{(2\pi)^3 2E_2} (2\pi)^4 \delta^4 (P_{\text{in}} - P_{\text{fin}}). \quad (\text{A.17})$$

The four-vectors P_{in} and P_{fin} refer to the total momenta in the initial and final states, respectively. In our procedure we apply a change of variables that leads to the following parametrisation of the phase-space measure

$$\frac{1}{16\pi^2 E_1 E_2} dy d\hat{s} ds_{13} ds_{24} \times J, \quad (\text{A.18})$$

where y is the rapidity of the colliding partons in the laboratory frame. The Jacobian J of this transformation is given by

$$J = \frac{E_1 E_2}{4s} \left| E_4 (p_{1z} p_{2y} p_{3x} - p_{1y} p_{2z} p_{3x} - p_{1z} p_{2x} p_{3y} + p_{1x} p_{2z} p_{3y} + p_{1y} p_{2x} p_{3z} - p_{1x} p_{2y} p_{3z}) + E_2 p_{1z} p_{3y} p_{4x} - E_1 p_{2z} p_{3y} p_{4x} - E_2 p_{1y} p_{3z} p_{4x} + E_1 p_{2y} p_{3z} p_{4x} - E_2 p_{1z} p_{3x} p_{4y} + E_1 p_{2z} p_{3x} p_{4y} + E_2 p_{1x} p_{3z} p_{4y} - E_1 p_{2x} p_{3z} p_{4y} + (E_2 p_{1y} p_{3x} + -E_1 p_{2y} p_{3x} - E_2 p_{1x} p_{3y} + E_1 p_{2x} p_{3y}) p_{4z} + E_3 (-p_{1z} p_{2y} p_{4x} + p_{1y} p_{2z} p_{4x} + p_{1z} p_{2x} p_{4y} - p_{1x} p_{2z} p_{4y} - p_{1y} p_{2x} p_{4z} + p_{1x} p_{2y} p_{4z}) \right|^{-1}. \quad (\text{A.19})$$

If we treat the variables E_1 , E_2 and p_{2y} as independent parameters, the other components of the momenta p_1, p_2 of the missing particles can be expressed as the solution of the following linear system of five equations

$$(p_1 + p_3)^2 = s_{13}, \quad (\text{A.20a})$$

$$(p_2 + p_4)^2 = s_{24}, \quad (\text{A.20b})$$

$$p_{1x} + p_{2x} = -p_x^{\text{branches}}, \quad (\text{A.20c})$$

$$p_{1y} + p_{2y} = -p_y^{\text{branches}}, \quad (\text{A.20d})$$

$$p_{1z} + p_{2z} = \sinh(y) \hat{s}^{1/2} - p_z^{\text{branches}}, \quad (\text{A.20e})$$

that is parametrised by the momenta of the branches p_3 and p_4 , by the total momentum p^{branches} of all the branches represented by the blobs in Figure A.5, by the rapidity y and the invariant mass $\hat{s}^{1/2}$ of the colliding partons and by the variables E_1 , E_2 and

p_{2y} . The next step is to fix the value of the variables E_1 , E_2 and p_{2y} . The variable E_1 can be expressed as a linear function of E_2 :

$$E_1 = \cosh(y)\hat{s}^{1/2} - E^{\text{branches}} - E_2. \quad (\text{A.21})$$

Then the mass-shell conditions for the two missing particles define a system of two coupled quadratic equations in the variables E_2 and p_{2y} . In this case, the quartic terms of the two equations have the same coefficients, and the system reduces to a linear equation and a quadratic equation. There are up to two solutions for E_2 and p_{2y} . Each solution that is physical (*i.e.*, such that $E_2 > 0$, $E_1 > 0$) corresponds to a distinct phase-space point at which the Jacobian in Eq. (A.19) and the integrand must be evaluated.

A.1.6 FB F

The notation for the phase-space variables associated with this constrained sector is given in Figure A.6. The momenta of the missing particles are denoted by p_1 and p_2 ,

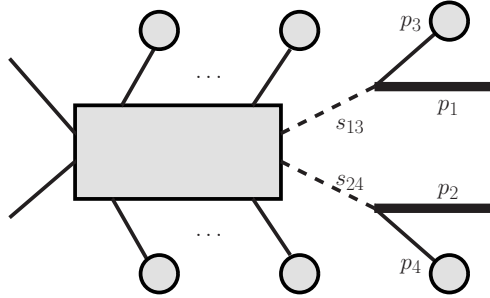


FIGURE A.6 – Notation for the kinematics of FB F.

the momenta of the branches directly connected to these missing particles are denoted by p_3 and p_4 . The Bjorken fractions are denoted by q_1 and q_2 . The variables s_{ij} refer to the invariants $(p_i + p_j)^2$. The standard phase-space parametrisation associated with this main block reads

$$dq_1 dq_2 \frac{d^3 p_1}{(2\pi)^3 2E_1} \frac{d^3 p_2}{(2\pi)^3 2E_2} (2\pi)^4 \delta^4 (P_{\text{in}} - P_{\text{fin}}). \quad (\text{A.22})$$

The four-vectors P_{in} and P_{fin} refer to the total momenta in the initial and final states, respectively. In our procedure we apply a change of variables that leads to the following parametrisation of the phase-space measure

$$\frac{1}{16\pi^2 E_1 E_2} dq_1 dq_2 ds_{13} ds_{24} \times J. \quad (\text{A.23})$$

The Jacobian J of this transformation is given by

$$\begin{aligned}
J = \frac{E_1 E_2}{4} & \left| E_4 (p_{1z} p_{2y} p_{3x} - p_{1y} p_{2z} p_{3x} - p_{1z} p_{2x} p_{3y} + p_{1x} p_{2z} p_{3y} + \right. \\
& p_{1y} p_{2x} p_{3z} - p_{1x} p_{2y} p_{3z}) + E_2 p_{1z} p_{3y} p_{4x} - E_1 p_{2z} p_{3y} p_{4x} - \\
& E_2 p_{1y} p_{3z} p_{4x} + E_1 p_{2y} p_{3z} p_{4x} - E_2 p_{1z} p_{3x} p_{4y} + E_1 p_{2z} p_{3x} p_{4y} + \\
& E_2 p_{1x} p_{3z} p_{4y} - E_1 p_{2x} p_{3z} p_{4y} + (E_2 p_{1y} p_{3x} - E_1 p_{2y} p_{3x} \\
& - E_2 p_{1x} p_{3y} + E_1 p_{2x} p_{3y}) p_{4z} + E_3 (-p_{1z} p_{2y} p_{4x} + p_{1y} p_{2z} p_{4x} + \\
& \left. p_{1z} p_{2x} p_{4y} - p_{1x} p_{2z} p_{4y} - p_{1y} p_{2x} p_{4z} + p_{1x} p_{2y} p_{4z}) \right|^{-1}. \quad (\text{A.24})
\end{aligned}$$

If we treat the variables E_1 , E_2 and p_{2y} as independent parameters, the other components of the momenta p_1, p_2 of the missing particles can be expressed as the solution of the following linear system of five equations,

$$(p_1 + p_3)^2 = s_{13}, \quad (\text{A.25a})$$

$$(p_2 + p_4)^2 = s_{24}, \quad (\text{A.25b})$$

$$p_{1x} + p_{2x} = -p_x^{\text{branches}}, \quad (\text{A.25c})$$

$$p_{1y} + p_{2y} = -p_y^{\text{branches}}, \quad (\text{A.25d})$$

$$p_{1z} + p_{2z} = s^{1/2}(q_1 - q_2)/2 - p_z^{\text{branches}}, \quad (\text{A.25e})$$

that is parametrised by the momenta p_3 and p_4 , by the total momentum p^{branches} of all the branches represented by the blobs in Figure A.6, by the Bjorken fractions q_1, q_2 and by the variables E_1, E_2 and p_{2y} . The next step is to fix the values of the variables E_1, E_2 and p_{2y} . The variable E_1 can be expressed as a linear function of E_2 :

$$E_1 = s^{1/2}(q_1 + q_2)/2 - E^{\text{branches}} - E_2. \quad (\text{A.26})$$

The mass-shell conditions for the two missing particles with momenta p_1 and p_2 define a system of two coupled quadratic equations in the variables E_2 and p_{2y} . In this case, the quartic terms of the two equations have the same coefficients, and the system reduces to a linear equation and a quadratic equation. There are up to two solutions for E_2 and p_{2y} . Each solution that is physical (*i.e.*, such that $E_2 > 0, E_1 > 0$) corresponds to a distinct phase-space point at which the Jacobian in Eq. (A.24) and the integrand must be evaluated.

A.2 Phase-space measure associated with the secondary blocks

A.2.1 PB A

The notation for the phase-space variables associated with this secondary block is given in Figure A.7. The momentum of the missing particle is denoted by p_1 , the

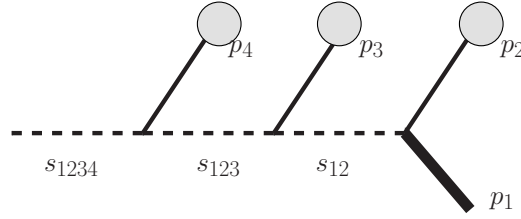


FIGURE A.7 – Notation for the kinematics of PB A.

momenta of the three branches connected to the block are denoted by p_2 , p_3 and p_4 . The variables s_{12} , s_{123} and s_{1234} refer to the invariants $(p_1 + p_2)^2$, $(p_1 + p_2 + p_3)^2$, and $(p_1 + p_2 + p_3 + p_4)^2$, respectively. The standard phase-space parametrisation associated with this block reads

$$\frac{d^3 p_1}{(2\pi)^3 2E_1}. \quad (\text{A.27})$$

In our procedure we apply a change of variables that leads to the following parametrisation of the phase-space measure

$$\frac{1}{(2\pi)^3 2E_1} ds_{12} ds_{123} ds_{1234} \times J. \quad (\text{A.28})$$

The Jacobian J of this transformation is given by

$$\begin{aligned} J = & \frac{E_1}{8} \left| E_4 (p_{1z} p_{2y} p_{3x} - p_{1y} p_{2z} p_{3x} - p_{1z} p_{2x} p_{3y} + p_{1x} p_{2z} p_{3y} + \right. \\ & p_{1y} p_{2x} p_{3z} - p_{1x} p_{2y} p_{3z}) + E_2 p_{1z} p_{3y} p_{4x} - E_1 p_{2z} p_{3y} p_{4x} - \\ & E_2 p_{1y} p_{3z} p_{4x} + E_1 p_{2y} p_{3z} p_{4x} - E_2 p_{1z} p_{3x} p_{4y} + E_1 p_{2z} p_{3x} p_{4y} + \\ & E_2 p_{1x} p_{3z} p_{4y} - E_1 p_{2x} p_{3z} p_{4y} + (E_2 p_{1y} p_{3x} - E_1 p_{2y} p_{3x} - \\ & E_2 p_{1x} p_{3y} + E_1 p_{2x} p_{3y}) p_{4z} + E_3 (-p_{1z} p_{2y} p_{4x} + p_{1y} p_{2z} p_{4x} \\ & \left. + p_{1z} p_{2x} p_{4y} - p_{1x} p_{2z} p_{4y} - p_{1y} p_{2x} p_{4z} + p_{1x} p_{2y} p_{4z}) \right|^{-1}. \quad (\text{A.29}) \end{aligned}$$

If we treat the variable E_1 as an independent parameter, the components of the three-momentum \mathbf{p}_1 of the missing particle can be expressed as the solution of the following linear system of three equations

$$(p_1 + p_2)^2 = s_{12}, \quad (\text{A.30a})$$

$$(p_1 + p_2 + p_3)^2 = s_{123}, \quad (\text{A.30b})$$

$$(p_1 + p_2 + p_3 + p_4)^2 = s_{1234}, \quad (\text{A.30c})$$

that is parametrised by the momenta p_2, p_3, p_4 of the branches connected to the block, and by the variable E_1 . The next step is to fix the value of the variable E_1 . The mass-shell condition for the missing particle with momentum p_1 defines a quadratic equation in the variable E_1 . There are up to two solutions for E_1 . Each solution that is physical (*i.e.*, such that $E_1 > 0$) corresponds to a distinct phase-space point at which the Jacobian in Eq. (A.29) and the integrand must be evaluated.

A.2.2 PB B

The notation for the phase-space variables associated with this secondary block is given in Figure A.8. The momentum of the missing particle is denoted by p_1 , the

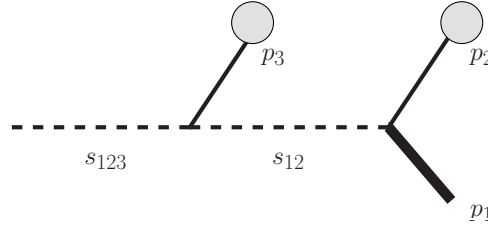


FIGURE A.8 – Notation for the kinematics of PB B.

momenta of the two branches connected to the block are denoted by p_2 and p_3 . The variables s_{12} and s_{123} refer to the invariants $(p_1 + p_2)^2$, and $(p_1 + p_2 + p_3)^2$, respectively. The standard phase-space parametrisation associated with this block reads

$$\frac{d^3 p_1}{(2\pi)^3 2E_1}. \quad (\text{A.31})$$

In our procedure we apply a change of variables that leads to the following parametrisation of the phase-space measure

$$\frac{1}{(2\pi)^3 2E_1} d\phi_1 ds_{12} ds_{123} \times J, \quad (\text{A.32})$$

where ϕ_i denotes the azimuthal angle of particle i . The Jacobian J of this transformation is given by

$$J = \frac{E_1}{4} p_{1T} \left| -\cos(\phi_1 - \phi_2) E_3 p_{2T} p_{1z} + \cos(\phi_1 - \phi_3) E_2 p_{3T} p_{1z} + E_3 p_{1T} p_{2z} - \cos(\phi_1 - \phi_3) E_1 p_{3T} p_{2z} - E_2 p_{1T} p_{3z} + \cos(\phi_1 - \phi_2) E_1 p_{2T} p_{3z} \right|^{-1} \quad (\text{A.33})$$

If we treat the variable E_1 as an independent parameter, the transverse momentum p_{1T} and the momentum component p_{1z} of the missing particle can be expressed as the solution of the following linear system of two equations

$$(p_1 + p_2)^2 = s_{12}, \quad (\text{A.34a})$$

$$(p_1 + p_2 + p_3)^2 = s_{123}, \quad (\text{A.34b})$$

that is parametrised by the momenta p_2 and p_3 of the branches connected to the block, by the azimuthal angle ϕ_1 and by the variable E_1 . The next step is to fix the value of the variable E_1 . The mass-shell condition for the missing particle with momentum p_1 defines a quadratic equation in the variable E_1 . There are up to two solutions for E_1 . Each solution that is physical (*i.e.*, such that $E_1 > 0$) corresponds to a distinct phase-space point at which the Jacobian in Eq. (A.33) and the integrand must be evaluated.

A.2.3 PB C/D

The notation for the phase-space variables associated with this secondary block is given in Figure A.9. The momentum of the missing particle is denoted by p_1 , the

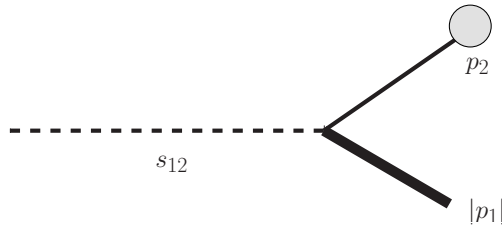


FIGURE A.9 – Notation for the kinematics of PB C/D.

momentum of the branch connected to the block is denoted by p_2 . The variable s_{12} refers to the invariant $(p_1 + p_2)^2$. The standard phase-space parametrisation associated with this block reads

$$\frac{d^3 p_1}{(2\pi)^3 2E_1}. \quad (\text{A.35})$$

In our procedure we apply a change of variables that leads to the following parametrisation of the phase-space measure

$$\frac{1}{(2\pi)^3 2E_1} d\phi_1 d\theta_1 ds_{12} \times J, \quad (\text{A.36})$$

where θ_1 and ϕ_1 denote the polar and azimuthal angles of the missing particle. The Jacobian J of this transformation is given by

$$J = \frac{E_1}{2} \sin \theta_1 |\mathbf{p}_1|^2 \left| |\mathbf{p}_1| E_2 - E_1 \hat{\mathbf{p}}_1 \cdot \mathbf{p}_2 \right|^{-1}. \quad (\text{A.37})$$

If we treat the variable E_1 as an independent parameter, the momentum modulus $|\mathbf{p}_1|$ of the missing particle can be expressed as the solution of the following linear equation

$$(p_1 + p_2)^2 = s_{12}, \quad (\text{A.38})$$

that is parametrised by the momentum p_2 of the branch connected to the block, by the polar and azimuthal angles θ_1 , ϕ_1 , and by the variable E_1 . The next step is to fix the value of the variable E_1 . The mass-shell condition for the missing particle with momentum p_1 defines a quadratic equation in the variable E_1 . There are up to two solutions for E_1 . Each solution that is physical (*i.e.*, such that $E_1 > 0$) corresponds to a distinct phase-space point at which the Jacobian in Eq. (A.37) and the integrand must be evaluated.

A.2.4 PB E

The notation for the phase-space variables associated with this secondary block is given in Figure A.10. The momenta of the visible particles are denoted by p_1 and p_2 ,

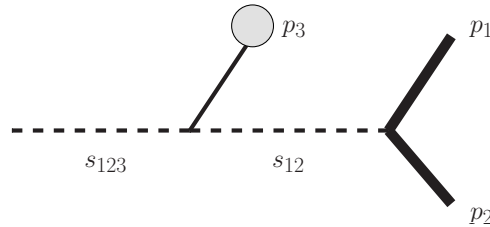


FIGURE A.10 – Notation of the kinematics for PB E.

the momentum of the branch connected to the block is denoted by p_3 . The variables

s_{12} and s_{123} refer to the invariants $(p_1 + p_2)^2$, and $(p_1 + p_2 + p_3)^2$. The standard phase-space parametrisation associated with this block reads

$$\frac{d^3 p_1}{(2\pi)^3 2E_1} \frac{d^3 p_2}{(2\pi)^3 2E_2}. \quad (\text{A.39})$$

In our procedure we apply a change of variables that leads to the following parametrisation of the phase-space measure

$$\frac{1}{(2\pi)^6 4E_1 E_2} d\theta_1 d\phi_1 d\theta_2 d\phi_2 ds_{12} ds_{123} \times J, \quad (\text{A.40})$$

where θ_i and ϕ_i denote the polar and azimuthal angles of particle i . The Jacobian J of this transformation is given by

$$J = \frac{E_2^2}{4} |\mathbf{p}_1|^2 \sin \theta_1 \sin \theta_2 \left| \left(|\mathbf{p}_1| |\mathbf{p}_2| / E_1 - |\mathbf{p}_2| f_{12} \right) (E_3 - |\mathbf{p}_3| f_{23}) \right. \\ \left. - (E_3 |\mathbf{p}_1| / E_1 - |\mathbf{p}_3| f_{13}) (E_1 - f_{12} |\mathbf{p}_1|) \right|^{-1}. \quad (\text{A.41})$$

where f_{ij} stands for $\mathbf{p}_i \cdot \mathbf{p}_j / |\mathbf{p}_i| |\mathbf{p}_j|$. The values for the momenta $|\mathbf{p}_1|$ and $|\mathbf{p}_2|$ can be obtained by solving the following linear system of equations

$$(p_1 + p_2)^2 = s_{12}, \quad (\text{A.42a})$$

$$(p_1 + p_2 + p_3)^2 = s_{123}. \quad (\text{A.42b})$$

By subtracting Eq. (A.42b) from Eq. (A.42a), we obtain an expression for E_1 that is a first order polynomial in $|\mathbf{p}_1|$ and $|\mathbf{p}_2|$. Inserting this expression into Eq. (A.42a) and into the equation defining the mass-shell condition for the particle of momentum p_1 , we obtain a system of two quadratic equations in $|\mathbf{p}_1|$ and $|\mathbf{p}_2|$ parametrised by the momentum p_3 , by the invariants s_{12} , s_{123} and by the angles θ_1 , θ_2 , ϕ_1 and ϕ_2 . This system can be solved analytically. There are up to four solutions for the modulus $|\mathbf{p}_1|$ and $|\mathbf{p}_2|$. Each solution that is physical (*i.e.*, such that $|\mathbf{p}_1| > 0$ and $|\mathbf{p}_2| > 0$) corresponds to a distinct phase-space point at which the Jacobian in Eq. (A.41) and the integrand must be evaluated.

Annexe **B**

Monte-Carlo and statistics associated to marginal distribution

“You cannot feed the hungry on statistics.”

Heinrich Heine

This Appendix will focus on technical details associated to the *Differential Matrix Element Method* described in Section 4.5. We will focus our attention on two different points. First we will present how to evaluate marginal distributions. Then we will present how we quantify the agreement between two distributions.

B.1 marginal distributions

Mathematically, the marginal distribution of a function $\mathcal{P}(\mathbf{p}^{vis})$ by a function $Z(\mathbf{p}^{vis})$ is defined as :

$$\frac{\partial \mathcal{P}(\mathbf{p}^{vis})}{\partial Z(\mathbf{p}^{vis})}. \tag{B.1}$$

For the weight defined in the MEM (Eq. 2.3) this corresponds to the following relation :

$$\left. \frac{\partial \mathcal{P}(\mathbf{p}^{vis})}{\partial Z(\mathbf{p}^{vis})} \right|_{Z^*} = \frac{1}{\sigma} \int d\Phi dx_1 dx_2 f_1(x_1) f_2(x_2) |M(\mathbf{p})|^2 W(\mathbf{p}, \mathbf{p}^{vis}) \delta(Z(\mathbf{p}^{vis}) - Z^*). \quad (\text{B.2})$$

Computing this integral for a given value of Z^* is quite complex, since the presence of an additional δ functions requires a dedicated phase-space generator. In order to gain in efficiency, we will rather estimate the marginal distribution on a “small” interval :

$$\int_{Z_i}^{Z_{i+1}} dZ^* \left. \frac{\partial \mathcal{P}(\mathbf{p}^{vis})}{\partial Z(\mathbf{p}^{vis})} \right|_{Z^*} = \frac{1}{\sigma} \int d\Phi dx_1 dx_2 f_1(x_1) f_2(x_2) |M(\mathbf{p})|^2 W(\mathbf{p}, \mathbf{p}^{vis}) \chi(Z(\mathbf{p}^{vis}), Z_i, Z_{i+1}),$$

where $\chi(Z(\mathbf{p}^{vis}), Z_i, Z_{i+1})$ is the characteristic function which is different from zero if $Z_i < Z(\mathbf{p}^{vis}) < Z_{i+1}$. Since $\mathcal{P}(\mathbf{p}^{vis})$ can be evaluated efficiently thanks to a specific phase-space mapping (See Chap. 3), we can expect that the same mapping will work for all the intervals. In order to avoid computational cost of having to reject Monte-Carlo points if they are not in the interval of interest, we will compute all the marginal contributions in a row –when computing the event’s weight. Each time we generate a Monte-Carlo point –in order to evaluate \mathcal{P} –, we calculate the value associated to the variable $Z(\mathbf{p}^{vis})$ and update the estimator of the integral associated to that given bin. With such a method, the precision on all bins should be achieved as long as the bin contributes significantly to the value of $\mathcal{P}(\mathbf{p}^{vis})$.

B.2 Correlation matrix and chi-square

After having evaluated differential cross sections, with the sum of the different marginal distributions, the question is to know if the observed differential cross section is compatible with the expected one. In order to quantify the agreement between this histogram and the expected value, we use a chi-squared variable. Since each event contributes to different bins, all bins are correlated to each other. In consequence the formula needed for the chi-squared variable is

$$\chi^2 = \sum_{i,j} \frac{(x_i - \bar{x}_i)}{\sigma_i} C_{i,j}^{-1} \frac{(x_j - \bar{x}_j)}{\sigma_j}, \quad (\text{B.3})$$

with C is the correlation matrix, x_i the value in the bin i , \bar{x}_i the expected value in bin i and σ_i the variance of the bin i . In practice, this estimator requires a minimal number

of entry by bin [106]. In consequence, we consider the bin only if the entries in the bin is larger than 15.

The estimator of quantity present in Eq. (B.3) is obtained by repeating the method on N_S different samples corresponding to the same luminosity. If we note x_i^a the value in the bin i for the a^{th} sample the estimator reads

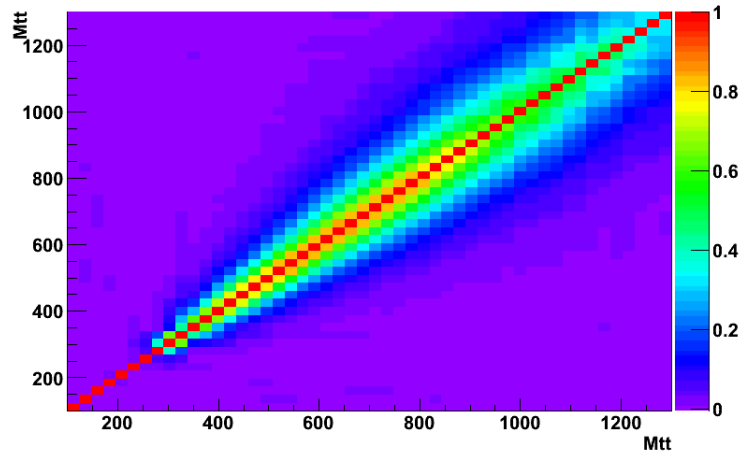
$$\bar{x}_i = \frac{1}{N_S} \sum_{a=1}^{N_S} x_i^a, \quad (\text{B.4})$$

$$\sigma_i = \frac{1}{N_S} \sum_{a=1}^{N_S} (x_i^a - \bar{x}_i)^2, \quad (\text{B.5})$$

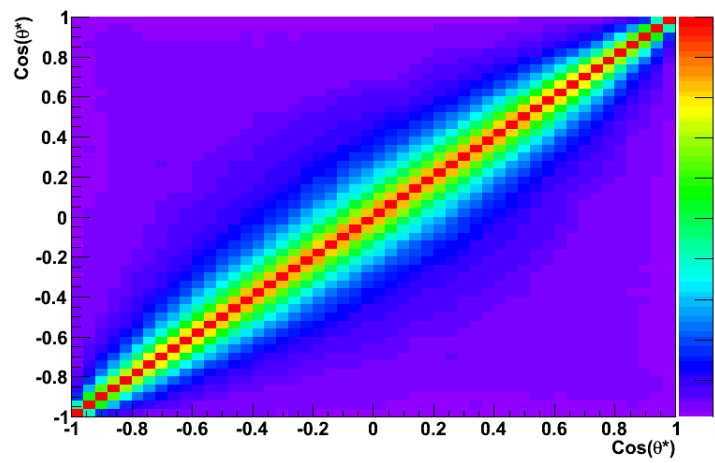
$$C_{i,j} = \frac{1}{N_S \sigma_i \sigma_j} \sum_{a=1}^{N_S} (x_i^a - \bar{x}_i) * (x_j^a - \bar{x}_j). \quad (\text{B.6})$$

Note that by construction $C_{i,j}$ is independent of the total luminosity of the samples. We checked that choosing a luminosity corresponding to one event, on average, in each sample provides the most accurate estimation.

Fig. B.1 presents the two correlation matrices used for the computation of the chi-squared variable in Sec. 4.5 corresponding respectively to the $t\bar{t}$ invariant mass and to the top diffusion angle in the $t\bar{t}$ rest frame.



(a)



(b)

FIGURE B.1 – Correlation Matrix for M_{tt} , $\cos(\theta_{t\bar{t}}^*)$ associated to the MKF method for top-quark pair production. The first graph (a) is the correlation matrix for the $t\bar{t}$ invariant mass, while the second (b) is the top diffusion angle in the $t\bar{t}$ rest frame. These matrices are evaluated with 100.000 Standard Model “detector like” events passing the selection cuts.

Bibliographie

- [1] Joint CDF and DO collaboration, “Combination of CDF and D0 Results on the Mass of the Top Quark”, 2010, arxiv :1007.3178.
- [2] Joint CDF and DO collaboration, “Combined CDF and D0 Upper Limits on Standard Model Higgs- Boson Production with up to 6.7 fb^{-1} of Data”, 2010, arxiv :1007.4587.
- [3] CMS Collaboration, “First Measurement of the Cross Section for Top-Quark Pair Production in Proton-Proton Collisions at $\sqrt{s}=7 \text{ TeV}$ ”, 2010, arxiv :1010.5994.
- [4] Atlas Collaboration, “Top quark pair production Cross Section in ATLAS with early data”, 2010, arxiv :1010.0148.
- [5] CMS Collaboration, “Search for dijet resonances in the dijet mass distribution in pp collisions at $\sqrt{s}=7 \text{ tev}$ ”, 2010.
- [6] Atlas Collaboration, “Search for quark contact interactions in dijet angular distributions in pp collisions at $\sqrt{s} = 7 \text{ tev}$ measured with the atlas detector.”, tech. rep., CERN, Geneva, 2010, arXiv :1009.5069, oai :cds.cern.ch :1294880.
- [7] CMS Collaboration, “Search for pair production of first generation scalar leptoquarks using events containing two electrons and two jets produced in pp collisions at $\sqrt{s} = 7 \text{ tev}$ ”, 2010.
- [8] LEP Electroweak Working Group. <http://lepewwg.web.cern.ch/>.
- [9] R. Barate *et al.*, “Search for the standard model Higgs boson at LEP”, *Phys. Lett.*, vol. B565, pp. 61–75, 2003, hep-ex/0306033.
- [10] N. Arkani-Hamed, S. Dimopoulos, and G. R. Dvali, “The hierarchy problem and new dimensions at a millimeter”, *Phys. Lett.*, vol. B429, pp. 263–272, 1998, hep-ph/9803315.

- [11] L. Randall and R. Sundrum, “A large mass hierarchy from a small extra dimension”, *Phys. Rev. Lett.*, vol. 83, pp. 3370–3373, 1999, hep-ph/9905221.
- [12] P. C. West, “Introduction to supersymmetry and supergravity”, p. 425, 1990. Singapore, World Scientific.
- [13] S. P. Martin, “A Supersymmetry Primer”, 1997, hep-ph/9709356.
- [14] C. T. Hill and E. H. Simmons, “Strong dynamics and electroweak symmetry breaking”, *Phys. Rept.*, vol. 381, pp. 235–402, 2003, hep-ph/0203079.
- [15] E. Farhi and L. Susskind, “Technicolor”, *Phys. Rept.*, vol. 74, p. 277, 1981.
- [16] J. DiBello, R. Konoplich, N. Lavini, and T. S. Laurent, “Endpoints of invariant mass distribution in SUSY particle decays into massive particles”, 2010, arxiv :1004.4819.
- [17] C. G. Lester and D. J. Summers, “Measuring masses of semiinvisibly decaying particles pair produced at hadron colliders”, *Phys. Lett.*, vol. B463, pp. 99–103, 1999, hep-ph/9906349.
- [18] A. Barr, C. Lester, and P. Stephens, “ $m(T_2)$: The Truth behind the glamour”, *J. Phys.*, vol. G29, pp. 2343–2363, 2003, hep-ph/0304226.
- [19] A. J. Barr and C. G. Lester, “A Review of the Mass Measurement Techniques proposed for the Large Hadron Collider”, 2010, arxiv :1004.2732.
- [20] J. Heyninck, “Kinematic fit in CMS & the use of top quarks for calibration”, *PoS*, vol. TOP2006, p. 024, 2006.
- [21] P. Artoisenet, V. Lemaitre, F. Maltoni, and O. Mattelaer, “Automation of the matrix element reweighting method”, 2010, arxiv :1007.3300.
- [22] J. Alwall *et al.*, “New Developments in MadGraph/MadEvent”, *AIP Conf. Proc.*, vol. 1078, pp. 84–89, 2009, arxiv :0809.2410.
- [23] P. Artoisenet and O. Mattelaer, “MadWeight : Automatic event reweighting with matrix elements”, *PoS*, vol. CHARGED2008, p. 025, 2008.
- [24] J. Alwall, A. Freitas, and O. Mattelaer, “The Matrix Element Method and QCD Radiation”, 2010, arxiv :1010.2263.
- [25] J. Alwall, A. Freitas, and O. Mattelaer, “Measuring Sparticles with the Matrix Element”, *AIP Conf. Proc.*, vol. 1200, pp. 442–445, 2010, arxiv :0910.2522.
- [26] J. F. Gunion, H. E. Haber, G. L. Kane, and S. Dawson, “the higgs hunter’s guide”, 1989, SCIPP-89/13.
- [27] A. Djouadi, “The Anatomy of electro-weak symmetry breaking. I : The Higgs boson in the standard model”, *Phys. Rept.*, vol. 457, pp. 1–216, 2008, hep-ph/0503172.
- [28] A. Salam, “Weak and Electromagnetic Interactions”, 1968. Originally printed in *Svartholm : Elementary Particle Theory, Proceedings Of The Nobel Symposium Held 1968 At Lerum, Sweden*, Stockholm 1968, 367-377.

- [29] S. L. Glashow, “Partial Symmetries of Weak Interactions”, *Nucl. Phys.*, vol. 22, pp. 579–588, 1961.
- [30] S. Weinberg, “A Model of Leptons”, *Phys. Rev. Lett.*, vol. 19, pp. 1264–1266, 1967.
- [31] P. W. Higgs, “Broken symmetries, massless particles and gauge fields”, *Phys. Lett.*, vol. 12, pp. 132–133, 1964.
- [32] F. Englert and R. Brout, “Broken symmetry and the mass of gauge vector mesons”, *Phys. Rev. Lett.*, vol. 13, pp. 321–322, 1964.
- [33] R. Brout and F. Englert, “Spontaneous broken symmetry”, *Comptes Rendus Physique*, vol. 8, pp. 973–985, 2007.
- [34] C. H. Llewellyn Smith, “High-Energy Behavior and Gauge Symmetry”, *Phys. Lett.*, vol. B46, pp. 233–236, 1973.
- [35] W. S. R.K. Ellis and B.R. Webber, “Qcd and collider physics”, Cambridge Monographs on Particle Physics, Nuclear Physics and Cosmology, Volume 8 (Cambridge University Press, 1996).
- [36] M. H. Seymour, “Quantum ChromoDynamics”, 2010, arxiv :1010.2330.
- [37] F. J. Yndurain, “Limits on the mass of the gluon”, *Phys. Lett.*, vol. B345, pp. 524–526, 1995.
- [38] S. Willenbrock, “Radiative corrections to heavy Higgs physics”, *Proceedings, 4th Meeting of the Division of Particles and Fields of the APS*, pp. 715–718, 1988.
- [39] K. Riesselmann and S. Willenbrock, “Ruling out a strongly-interacting standard Higgs model”, *Phys. Rev.*, vol. D55, pp. 311–321, 1997, hep-ph/9608280.
- [40] E. Accomando *et al.*, “Physics with e^+e^- linear colliders”, *Phys. Rept.*, vol. 299, pp. 1–78, 1998, hep-ph/9705442.
- [41] U. Aglietti *et al.*, “Tevatron for LHC report : Higgs”, 2006, hep-ph/0612172.
- [42] T. Aaltonen, “Combined $W H \rightarrow l \nu b \bar{b}$ search at CDF with neural network and matrix element techniques”, *PoS*, vol. HCP2009, p. 061, 2009.
- [43] V. Barger, J. L. Hewett, and T. G. Rizzo, “Top-quark mass predictions from w, z masses and z partial widths”, *Phys. Rev. Lett.*, vol. 65, no. 11, pp. 1313–1316, 1990.
- [44] M. J. G. Veltman, “Limit on Mass Differences in the Weinberg Model”, *Nucl. Phys.*, vol. B123, p. 89, 1977.
- [45] P. Sikivie, L. Susskind, M. B. Voloshin, and V. I. Zakharov, “Isospin Breaking in Technicolor Models”, *Nucl. Phys.*, vol. B173, p. 189, 1980.
- [46] R. Lytel, “Weak isospin breaking and higher order corrections”, *Phys. Rev.*, vol. D22, p. 505, 1980.

- [47] M. Lemoine and M. J. G. Veltman, “Radiative Corrections to $e^+ e^- \rightarrow W^+ W^-$ in the Weinberg Model”, *Nucl. Phys.*, vol. B164, p. 445, 1980.
- [48] M. B. Einhorn, D. R. T. Jones, and M. J. G. Veltman, “Heavy Particles and the rho Parameter in the Standard Model”, *Nucl. Phys.*, vol. B191, p. 146, 1981.
- [49] S. Willenbrock, “Symmetries of the standard model”, 2004, hep-ph/0410370.
- [50] G. D’Agostini and G. Degrassi, “Constraining the Higgs boson mass through the combination of direct search and precision measurement results”, 2000, hep-ph/0001269.
- [51] G. F. Giudice, “Theories for the Fermi Scale”, *J. Phys. Conf. Ser.*, vol. 110, p. 012014, 2008, arxiv :0710.3294.
- [52] K. Abe *et al.*, “A high-precision measurement of the left-right Z boson cross-section asymmetry”, *Phys. Rev. Lett.*, vol. 84, pp. 5945–5949, 2000, hep-ex/0004026.
- [53] K. Abe *et al.*, “First direct measurement of the parity-violating coupling of the Z0 to the s-quark”, *Phys. Rev. Lett.*, vol. 85, pp. 5059–5063, 2000, hep-ex/0006019.
- [54] K. Kondo, “Dynamical likelihood method for reconstruction of events with missing momentum. 1 : method and toy models”, *J. Phys. Soc. Jap.*, vol. 57, pp. 4126–4140, 1988.
- [55] K. Kondo, “Dynamical likelihood method for reconstruction of events with missing momentum. 2 : Mass spectra for $2 \rightarrow 2$ processes”, *J. Phys. Soc. Jap.*, vol. 60, pp. 836–844, 1991.
- [56] K. Kondo, T. Chikamatsu, and S. H. Kim, “Dynamical likelihood method for reconstruction of events with missing momentum. 3 : Analysis of a CDF high $p(T) e \mu$ event as $t \text{ anti-}t$ production”, *J. Phys. Soc. Jap.*, vol. 62, pp. 1177–1182, 1993.
- [57] R. H. Dalitz and G. R. Goldstein, “The Decay and polarization properties of the top quark”, *Phys. Rev.*, vol. D45, pp. 1531–1543, 1992.
- [58] R. H. Dalitz and G. R. Goldstein, “Analysis of top-antitop production and dilepton decay events and the top quark mass”, *Phys. Lett.*, vol. B287, pp. 225–230, 1992.
- [59] G. R. Goldstein, K. Sliwa, and R. H. Dalitz, “On observing top quark production at the tevatron”, *Phys. Rev.*, vol. D47, pp. 967–972, 1993, hep-ph/9205246.
- [60] R. H. Dalitz and G. R. Goldstein, “Where is top?”, *Int. J. Mod. Phys.*, vol. A9, pp. 635–666, 1994, hep-ph/9308345.
- [61] C. F. Kolda and H. Murayama, “The Higgs mass and new physics scales in the minimal standard model”, *JHEP*, vol. 07, p. 035, 2000, hep-ph/0003170.

- [62] M. Schmaltz and D. Tucker-Smith, “Little Higgs Review”, *Ann. Rev. Nucl. Part. Sci.*, vol. 55, pp. 229–270, 2005, hep-ph/0502182.
- [63] E. Komatsu *et al.*, “Seven-Year Wilkinson Microwave Anisotropy Probe (WMAP) Observations : Cosmological Interpretation”, 2010, arxiv :1001.4538.
- [64] L. Girardello and M. T. Grisaru, “Soft breaking of supersymmetry”, *Nuclear Physics B*, vol. 194, pp. 65–76, 1982.
- [65] P. Fayet, “Supergauge Invariant Extension of the Higgs Mechanism and a Model for the electron and Its Neutrino”, *Nucl. Phys.*, vol. B90, pp. 104–124, 1975.
- [66] S. Profumo and C. E. Yaguna, “A statistical analysis of supersymmetric dark matter in the MSSM after WMAP”, *Phys. Rev.*, vol. D70, p. 095004, 2004, hep-ph/0407036.
- [67] H.-C. Cheng, D. Engelhardt, J. F. Gunion, Z. Han, and B. McElrath, “Accurate Mass Determinations in Decay Chains with Missing Energy”, *Phys. Rev. Lett.*, vol. 100, p. 252001, 2008, arxiv :0802.4290.
- [68] H.-C. Cheng, J. F. Gunion, Z. Han, and B. McElrath, “Accurate Mass Determinations in Decay Chains with Missing Energy : II”, *Phys. Rev.*, vol. D80, p. 035020, 2009, arxiv :0905.1344.
- [69] V. M. Abazov *et al.*, “A precision measurement of the mass of the top quark”, *Nature*, vol. 429, pp. 638–642, 2004, hep-ex/0406031.
- [70] V. M. Abazov *et al.*, “Measurement of the top quark mass in the lepton + jets final state with the matrix element method”, *Phys. Rev.*, vol. D74, p. 092005, 2006, hep-ex/0609053.
- [71] A. Abulencia *et al.*, “Precise measurement of the top quark mass in the lepton+jets topology at CDF II”, *Phys. Rev. Lett.*, vol. 99, p. 182002, 2007, hep-ex/0703045.
- [72] A. Abulencia *et al.*, “Precision measurement of the top quark mass from dilepton events at CDF II”, *Phys. Rev.*, vol. D75, p. 031105, 2007, hep-ex/0612060.
- [73] V. M. Abazov *et al.*, “Measurement of the top quark mass in the dilepton channel”, *Phys. Lett.*, vol. B655, p. 7, 2007, hep-ex/0609056.
- [74] T. Aaltonen *et al.*, “First Observation of Electroweak Single Top Quark Production”, *Phys. Rev. Lett.*, vol. 103, p. 092002, 2009, arxiv :0903.0885.
- [75] V. M. Abazov *et al.*, “Observation of Single Top-Quark Production”, *Phys. Rev. Lett.*, vol. 103, p. 092001, 2009, arxiv :0903.0850.
- [76] Joint CDF and DO collaboration, “Combined CDF and D0 Upper Limits on Standard Model Higgs-Boson Production with up to 4.2 fb⁻¹ of Data”, 2009, arxiv :0903.4001.
- [77] F. Maltoni and T. Stelzer, “MadEvent : Automatic event generation with MadGraph”, *JHEP*, vol. 02, p. 027, 2003, hep-ph/0208156.

- [78] A. Pukhov, “Calcchep 2.3 : MSSM, structure functions, event generation, 1, and generation of matrix elements for other packages”, 2004, hep-ph/0412191.
- [79] T. Gleisberg *et al.*, “SHERPA 1.alpha, a proof-of-concept version”, *JHEP*, vol. 02, p. 056, 2004, hep-ph/0311263.
- [80] S. Weinzierl, “Introduction to Monte Carlo methods”, 2000, hep-ph/0006269.
- [81] J. Alwall *et al.*, “MadGraph/MadEvent v4 : The New Web Generation”, *JHEP*, vol. 09, p. 028, 2007, arxiv :0706.2334.
- [82] C. G. Papadopoulos, “PHEGAS : A phase space generator for automatic cross-section computation”, *Comput. Phys. Commun.*, vol. 137, pp. 247–254, 2001, hep-ph/0007335.
- [83] G. P. Lepage, “VEGAS : an adaptive multidimensional integration Program”, 1980. CLNS-80/447.
- [84] W. H. Press and G. R. Farrar, “recursive stratified sampling for multidimensional monte carlo integration”, 1989. CFA-3010.
- [85] V. M. Abazov *et al.*, “Helicity of the W boson in lepton + jets $t\bar{t}$ events”, *Phys. Lett.*, vol. B617, pp. 1–10, 2005, hep-ex/0404040.
- [86] J. Pumplin *et al.*, “New generation of parton distributions with uncertainties from global QCD analysis”, *JHEP*, vol. 07, p. 012, 2002, hep-ph/0201195.
- [87] J. Conway, “Pretty Good Simulator”,
<http://www.physics.ucdavis.edu/~conway/research/software/pgs/pgs.html>.
- [88] M. F. Canelli, “Helicity of the W boson in single - lepton $t\bar{t}$ events”, 2003. UMI-31-14921.
- [89] K. Cranmer and T. Plehn, “Maximum significance at the LHC and Higgs decays to muons”, *Eur. Phys. J.*, vol. C51, pp. 415–420, 2007, hep-ph/0605268.
- [90] V. M. Abazov *et al.*, “Precise measurement of the top quark mass from lepton+jets events at D0”, *Phys. Rev. Lett.*, vol. 101, p. 182001, 2008, arxiv :0807.2141.
- [91] V. M. Abazov *et al.*, “Search for charged Higgs bosons in top quark decays”, *Phys. Lett.*, vol. B682, pp. 278–286, 2009, arxiv :0908.1811.
- [92] V. M. Abazov *et al.*, “Search for charged Higgs bosons in decays of top quarks”, *Phys. Rev.*, vol. D80, p. 051107, 2009, arxiv :0906.5326.
- [93] A. Abulencia *et al.*, “Search for charged Higgs bosons from top quark decays in $p\bar{p}$ collisions at $\sqrt{s} = 1.96$ -TeV”, *Phys. Rev. Lett.*, vol. 96, p. 042003, 2006, hep-ex/0510065.
- [94] T. Aaltonen *et al.*, “Search for charged Higgs bosons in decays of top quarks in $p - \bar{p}$ collisions at $\sqrt{s} = 1.96$ TeV”, *Phys. Rev. Lett.*, vol. 103, p. 101803, 2009, arxiv :0907.1269.

- [95] D. Wicke, “Properties of the Top Quark”, 2009, arxiv :1005.2460.
- [96] T. Aaltonen *et al.*, “First Measurement of the $t\bar{t}$ Differential Cross Section $d\sigma/dM_{t\bar{t}}$ in $p\bar{p}$ Collisions at $\sqrt{s} = 1.96$ TeV”, *Phys. Rev. Lett.*, vol. 102, p. 222003, 2009, arxiv :0903.2850.
- [97] CDF Collaboration, “Search for resonant $t\bar{t}$ production in $p\bar{p}$ collisions at $\sqrt{s} = 1.96$ tev”, 2009.
- [98] R. Frederix and F. Maltoni, “Top pair invariant mass distribution : a window on new physics”, *JHEP*, vol. 01, p. 047, 2009, arxiv :0712.2355.
- [99] J. Alwall, S. de Visscher, and F. Maltoni, “QCD radiation in the production of heavy colored particles at the LHC”, *JHEP*, vol. 02, p. 017, 2009, arxiv :0810.5350.
- [100] T. Plehn, D. Rainwater, and P. Z. Skands, “Squark and gluino production with jets”, *Phys. Lett.*, vol. B645, pp. 217–221, 2007, hep-ph/0510144.
- [101] T. Sjostrand, S. Mrenna, and P. Skands, “PYTHIA 6.4 physics and manual”, *JHEP*, vol. 05, p. 026, 2006, hep-ph/0603175.
- [102] E. Boos *et al.*, “CompHEP 4.4 : Automatic computations from Lagrangians to events”, *Nucl. Instrum. Meth.*, vol. A534, pp. 250–259, 2004, hep-ph/0403113.
- [103] V. V. Sudakov, “Vertex parts at very high-energies in quantum electrodynamics”, *Sov. Phys. JETP*, vol. 3, pp. 65–71, 1956.
- [104] J. C. Collins, “Sudakov form factors”, *Adv. Ser. Direct. High Energy Phys.*, vol. 5, pp. 573–614, 1989, hep-ph/0312336.
- [105] J. Alwall, M. Herquet, F. Maltoni, O. Mattelaer and T. Stelzer, “Madgraph 5”, 2011. In preparation.
- [106] K. Nakamura *et al.* (Particle Data Group), “Particle Data Group.” *J. Phys. G* 37, 075021 (2010).